The application of GHz bandwidth electrical pulses to a single semiconductor quantum dot.

Jamie McFarlane

Submitted for the degree of Doctor of Philosophy

Heriot-Watt University

School of Engineering and Physical Sciences

May 2009

Abstract

Quantum dots contain several isolated two-level quantum systems, an ideal starting point for the creation of a qubit. A single quantum dot embedded within a charge-tunable heterostructure can be optically isolated using confocal microscopy, and electrically manipulated using an applied voltage. This thesis presents progress towards full opto-electrical control over a single dot, with a specific interest in the creation of a fully controllable electrically triggered deterministic single photon source.

Polarisation control was incorporated into the confocal microscope setup, and polarisation filtering was used to enhance the signal to noise ratio in photoluminescence studies. Weierstrass solid immersion lens technology was included in the microscope design in order to improve the collection efficiency of dot photoluminescence.

Static voltages were applied over single dots. Time-resolved spectroscopy allows the identification of hole tunnelling from the dot to the capping layer-superlattice interface. Suppression of hole tunnelling is achieved by altering the wafer structure. Autocorrelation measurements exhibit a finite second-order correlation at zero time delay, which is attributed to hole recapture from the wetting layer. Resonant excitation of the neutral exciton results in the creation of a negative trion in a specific voltage regime.

Photolithography and electron-beam evaporation were used to manufacture several micron-scale opto-electronic devices. Several changes were made with the intention of reducing the resistance and capacitance of the device, with respect to the original macroscopic design. Photoluminescence measurements show that single dots in the new devices are capable of responding to GHz bandwidth voltage pulses.

Finally, GHz bandwidth voltage pulses were applied to several single quantum dots. Single and multiple electron charging was observed on the timescale of exciton recombination. Several memory bit variations were demonstrated, each with an electrically triggered read-out mechanism. Two electrically triggered deterministic single photon sources were demonstrated, one using CW non-resonant optical excitation, the other using pulsed resonant optical excitation. Lastly, rapid adiabatic passage was attempted, with mixed results.

Acknowledgements

The following people were crucial to the success of this work:

Richard Warburton
Paul Dalgarno
Daniel Brunner
Stefan Seidl
Mark Leonard
Neil Ross
Brian Gerardot
Robert Hadfield
Kevin Prior
Mum and Dad

ACADEMIC REGISTRY

Research Thesis Submission

Name:	Jamie McFarlane		
School/PGI:	School of Engineering and Physical Sciences		
Version: *(i.e. First, Resubmission, Final)*		Degree Sought (Award **and** Subject area)	PhD in Physics

Declaration

In accordance with the appropriate regulations I hereby submit my thesis and I declare that:

1) the thesis embodies the results of my own work and has been composed by myself
2) where appropriate, I have made acknowledgement of the work of others and have made reference to work carried out in collaboration with other persons
3) the thesis is the correct version of the thesis for submission and is the same version as any electronic versions submitted*.
4) my thesis for the award referred to, deposited in the Heriot-Watt University Library, should be made available for loan or photocopying and be available via the Institutional Repository, subject to such conditions as the Librarian may require
5) I understand that as a student of the University I am required to abide by the Regulations of the University and to conform to its discipline.

* *Please note that it is the responsibility of the candidate to ensure that the correct version of the thesis is submitted.*

Signature of Candidate:		Date:	

Submission

Submitted By *(name in capitals):*	
Signature of Individual Submitting:	
Date Submitted:	

For Completion in Academic Registry

Received in the Academic Registry by *(name in capitals):*			
Method of Submission *(Handed in to Academic Registry; posted through internal/external mail):*			
E-thesis Submitted (***mandatory for final theses from January 2009)***			
Signature:		Date:	

Contents

Author publications

J. McFarlane, P. A. Dalgarno, B. D. Gerardot, R. H. Hadfield, R. J. Warburton, K. Karrai, A. Badolato and P. M. Petroff, *Gigahertz bandwidth electrical control over a dark exciton-based memory bit in a single quantum dot.* Applied Physics Letters, **94**, 093113 (2009). Also included in the Virtual Journal of Nanoscale Science & Technology, **94**, 12 (2009).

P. A. Dalgarno, **J. McFarlane**, D. Brunner, R. W. Lambert, B. D. Gerardot, R. J. Warburton, K. Karrai, A. Badolato and P. M. Petroff, *Hole recapture limited single photon generation from a single n-type charge-tunable quantum dot.* Applied Physics Letters, **92**, 193103 (2008).

P. A. Dalgarno, J. M. Smith, **J. McFarlane**, B. D. Gerardot, K. Karrai, A. Badolato, P. M. Petroff and R. J. Warburton, *Coulomb interactions in single charged self-assembled quantum dots: Radiative lifetime and recombination energy.* Physical Review B, **77**, 245311 (2008).

P. A. Dalgarno, **J. McFarlane**, B. D. Gerardot, R. J. Warburton, K. Karrai, A. Badolato and P. M. Petroff, *Decay dynamics of the positively charged exciton in a single charge tunable self-assembled quantum dot.* Applied Physics Letters, **89**, 043107 (2006).

Author conferences

J. McFarlane, P. A. Dalgarno, B. D. Gerardot, K. Karrai, A. Badolato, P. M. Petroff and R. J. Warburton, *Single photons on demand using GHz voltage pulses over a quantum dot.* Oral presentation, Photon08, Edinburgh, August 2008.

J. McFarlane, P. A. Dalgarno, B. D. Gerardot, M. Leonard, K. Karrai, A. Badolato, P. M. Petroff and R. J. Warburton, *GHz electrical manipulation of single dark excitons.* Oral presentation, QD2008: International conference on semiconductor quantum dots, Gyeongju, Korea, May 2008.

J. McFarlane, P. A. Dalgarno, B. D. Gerardot, K. Karrai, A. Badolato, P. M. Petroff and R. J. Warburton, *GHz electrically triggered exciton spin flip in a single quantum dot.* Poster presentation, One day quantum dot meeting, London, January 2008.

J. McFarlane, P. A. Dalgarno, B. D. Gerardot, K. Karrai, P. M. Petroff, M. Leonard and R. J. Warburton, *Manipulating the emission from a single charge-tunable quantum dot with sub-nanosecond voltage pulses.* Oral presentation, CSUK: UK compound semiconductors annual conference, Sheffield, July 2007.

J. McFarlane, P. A. Dalgarno, B. D. Gerardot, K. Karrai, P. M. Petroff and R. J. Warburton, *Control of Hole Tunnelling in Charge Tunable Quantum Dots.* Oral presentation, Photon06, Manchester, September 2006.

Chapter 1

A Quantum dot-based Qubit

Quantum dots are semiconductor nanostructures which exhibit atom-like discrete energy levels. Several two-level quantum systems can be created within a single dot, and due to this it has promising applications as a structure for manipulating, storing and communicating single qubits. Absolute control over a qubit is essential for applications such as quantum cryptography and quantum computing. In order to exploit a single quantum dot as a functional device, full optical and electrical control is needed.

1.1 Motivation–the creation of a qubit

A quantum bit (or qubit) is the basic element of many of the more popular applications goals of quantum physics, namely quantum cryptography and quantum computing. The qubit is analogous to the regular bit in standard computation in that it can take values of 1 or 0, but intrinsically different in that it can also be created in a superposition of both states.

$$|\psi\rangle = \alpha|0\rangle + \beta|1\rangle \tag{1.1}$$

where $|\psi\rangle$ is the wavefunction of the qubit, defined as a superposition of $|0\rangle$ and $|1\rangle$ states, with α and β as probability amplitudes. The requirement is therefore any two level quantum mechanical system, for instance: atomic spin, atomic charge, excitation between atomic energy levels, photon polarisation, or photon phase. However, there is a need for absolute control over processing and communication. In order to be fully functionalised, a qubit needs to be stored and/or manipulated without suffering adversely due to decoherence effects, and also potentially transmitted between processing sites. What follows is a simple discussion of the requirements of the main qubit systems under development.

1.1.1 Quantum Cryptography

There are several people credited with the idea behind quantum cryptography, including Stephen Wiesner, Charles Bennett, Gilles Brassard and Artur Ekert [1]. The idea is simple, based around the communication of a cryptographic key between two parties (commonly named Alice and Bob) which is potentially being intercepted by an eavesdropper (named Eve). There are two communication paths: a public channel and a quantum channel. The quantum channel is based on the communication of qubits with one of two orthogonal basis types. Alice sends Bob a key of random bits, each in a random basis. Bob detects the key using a random basis. Alice and bob then compare basis orientations through a public channel. The bits in which the basis matched forms the key. Alice and Bob can now communicate across the public channel using the key to encode/decode the information. The key is never transferred across the public channel, only the series of bases. If Eve listens in to the conversation, she cannot recreate both the basis and the bit sent by Alice, and hence introduces an error into the communication. If Alice and Bob compare part of their bit stream, they will find this error.

In test systems, weak laser sources are often used to provide the single photons [2, 3]. These systems use largely attenuated laser pulses (with the number of photons governed by Poisson statistics) with a very low mean photon number, μ. These sources are however inefficient and insecure. Most of the pulses are empty, and there is a probability $P \sim \frac{\mu^2}{2}$ that the pulses will contain two or more photons, which leaves the channel open to photon number splitting attacks [1]. A true single photon source would solve this problem.

1.1.2 Entanglement

Further to single photon physics, entanglement of two or more photons is also desirable. Entanglement can be defined as the quantum uncertainty between two or more particles, in which the wavefunction of each particle can only be described with reference to the others. In a flying qubit this can take the form of either polarisation entanglement, or energy-time entanglement [1]. Again this can be used for cryptography [12], but also for quantum computing and quantum teleportation [13]. There are several methods for creating entangled photons, including: parametric down-conversion in a non-linear crystal (which doesn't allow the triggered production of entangled photons), and exciton cascade processes within quantum dots [14, 15].

1.1.3 Quantum Computing

Quantum computing promises a large step forward in information processing. Unlike many conventional calculations, those done using wavefunctions instead of bit streams allow either an increase in the speed of the calculation, or a decrease in the quantity of input data required [4].

The basic premise of quantum computing necessitates the qubit. This needs to be easily manipulated within its environment, stored, and entangled with other qubits as well as being measurable. However, potential limits caused by decoherence and noise have already been addressed and quantified [5]. The main restrictive factor in the current technologies of trapped ions [6, 7], quantum dots [8], nuclear magnetic resonance [9], and optical lattices of neutral atoms [10] is the issue of scalability. Although proof of principle experiments have been shown [11], there continues to be a need for a valid way of increasing the processing capability of such a system.

1.1.4 An ideal quantum optics device

There is currently a need for a technology which can accommodate the previously mentioned applications. Such a device should have the ability to emit single (anti-bunched) photons with sub-Poissonian probability. The device should be optically efficient in order to successfully transmit a flying qubit (generally a photon). The device should also be scalable in order that it can be more easily integrated and manufactured. When stored, the qubit should be largely unaffected by decoherence and other effects (such as random spin precession) which can affect the data. Lastly, the device should ideally be fully controllable, with a defined write-store-manipulate-read process which can be triggered externally. A solid state device is therefore preferable, because it provides easy optical and electrical access, and the technology is already in place to grow and process devices on a large scale.

1.2 Quantum dots

1.2.1 Confinement in three dimensions

When the width of a confining potential becomes similar to the de Broglie wavelength of a trapped particle ($\lambda_{DB} = \frac{h}{p}$, where p is the particle momentum) there is a quantisation of the available energy levels. In bulk semiconductor material, the broad conduction and valence energy continuum of the material can become thin energy bands through the use of a heterostructure, in which materials with differing bandgap energies are grown one after another to produce a quantum well.

A quantum well represents confinement in one dimension; any carriers trapped in the well are free to move within the 2-dimensional growth plane of the sample. Reducing the dimensionality further, there is confinement in two dimensions with quantum wires, and confinement in all three directions with quantum dots. Quantum dots are often referred to as “artificial atoms” because the strong carrier confinement causes the density of states to form sharp ($\sim$ μeV at liquid helium temperatures) Lorentzian peaks occurring at discrete energies, like those of a single atom.

1.2.2 Trapped carriers

It was originally thought that quantum dots would experience a phonon bottleneck, in which intra-dot carrier relaxation would be much slower than the radiative recombination rate [16]. This was theorised because the energy level separations were larger than the energy of the available acoustic phonons. However, due perhaps to electron-hole scattering [17, 18], multiphonon processes [19, 20] or Auger processes [21, 22] in which electrons can relax by promoting another nearby electron to a higher energy level, carriers that are excited non-resonantly at a higher energy than the bulk material bandgap energy were found to quickly relax into the lowest energy levels in the dot [23]. This offers a level of control over the excitons which form in the dot, as the lowest energy level available to a carrier will be preferentially filled.

The dots studied in this work are InGaAs, embedded within a GaAs heterostructure. The dot potential is approximately parabolic for low energies [2], but there is evidence that there is a softening of the potential at higher energies [24]. Standard atomic energy level nomenclature is used when describing the dot energy levels, s being the lowest energy level, and p being the next lowest. The dots are lens shaped, and because of this, the parabolic potential is steep in the growth direction and shallower in the lateral plane. Due to this, although like atomic physics the s-shell in the dot can be occupied by up to two electrons/holes (with angular momentum quantum number $l = 0$), the p-shell can only be occupied by four electrons/holes ($l = 1$), as the p-shell energy in the growth direction lies at a higher energy than can be contained within the dot.

The Pauli exclusion principle specifies that if there are two electrons/holes in the s-shell orbital of the dot they must have opposite spin. Electrons in the dot have either spin up or spin down, with angular momentum $S_z = \pm\frac{1}{2}$. The holes which are of relevance to this work are heavy holes, which again must have spin up or spin down, but with angular momentum $J_z = \pm\frac{3}{2}$. Photons, with left or right handed circular polarisation have spin angular momentum $L = 1$, and so due to conservation of angular momentum electron-hole recombination can only occur if the electron and hole have opposite spin. Excitons in which the electrons and holes have the same spin ($L = 2$) are referred to as dark states due to their inability to recombine radiatively.

1.2.3 Controllable interaction

A quantum dot is an ideal place to start with respect to fabricating a device based on controllable interaction and storage of a qubit. The formation of an exciton provides a great example of two-level quantum system, with the knowledge that any carriers available to the dot will relax into the lowest available energy levels. In addition, there are clear selection rules which determine whether electron-hole pairs can recombine. At 5 K, the thermal energy (k_BT) is around 0.4 meV, which is much smaller than the electron/hole ionisation energy in the dot (typically 70-130 meV). Therefore once a carrier is in the dot, it is stable until perturbed externally. In this way, single carriers or dark states have potential for use as memory elements within a single dot

Carrier spin is another two level quantum system which is accessible through the use of quantum dots. Carriers which are excited non-resonantly into the bulk semiconductor lose their spin when relaxing through the dot energy levels, but resonant excitation can be used to inject an electron-hole pair with known spin into the dot. If an exciton is resonantly excited into the dot with a known carrier spin, it can be expected to maintain that spin until either: spin relaxation occurs in time T_1, or decoherence of the spin phase occurs in time T_2.

1.3 Dot Growth

In order to provide access to the benefits intrinsic to the semiconductor quantum dots studied here the dots were grown within a heterostructure that allows optical and electrical manipulation.

1.3.1 Stranski–Krastanov growth

The dots used in this work were self-assembled InGaAs dots grown on a GaAs substrate by molecular beam epitaxy (MBE) using a Stranski–Krastanov growth method.

The 7% lattice mismatch between InAs and GaAs causes the formation of the InAs islands over a ∼1 monolayer InAs wetting layer. As the InAs is deposited, the islands (quantum dots) form at ∼1.5 monolayers as an attempt to alleviate the strain [25]. If more than ∼2 monolayers of InAs are deposited dislocations start to occur which reduce the optical efficiency of the sample [25].

Creation of InGaAs quantum dots is achieved by in-situ annealing. The dots used in this work are covered with 1 nm of GaAs and annealed at 530 °C for 30 seconds. The anneal causes considerable diffusion of Ga into the InAs dots, causing the optical and electrical properties to be affected [26]. During the overgrowth the photoluminescence (PL) energy of the dots changes from ∼1.05 eV to ∼1.3 eV. This gives an advantage in that the silicon detectors used to detect PL from the quantum dot (using a spectrometer or a single photon avalanche photo-diode) have an extremely low efficiency at 1.1 eV, increasing to ∼20% at 1.3 eV. This however moves the PL further from the 1.3 μm wavelength which would be desirable for long distance quantum key distribution using optical fibres.

The wetting layer functions as a quantum well, and forms a continuum of states above the quantum dot energy levels, but below that of the bulk GaAs. Non-resonant optical excitation at 830 nm is often used in this work, to excite carriers specifically into the wetting layer states.

Due to the self-assembly process, there is a large inhomogeneity of dot size of around 10% [25]. This causes an equivalent range in emission energies between individual dots, which is currently one of the main problems of this method with reference to the scalability, although this may be overcome using dot selection methods (mesas, confocal microscopy etc.).

1.3.2 Preparation for single dot spectroscopy

The typical dot density created using the self-assembly method is 10^{10} dots per cm^2. This is rather restrictive for single dot selection, even whilst using a selection method such as confocal microscopy. In MBE growth the substrate is normally rotated to prevent uneven material growth, but during the growth of the wafers used in this work the substrate rotation was halted during the dot growth. In this way a dot density gradient is created over the wafer surface, allowing the density to be chosen so that dot selection is more easily achievable.

1.3.3 Quantum dot imaging

Atomic force microscopy (AFM) on uncovered quantum dots gives an indication of their size and distribution. Fig. 1.1 shows an AFM scan of uncovered InAs dots grown on GaAs. The dots are typically lens shaped, ∼5 nm in the growth direction and ∼20 nm in the growth plane. There is a random distribution of dots over the sample surface.

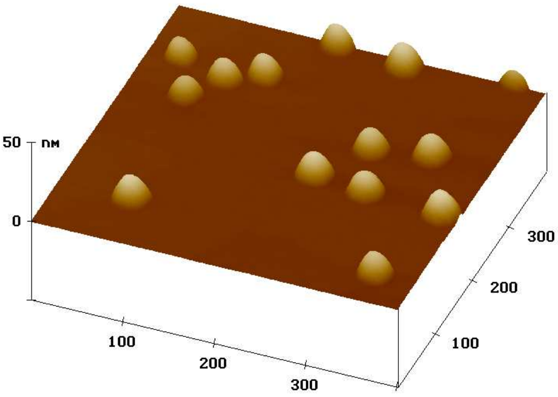

Figure 1.1: AFM scan of uncapped InAs quantum quantum dots on a GaAs substrate; All dimensions are in nanometers. Image by Axel Lorke.

The annealing process changes the dot composition and shape [27]. Cross-sectional scanning tunneling microscopy (X-STM) can be used to assess the shape of the capped dots. X-STM involves cleaving the wafer and performing scanning tunneling microscopy on the cleaved edge, in ultra-high vacuum. As seen in Fig.1.2 the capped dots have an truncated lens shape.

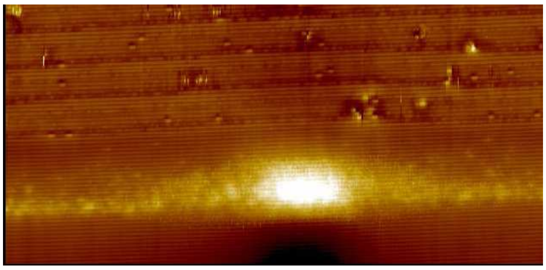

Figure 1.2: X-STM scan of capped InAs quantum quantum dots on a GaAs substrate. Image supplied by Murat Bozkurt and Paul Koenraad.

1.4 Optical excitation

1.4.1 Photoluminescence

Quantum dots embedded within a semiconductor heterostructure are not limited by photoblinking or photobleaching, as is the case with colloidal quantum dots [28]. This makes embedded dots more suitable than colloidal dots for photoluminescence (PL) spectroscopy. Illuminating the structure with non-resonant 830 nm laser light causes electrons in the wetting layer to be excited from the valence band energy continuum to the conduction band energy continuum. The carriers then relax quickly to the lowest energy levels available in the dot. Alternatively, exciting resonantly excites electrons from the dot valence band energy levels to the conduction band energy levels. If recombination is possible (and without the use of any cavity technology), electron-hole recombination will release a photon in any direction. The spin of an electron-hole pair will determine whether the photon released has left- or right-handed circular polarisation.

If weak non-resonant excitation is used, PL is observed from single excitons in the dot that have relaxed to the s-shell before recombining. As the excitation power is increased carriers will relax into the dot at a faster rate than the recombination rate, and higher energy exciton PL (eg. from two hole or three hole excitons) is observed [29].

If resonant excitation is used, a coherent interaction is established with the energy levels in the dot. The energy transferred to the dot can be related directly to the probability of exciting the dot. Further to this, there is also a probability of exciting the dot, and then causing stimulated re-emission, and so on. In this way, an oscillation of excitation probability with increasing power has been observed [30, 31], termed Rabi oscillations.

1.4.2 Ensemble PL

When PL is recorded from an ensemble of quantum dots inhomogeneous broadening is observed due to the fluctuations in dot size. A spectrum from a dot ensemble is shown in Fig.1.3, excited with non-resonant 830 nm CW laser light. A bi-modal distribution is observed, with most dot emission occurring at 1.33 eV and 1.35 eV.

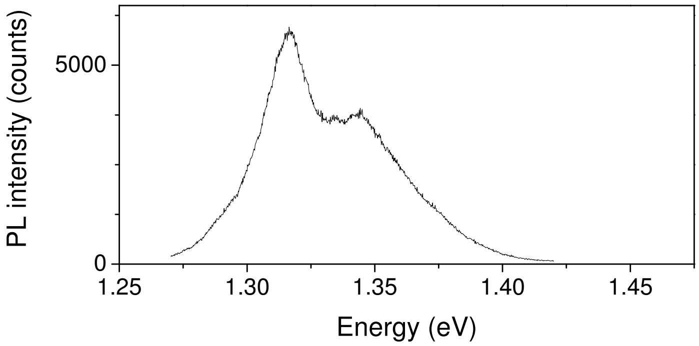

Figure 1.3: Photoluminescence spectra of an ensemble of dots. Image by Paul Dalgarno of Wafer no. 10311A (Referred to as Wafer A in later chapters).

1.4.3 Single dot PL

There are several methods available for achieving single quantum dot optical selection: Micron-sized aperture masks [32] can be deposited as a metallic layer onto the sample, and allow sub-diffraction limit resolution using a near-field microscope. Another near-field technique involves the use of a tapered metalised optical fibre positioned within several nanometers of the sample surface [33, 34]. Alternatively, lithographic sample etching can be used to define subwavelength-sized pillars in the sample, containing on average a single quantum dot [35, 36]. This has the advantage that the pillars can potentially form a microcavity. Confocal microscopy (see chapter 2), originally developed for observing single bio-molecules [37], is used in this work. Using a confocal setup the collectable PL emission is not limited by an aperture, and the excitation field strengths are easier to estimate. Lastly, low dot density samples (as used in this work) can potentially be used with any of the above techniques to aid in single quantum dot isolation.

Single quantum dot PL has none of the inhomogeneous broadening characteristics of the ensemble case, allowing a more detailed examination of the dot behaviour. The energy difference between single, double, and charged excitons in a single dot has a typical value of a few meV, easily measurable using a standard grating spectrometer with a nitrogen-cooled silicon-based CCD array, as used in this work. However, as we start to measure smaller values (such as the linewidth broadening of the negative trion due to tunneling ($\sim$0.03 meV) [38], the fine structure splitting of the neutral exciton (several tens of μeV) [39, 40, 41], or the fundamental linewidth of exciton emission (a few μeV) [42]) the $\sim$50 μeV resolution of the grating spectrometer becomes restrictive.

In order to overcome resolution problems resonant excitation of a single quantum dot can be performed using a narrowband laser (linewidth $\sim$0.001 μeV) to probe smaller energy scales than is possible with a grating spectrometer. However, precise laser tuning is difficult and expensive to monitor. A simpler approach is to embed the quantum dot into a charge-tunable heterostructure [43], and electronically tune the dot energy levels through the energy of the laser (See Chapter 3 section 3.5).

1.4.4 Anti-bunching

Single quantum dots are proven to be good single photon sources [44]. Anti-bunched emission has already been demonstrated [45, 46, 47] using the standard technique of auto-correlation, whereby individual photons are made incident onto a beamsplitter with two potential exit paths. Each exit path leads to one of two detectors, and detection of a photon starts/stops an electronic timer. A time correlated histogram of coincidence counts from each detector gives the relation [45, 48],

$$g^{(2)}(\tau) = \frac{\langle I(t)I(t+\tau)\rangle}{\langle I(t)\rangle^2}, \tag{1.2}$$

where $I(t)$ is the intensity measured by the first detector at an arbitrary time t and $I(t+\tau)$ is the intensity measured by the second detector with a delay of τ.

When a quantum dot is emitting a continuous stream of photons (as when excited with cw laser light) the normalised τ=0 point occurs as a dip in an otherwise straight line with g^2($\tau \neq 0$)=1. The exponential slope which forms the τ=0 dip is given by [45],

$$g^{(2)}(\tau) = 1 - e^{-(\Gamma+W_p)\tau}, \tag{1.3}$$

where Γ is the electron-hole recombination rate and W_p is the pump rate into the radiatively active upper state. The slope gives an indication of the repopulation and re-emission time of the dot, which is therefore dependent on the laser (pump) power and the electron hole recombination rate [45]. The g^2(τ=0) value can be taken as the fractional probability that the dot releases two or more photons.

When a quantum dot is emitting pulses of photons (as when excited with pulsed laser light) the g^2(t) value shows a series of peaks at the repetition period T. The g^2(τ=0) value is the area of the τ=0 peak measured as a fraction of the average area of the other peaks, and can be considered the fractional probability that the dot will release two or more photons per pulse.

An ideal single photon source will have g^2(τ=0)=0. g^2(τ=0) values of less than 0.02 have already been demonstrated using quantum dots excited non-resonantly [49, 50]. However, although optical control has been demonstrated [51] there is currently a lack of real-time electronic control over the output, which is addressed in this work.

1.4.5 Optical efficiency

Semiconductor quantum dots are extremely efficient at emitting light, in fact there is close to 100% probability that an excited dot will emit a photon when it is energetically allowed [44]. Unfortunately, efficient light collection is still a problem. Light can be emitted from the dot in any direction, and is emitted below the sample surface. A standard aspheric microscope objective lens with a numerical aperture (NA) of 0.6 will collect light over an angle θ perpendicular to the sample surface with the relation

$$NA = nsin\theta, \tag{1.4}$$

where n is the refractive index of the surrounding material. For $n = 1$ (air), $\theta = 36.8°$. Using the expression for the solid angle,

$$\Omega = 2\pi(1 - cos\theta), \tag{1.5}$$

the objective lens collects light from a solid angle of 0.4π streradians, equivalent to 10% ($\frac{\Omega}{4\pi}$) of any light emitted by a point source on the sample surface. However, due to the high refractive index of GaAs ($n = 3.5$) any light emitted from a quantum dot towards the sample surface experiences a large refraction effect at the semiconductor-vacuum interface. Using Snell's law,

$$n_1 sin\theta_1 = n_2 sin\theta_2, \tag{1.6}$$

only 0.03π steradians of the light emitted from the dot can be collected, equivalent to 0.74%.

There are several possible routes to achieving better collection efficiencies from semiconductor quantum dots: Bragg mirrors can be incorporated into the heterostructure design, such that if the dot emits a photon in the opposite direction to the objective lens the Bragg mirror will reflect the photon. Also, a microcavity design can be used (using the Bragg mirrors) to force the dot to emit preferentially into the cavity mode [36]. Lastly, the incorporation of a numerical aperture increasing lens into the system can minimise the refraction problems.

In this work the incorporation of Bragg mirrors into the system may have caused problems with respect to the charge-tunable structure, and a microcavity design may have interfered with the natural radiative lifetime of an exciton in the dot (through the Purcell effect). As such, in order to increase the collection efficiency solid immersion lens technology [52, 53] was incorporated into the system.

1.5 Electrical manipulation

A key advantage to using semiconductor quantum dots is the opportunity to embed them within a semiconductor heterostructure, allowing the dots to be manipulated electrically as well as optically. There are two main heterostructure designs: p-i-n diodes, and Schottky diodes.

1.5.1 p-i-n diodes

Quantum dots can be embedded within the intrinsic region of a p-i-n diode, which can be forward biased to allow an average of one or more excitons to fill the dot. This is normally a current controlled device, which can generally only be used to study charge-neutral excitons. In principle extremely low $g^2(0)$ values can be obtained with this device [54]. However, there is no electrical control over the exciton charge.

1.5.2 Schottky diodes

Quantum dots can be embedded within a charge-tunable structure, near to an n-doped or p-doped Fermi-sea (Back contact). A Schottky diode is a voltage controlled device (there is no d.c. current flow), with the voltage used to manipulate the dot energy-levels with respect to the Fermi level. In the Schottky device used in this work the back contact is n-doped. Voltage controlled tunneling allows absolute control over the number of majority carriers (electrons) in the dot through the Coulomb blockade, and optical excitation provides the minority carrier (the holes). In a p-doped device the dot is manipulated in the same fashion, but the majority carrier is the hole and the minority carrier is the electron.

Single majority carrier charging of an exciton is possible using a Schottky diode-based device. Minority carrier storage is possible, using a voltage to prevent majority carriers entering the dot (see Chapter 3). Dot energy levels can be tuned through the resonance of a narrowband laser electronically, instead of tuning the laser (see Chapter 3 section 3.5) [55].

1.6 GHz electrical manipulation

The focus of this work is an approach to applying GHz bandwidth electrical pulsing to a semiconductor quantum dot. Radiative recombination of an exciton in a single quantum dot can be expected to occur within $\sim$1 ns. The ability to control carrier occupation of the dot on this timescale leads to some interesting physics, most notably the potential for an electrically triggered and controllable qubit.

Progress has already been made towards GHz manipulation. There have already been several successful electrically driven single photon sources based on a p-i-n diode structure [56, 57, 58]. Also, charge-tunable structures have been manipulated with fast electrical switching to allow carrier spin-initialisation and read-out [59], with the potential for an additional spin manipulation step [60]. In this way, there is already a level of control available with regards to the individual components of a qubit.

In this work, GHz exciton charging is demonstrated in a charge tunable device. The device is shown to be capable of electrically triggering single photon emission with a GHz voltage pulse. Lastly, optical spin initialisation and read-out is performed using GHz pulses to tune the neutral exciton transition energy into resonance with the emission from a narrowband laser and then charge the exciton. This work is an advancement on current standards because these operations can be performed using one device, with greater control than previously shown.

1.7 Conclusion

Quantum dots are a viable source of single and entangled photons, and capable of charge and spin storage. They can be grown within a solid-state heterostructure, which allows both optical and electrical control, and affords several solutions to the inherent challenges of selecting single dots and improving optical extraction efficiencies. This research represents an advancement towards full electrical control over the optical emission of a single quantum dot, which will ultimately benefit the fields of quantum cryptography and quantum computing.

References

[1] N. Gisin, G. Ribordy, W. Tittel and H. Zbinden, *Quantum cryptography.* Reviews of Modern Physics, **74**, 145 (2002).

[2] R. J. Warburton, *Self-assembled semiconductor quantum dots.* Contemporary Physics, **43**, 351 (2002).

[3] P. A. Hiskett, D. Rosenberg, C. G. Peterson, R. J. Hughes, S. Nam, A. E. Lita, A. J. Miller and J. E. Nordholt, *Long-distance quantum key distribution in optical fibre.* New Journal of Physics, **8**, 193 (2006).

[4] D. P. DiVincenzo, *The physical implementation of quantum computing.* ArXiv, quant-ph/0002077v3 (2000).

[5] E. Knill, R. Laflamme and W. H. Zurek, *Resilient quantum computation.* Science, **279**, 342 (1998).

[6] F. Schmidt-Kaler, H. Häffner, M. Reibe, S. Gulde, G. P. T. Lancaster, T. Deuschle, C. Becher, C. F. Roos, J. Eschner and R. Blatt, *Realization of the Cirac-Zoller controlled-NOT quantum gate.* Nature, **422**, 408 (2003).

[7] F. Diedrich and H. Walthner, *Nonclassical radiation of a single stored ion.* Physical Review A, **58**, 203 (1987).

[8] D. Loss and D. P. DiVincenzo, *Quantum computation with quantum dots.* Physical Review A, **57**, 120 (1998).

[9] L. M. K. Vandersypen, M. Steffen, G. Breyta, C. S. Yannoni, M. H. Sherwood and I. L. Chuang, *Experimental realization of Shor's quantum factoring algorithm using nuclear magnetic resonance.* Nature, **414**, 883 (2001).

[10] T. R. Beals, J. Vala and K. B. Whaley, *Scalability of quantum computation with addressable optical lattices.* Physical Review A, **77**, 052309 (2008).

[11] B. D. Gerardot, G. Subramanian, S. Minivelle, H. Lee, J. A. Johnson, W. V. Schoenfeld, D. Pine, J. S. Speck and P. M. Petroff, *Self-assembling quantum dot lattices through nucleation site engineering.* Journal of Crystal Growth, **236**, 647 (2002).

[12] A. K. Ekert, *Quantum cryptography based on Bell's theorem.* Physical Review Letters, **67**, 661 (1991).

[13] D. Bouwmeester, J. Pan, K. Mattle, M. Eibl, H. Weinfirter and A. Zeilinger, *Experimental quantum teleportation.* Nature, **390**, 575 (1997).

[14] E. Moreau, I. Robert, L. Manin, V. Thierry-Mieg, J. M. Gérard and I. Abram, *Quantum cascade of Photons in Semiconductor Quantum Dots.* Physical Review Letters, **87**, 183601 (2001).

[15] R. M. Stevenson, R. J. Young, P. Atkinson, K. Cooper, D. A. Ritchie and A. J. Shields, *A semiconductor source of triggered entangled photon pairs.* Nature, **439**, 179 (2006).

[16] U. Bockelmann and G. Bastard, *Phonon scattering and energy relaxation in two-, one-, and zero-dimensional electron gases.* Physical Review B, **42**, 8947 (1990).

[17] J. Urayama, T. B. Norris, J. Singh and P. Bhattacharya, *Observation of phonon bottleneck in quantum dot electronic relaxation.* Physical Review Letters, **86**, 4930 (2001).

[18] Y. Toda, O. Moriwaki, M. Nishioka and Y. Arakawa, *Efficient carrier relaxation mechanism in InGaAs/GaAs self-assembled quantum dots based on the existence of continuum states.* Physical Review Letters, **82**, 4114 (1999).

[19] R. Heitz, M. Veit, N. N. Ledentsov, A. Hoffmann, D. Bimberg, V. M. Ustinov, P. S. Kop'ev and Zh. I. Alferov, *Energy relaxation by multiphonon processes in InAs/GaAs quantum dots.* Physical Review B, **56**, 10435 (1997).

[20] X. Li, H. Nakayama and Y. Arakawa, *Phonon bottleneck in quantum dots: Role of lifetime of the confined optical phonons.* Physical Review B, **59**, 5069 (1999).

[21] U. Bockelmann and T. Egeler, *Electron relaxation in quantum dots by means of Auger processes.* Physical Review B, **46**, 15574 (1992).

[22] A. V. Uskov, J. McInerney, F. Adler, H. Schweizer and M. H. Pilkuhn, *Auger carrier capture kinetics in self-assembled quantum dot structures.* Applied Physics Letters, **72**, 58 (1998).

[23] B. Ohnesorge, M. Albrecht, J. Oshinowo, A. Forchel and Y. Arakawa, *Rapid Carrier relaxation in self-assembled* $In_xGa_{1-x}As/GaAs$ *quantum dots.* Physical Review B, **54**, 11532 (1996).

[24] P. A. Dalgarno, J. M. Smith, J. McFarlane, B. D. Gerardot, K. Karrai, A. Badolato, P. M. Petroff and R. J. Warburton *Coulomb interactions in single*

charged self-assembled quantum dots: Radiative lifetime and recombination energy. Physical Review B, **77**, 245311 (2008).

[25] D. Leonard, K. Pond and P. M. Petroff, *Critical layer thickness for self-assembled InAs islands on GaAs.* Physical Review B, **50**, 11687 (1994).

[26] J. M. Garcia, G. Medeiros-Ribeiro, K. Schmidt, T. Ngo, J. L. Feng, A. Lorke, J. Kotthaus and P. M. Petroff, *Intermixing and shape changes during the formation of InAs self-assembled quantum dots.* Applied Physics Letters, **71**, 2014 (1997).

[27] H. Eisele, A. Lenz, R. Heitz, R. Timm, M. Dähne, Y. Temko, T. Suzuki and K. Jacobi, *Change of InAs/GaAs quantum dot shape and composition during capping.* Journal of Applied Physics, **104**, 124301 (2008).

[28] P. A. Frantsuzov and R. A. Marcus, *Explanation of quantum dot blinking without the long-lived trap hypothesis.* Physical Review B, **72**, 155321 (2005).

[29] J. M. Smith, P. A. Dalgarno, B. Urbaszek, E. J. McGhee, G. S. Buller, G. J. Nott, R. J. Warburton, J. M. Garcia, W. Schoenfeld and P. M. Petroff, *Carrier storage and capture dynamics in quantum-dot heterostructures.* Applied Physics Letters, **82**, 3761 (2003).

[30] T. H. Stievater, X. Li, D. G. Steel, D. Gammon, D. S. Katzer, D. Park, C. Piermarocchi and L. J. Sham, *Rabi oscillations of excitons in single quantum dots.* Nature, **418**, 612 (2002).

[31] A. Zrenner, E. Beham, S. Stufler, F. Findeis, M. Bichler and G. Abstreiter, *Coherent properties of a two-level system based on a quantum-dot photodiode.* Nature, **418**, 612 (2002).

[32] G. Gammon, E. S. Snow, B. V. Shanabrook, D. S. Katzer and S. Park, *Homogeneous linewidths in the optical spectrum of a single gallium arsenide quantum dot.* Science, **273**, 87 (1996).

[33] C. Obermüller, A. Deisenrieder, G. Abstreiter, K. Karrai, S. Grosse, S. Manus, J. Feldmann, H. Lipsanen, M. Sopanen and J. Ahopelto, *Pauli-blocking imaging of single strain-induced semiconductor quantum dots.* Applied Physics Letters, **74**, 3200 (1999).

[34] K. Karrai and R. D. Grober, *Piezoelectric tip-sample distance control for near field optical microscopes.* Applied Physics Letters, **66**, 1842 (1995).

[35] M. Bayer, O. Stern, P. Hawrylak, S. Fafard, A. Forchel, *Hidden symmetries in the energy levels of excitonic 'artificial atoms'.* Nature, **405**, 923 (2000).

[36] C. Santori, *A brighter source of single photons.* Nature Photonics, **1**, 686 (2007).

[37] S. Weiss, *Fluorescence spectroscopy of single biomolecules.* Science, **283**, 1676 (1999).

[38] J. M. Smith, P. A. Dalgarno, R. J. Warburton, A. O. Govorov, K. Karrai, B. D. Gerardot and P. M. Petroff, *Voltage control of the spin dynamics of an exciton in a semiconductor quantum dot.* Physical Review Letters, **94**, 197402 (2005).

[39] B. Urbaszek, R. J. Warburton, K. Karrai, B. D. Gerardot, P. M. Petroff and J. M. Garcia, *Fine structure of highly charged excitons in semiconductor quantum dots.* Physical Review Letters, **90**, 247403 (2003).

[40] M. Bayer, G. Ortner, O. Stern, A. Kuthner, A. A. Gorbunov, A. Forchel, P. Hawrylak, S. Fafard, K. Hinzer, T. L. Reinecke, S. N. Walck, J. P. Reithmaier, K. Klopf and F. Schäfer, *Fine structure of neutral and charged excitons in self-assembled In(Ga)As/(Al)GaAs quantum dots.* Physical Review B, **65**, 195315 (2002).

[41] A. Högele, S. Seidl, M. Kroner, K. Karrai, R. J. Warburton, B. D. Gerardot and P. Petroff, *Voltage-controlled optics of a quantum dot.* Physical Review Letters, **93**, 217401 (2004).

[42] S. Seidl, M. Kroner, P. A. Dalgarno, A. Högele, J. M. Smith, M. Ediger, B. D. Gerardot, J. M. Garcia, P. M. Petroff, K. Karrai and R. J. Warburton, *Absorption and photoluminescence spectroscopy on a single self-assembled charge-tunable quantum dot.* Physical Review B, **72**, 195339 (2005).

[43] R. J. Warburton, C. Schaflein, D. Haft, F. Bickel, A. Lorke, K. Karrai, J. M. Garcia, W. Schoenfeld and P. M. Petroff, *Optical emission from a charge-tunable quantum ring.* Nature, **405**, 926 (2000).

[44] V. Zwiller, T. Aichele and O. Benson, *Quantum optics with single quantum dot devices.* New Journal of Physics, **6**, 96 (2004).

[45] P. Michler, A. Imamoglu, M. D. Mason, P. J. Carson, G. F. Strouse and S. K. Buratto, *Quantum correlation among photons from a single quantum dot at room temperature.* Nature, **406**, 968 (2000).

[46] P. Michler, A. Kiraz, C. Becher, W. V. Schoenfeld, P. M. Petroff, L. Zhang, E. Hu and A. Imamoglu, *A quantum dot single-photon turnstile device.* Science, **290**, 2282 (2000).

[47] V. Zwiller, H. Blom, P. Jonsson, N. Panev, S. Jeppesen, T. Tsegaye, E. Goobar, M. Pistol, L. Samuelson and G. Björk, *Single quantum dots emit single photons at a time: Antibunching experiments.* Applied Physics Letters, **78**, 2476 (2001).

[48] Louden, *The Quantum Theory of Light.* Clarendon-press, Oxford (1973).

[49] A. J. Shields, *Semiconductor quantum light sources.* Nature Photonics, **1**, 215 (2007).

[50] C. Böckler, S. Reitzenstein, C. Kistner, R. Debusmann, A. Löffler, T. Kida, S. Höfling, A. Forchel, L. Grenouillet, J. Claudon and J. M. Gerard, *Electrically driven high-Q quantum dot-micropillar cavities.* Applied Physics Letters, **92**, 091107 (2008).

[51] C. Santori, M. Pelton, G. Solomon, Y. Dale and Y. Yamamoto, *Triggered single photons from a quantum dot.* Physical Review Letters, **86**, 1502 (2001).

[52] S. Moehl, H. Zhao, B. Dal Don, S. Wachter and H. Kalt, *Solid immersion lens-enhanced nano-photoluminescence.* Journal of Applied Physics, **93**, 6265 (2003).

[53] V. Zwiller and G. Björk, *Improved light extraction from emitters in high refractive index materials using solid immersion lenses.* Journal of Applied Physics, **92**, 660 (2002).

[54] A. Imamoglu and Y. Yamamoto, *Turnstile device for heralded single photons: Coulomb blockade of electron and hole tunneling in quantum confined p-i-n heterojunctions.* Physical Review Letters, **72**, 210 (1994).

[55] B. Alen, F. Bickel, K. Karrai, R. J. Warburton and P. M. Petroff, *Stark-shift modulation absorption spectroscopy of single quantum dots.* Applied Physics Letters, **83**, 2235 (2003).

[56] Z. Yuan, B. E. Kardynal, R. M. Stevenson, A. J. Shields, C. J. Lobo, K. Cooper, N. S. Beattie, D. A. Ritchie and M. Pepper, *Electrically driven single-photon source.* Science, **295**, 102 (2002).

[57] M. B. Ward, T. Farrow, P. See, Z. L. Yuan, O. Z. Karimov, A. J. Bennett, A. J. Shields, P. Atkinson, K. Cooper and D. A. Ritchie, *Electrically driven telecommunication wavelength single-photon source.* Applied Physics Letters, **90**, 063512 (2007).

[58] T. Farrow, P. See, A. J. Bennett, M. B. Ward, P. Atkinson, K. Cooper, D. J. P. Ellis, D. C. Unitt, D. A. Ritchie and A. J. Shields, *Single-photon emitting diode based on a quantum dot in a micro-pillar.* Nanotechnology, **19**, 345401 (2008).

[59] D. Heiss, V. Jovanov, M. Bichler, G. Abstreiter and J. J. Finley, *A charge and spin readout scheme for single self-assembled quantum dots.* Physical Review B, **77**, 235442 (2008).

[60] V. Jovanov, *Talk: QD2008.* Gyeongju, Korea, (2008).

Chapter 2

Experimental setup

Quantum dots embedded within a charge tunable structure can be manipulated electronically and optically. The challenges of using GHz bandwidth voltage pulses across a single quantum dot for fast opto-electronic manipulation necessitated changes to the standard confocal setup originally used. Polarisation optics were included in order to perform polarisation-based filtering of the dot PL. The standard electronics had a far too large attenuation at GHz frequencies, so sub-ns rise-time cabling was included to carry fast pulses from a pulse pattern generator to the sample without significant attenuation. The efficiency of the collection optics was also improved by incorporating a super-hemispherical solid immersion lens into the system, and the timing of the triggering systems was re-vamped to account for the setup changes. Lastly both a Hanbury Brown-Twiss interferometer and spectrometer were set up, with additional measurements being made to help improve the signal to noise ratio of the system during single photon studies.

2.1 Confocal Microscope

The original experimental setup did not include any control over the polarisation of the excitation laser, or any ability to analyse the polarisation of the PL [1]. Here is a discussion of the confocal setup of the microscope and the changes made in order to add polarisation control.

2.1.1 Original setup

The original setup of the microscope head is shown in Fig. 2.1. The excitation laser light is collimated from a single-mode optical fibre with a NA = 0.25 aspheric lens (Thorlabs C220TM-B) to a $\sim$ 4 mm full width at half maximum (FWHM) diameter beam. The beam is then split by a 5 mm thick glass positioned at a 45 degree angle to the incident beam. Approximately 96% of the light passes through the glass and onto a Si detector which allows measurements of the excitation power. The other $\sim$ 4% is reflected down to a 0.65 NA (Thorlabs C380TM-B) objective lens and is focused onto the sample. Both PL from the quantum dot and reflected laser light are collimated by the same objective lens and $\sim$ 96% passes through the first beamsplitter. A second beamsplitter of the same type as the first has two functions. The first is to reflect $\sim$ 4% of the remaining laser light and PL so that it is focused on a CCD camera, allowing the observation of a representation of the laser spot on the sample. The second is to correct the deviation caused by the first beamsplitter due to refraction, and to allow $\sim$ 96% of the light to pass through a second 0.25 NA aspheric lens (Thorlabs C220TM-B) so it can be coupled into a second single-mode fibre.

In this arrangement the microscope can be considered confocal [2]. The small core size ($\sim$7 μm) of each optical fibre creates the pinhole used in standard confocal microscopy, and the line spread function of the collection fibre determines the resolution of the microscope.

2.1.2 Polarisation optics

Polarisation optics were included in order to allow more choice over excitation and collection conditions. For instance, they allow the laser light to be filtered out from the PL during resonant experiments (as performed in Chapter 5). They also allow the excitation of the dot with a hole of known spin [3, 4, 5, 6]. Also, it is possible to use the polarisation to increase the fraction of light which reflects off the first beamsplitter down to the sample. Presented in Fig. 2.2 are the optics that have been added to the microscope head.

The Glan-Taylor (GT) linear polariser and the $\frac{\lambda}{2}$ plate in the excitation arm were included so that the elliptical polarisation coming from the excitation fibre can be cleaned up and rotated. The light is then incident on the first beamsplitter (refractive index $n_t = 1.5$) at an angle of incidence (θ_i) of 45°, and the polarisation dependence

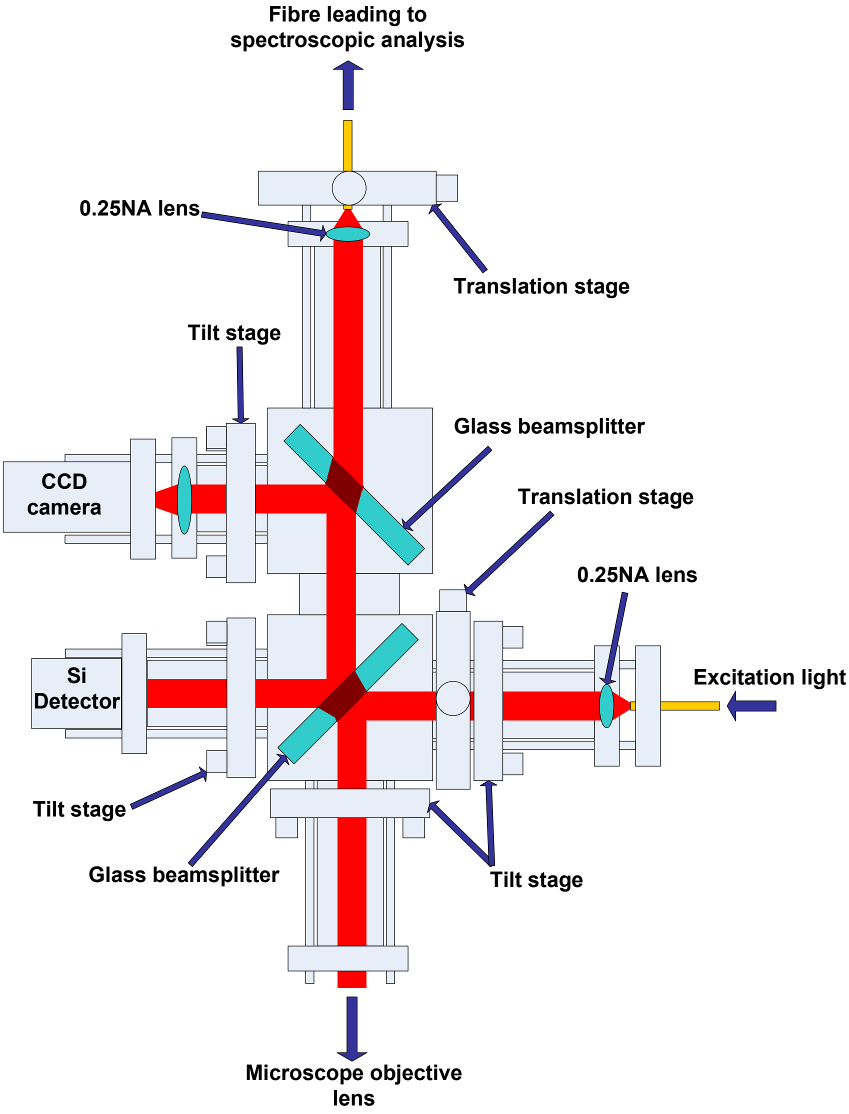

Figure 2.1: A schematic diagram of the original microscope head.

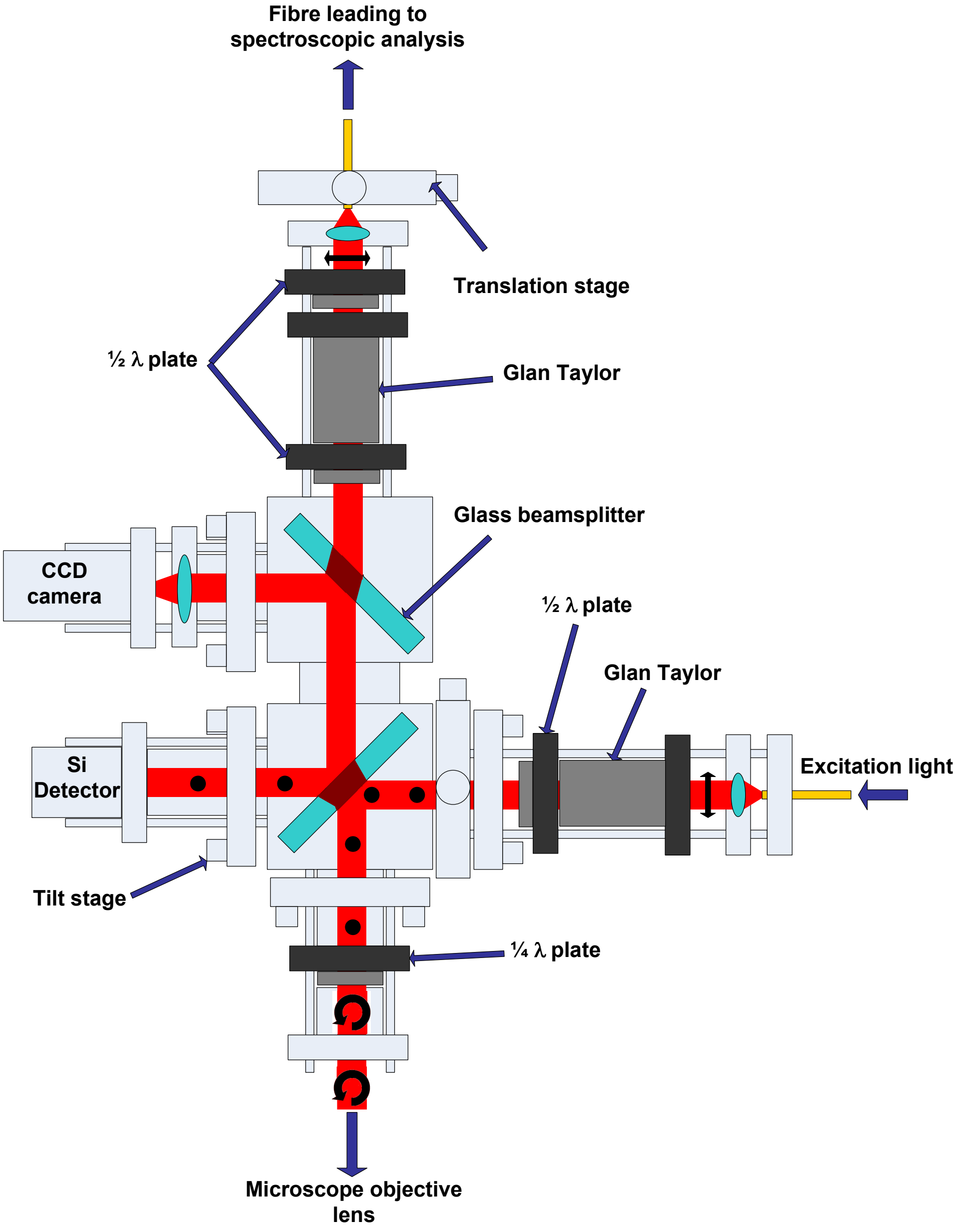

Figure 2.2: A schematic diagram of the microscope head including the polarisation optics added to give control over the excitation and detection polarisation. Also shown is an example of the polarisation change in a light pulse as it passes through the polarisation optics before it reaches the sample.

of the fraction of reflected light is given by the Fresnel equations

$$r_{\perp} = -\frac{\sin(\theta_i - \theta_t)}{\sin(\theta_i + \theta_t)} \tag{2.1}$$

and

$$r_{\parallel} = \frac{\tan(\theta_i - \theta_t)}{\tan(\theta_i + \theta_t)}, \tag{2.2}$$

where $r_{\perp}$ is the amplitude reflection coefficient for light polarised perpendicular to the plane of incidence, and $r_{\parallel}$ is the amplitude reflection coefficient for light polarised parallel to the plane of incidence. θ_t is the angle of transmission, given by Snell's law

$$n_i sin\theta_i = n_t sin\theta_t \tag{2.3}$$

where $n_i = 1$ is the refractive index of air. The total reflected intensity is given by $R = r^2$, and as such it can be seen that the maximum reflected intensity possible is 9.2% using light polarised perpendicular to the beamsplitter plane of incidence. Conversely, the minimum reflected intensity possible is 0.85% using light polarised parallel to the beamsplitter plane of incidence. It was desirable that the sample could be excited with the maximum power available from the laser. Calibration of the GT and the $\frac{\lambda}{2}$ plate in the excitation arm was achieved by maximising the power on the Si detector in the microscope head using the GT so as to use the highest intensity polarisation which comes from the excitation fibre, and then minimising the power on the Si detector using the $\frac{\lambda}{2}$ plate so that the maximum ∼9% of the available light is reflected down to the sample. In this way, the polarisation reflected from the first beamsplitter down to the $\frac{\lambda}{4}$ plate is always polarised perpendicularly to the beamsplitter plane of incidence.

The $\frac{\lambda}{4}$ plate is calibrated by replacing the objective lens and sample with a polarising beamsplitter and two Si detectors as shown in Fig. 2.3. The laser intensity on each detector was then measured as a function of the microscope head $\frac{\lambda}{4}$ plate angle. When the linearly polarised light reflected from the beamsplitter is incident on the fast or slow axis of the $\frac{\lambda}{4}$ plate, the light will remain linearly polarised with the same orientation. When the light is incident on the $\frac{\lambda}{4}$ plate at a polarisation rotated 45° clockwise from the fast axis, the light will continue with right-hand circular polarisation. When the light is incident on the $\frac{\lambda}{4}$ plate at a polarisation rotated 45° counter-clockwise from the fast axis, the light will continue with left-hand circular polarisation.

In a perfect system, when linear polarisation is incident on the polarising beamsplitter in Fig. 2.3, detector 1 will record all the signal, but when the output is circular (regardless of whether left- or right-handed) both detectors will see half of the available power.

The results are displayed in Fig. 2.4, alongside a fit based on Malus' law (blue

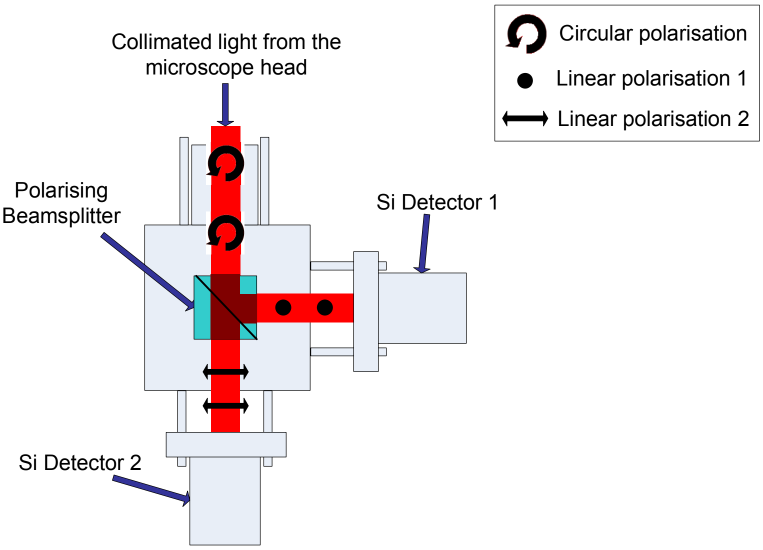

Figure 2.3: Schematic of the polarising beamsplitter used to align the polarisation optics in the head. Depending on the polarisation of the incident beam, the beamsplitter will reflect or transmit the light to either detector at different ratios.

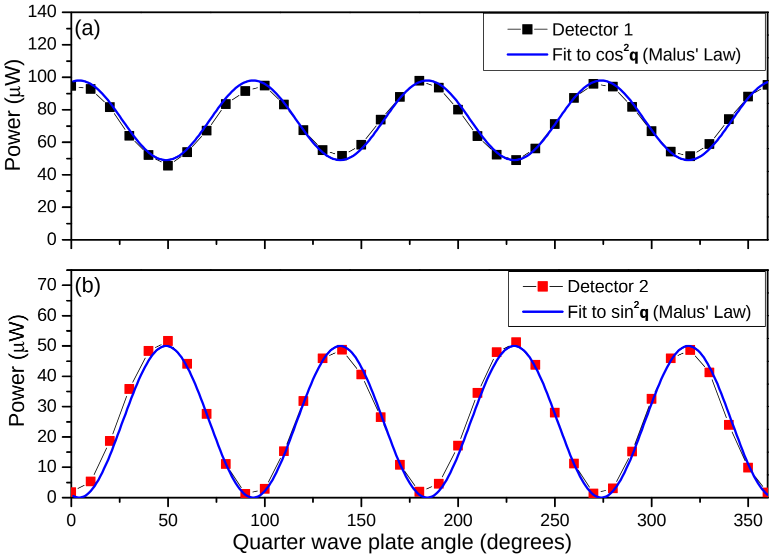

Figure 2.4: The intensity at each detector in Fig. 2.3 as the $\frac{\lambda}{4}$ plate in the microscope head (Fig. 2.2) is rotated. In (a) the blue line is $\cos^2(\theta)$ plotted against the data from detector 1 (black squares), with a maximum power of 98 μW and a peak-to-peak amplitude of 49 μW. In (b) the blue line is $\sin^2(\theta)$ plotted against the data from detector 2 (red squares), with a maximum power of 50 μW and a peak-to-peak amplitude of 50 μW. In both (a) and (b) the $\cos^2(\theta)$ and $\sin^2(\theta)$ plots are exactly out of phase, with a period of 90^{o}.

lines). At $\theta \approx 4^{o}$, 94^{o}, 184^{o} and 274^{o} detector 1 records a maximum power while detector 2 records close to zero signal, confirming that the output polarisation from the microscope head is linear at those $\frac{\lambda}{4}$ plate angles. At $\theta \approx 49^{o}$ and 229^{o} the polarisation of the incident light is rotated approximately 45^{o} counter-clockwise from the fast axis (marked on the $\frac{\lambda}{4}$ plate), detector 1 records a minimum power, and detector 2 records a maximum power. This confirms that the polarisation from the head is left-hand circularly polarised at those $\frac{\lambda}{4}$ plate angles. Lastly, at $\theta \approx 139^{o}$ and 319^{o} the polarisation of the incident light is rotated approximately 45^{o} clockwise from the fast axis, and again detector 1 records a minimum power and detector 2 records a maximum power, confirming that the polarisation from the head is right-hand circularly polarised at those $\frac{\lambda}{4}$ plate angles.

In the microscope head collection arm the first $\frac{\lambda}{2}$ plate was included in order to rotate the linearly polarised light such that only one polarisation (i.e. that of the laser or the dot PL) is allowed to propagate through the GT. The GT is not rotated, as this might disturb the alignment. The second $\frac{\lambda}{2}$ plate can be adjusted to aid the coupling to the collection single mode fibre, because the spectrometer has a polarisation dependence.

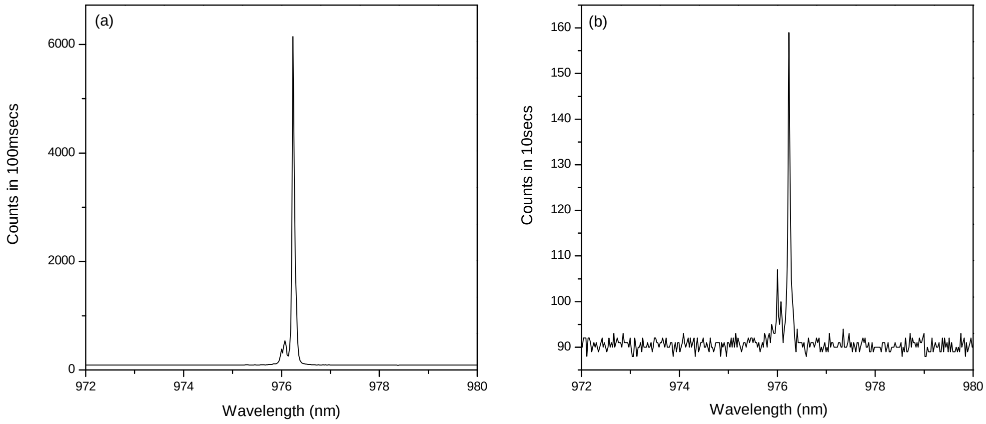

Figure 2.5: Graph of the laser peak (at 976.236 nm) (a) maximised and (b) minimized using the polarisation optics in the microscope head to excite the sample with left-hand circularly polarised light. The polarisation optics in the collection arm of the head are then adjusted to (a) allow or (b) disallow the reflected laser light to be coupled into the collection single mode fibre. The ~90 count baseline observed in (b) is due to read-out noise from the spectrometer CCD camera. The smaller peaks in (a) and (b) at 976 nm and 976.071 nm are due to laser mode-hopping.

This setup has the advantage that the laser polarisation can also be checked in-situ during experiments on a single quantum dot without disturbing the alignment. The polarisation of the exciting laser can be considered perfectly circularly polarised if the reflected laser light from the sample can be extinguished using polarisation filtering. Shown in Fig. 2.5 is an example of filtering the laser using only polarisation, giving an extinction down to 0.027%.

2.2 Spectrometer

A Princeton Instruments spectrometer is used to disperse spectrally the PL from the dot. As shown in Fig. 2.6, there are three different blazed gratings (300, 1200 and 1800 lines per mm) which allow different bandwidths to be analysed by the nitrogen-cooled CCD camera. The 1200 lines per mm-grating gives a resolution of ~50 μeV when incident on the CCD camera, and a movable mirror allows a bandwidth of ~0.5 meV to be coupled into a 50 μm multimode fibre which connects to a silicon SPAD. Finally, a holographic notch filter (centre wavelength 827 nm, spectral bandwidth 36 nm) purchased from Clairet Scientific Ltd. is included in the input coupling optics in order to filter out any reflected laser light from non-resonant excitation at 830 nm.

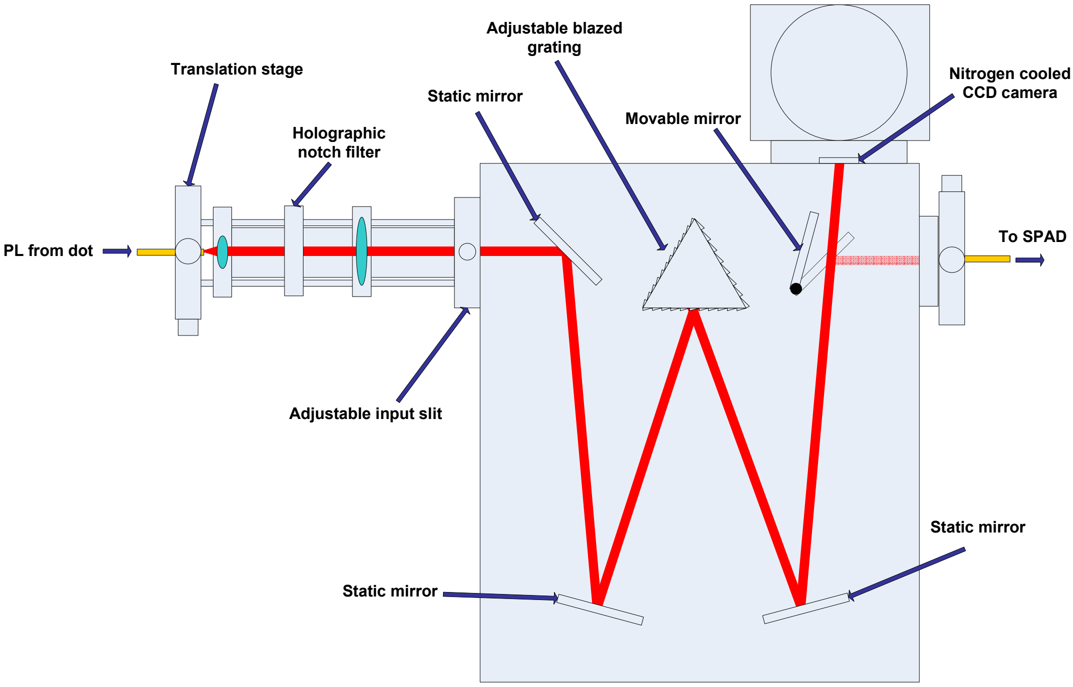

Figure 2.6: Schematic of the spectrometer setup.

2.3 Hanbury Brown-Twiss Interferometer

A Hanbury Brown-Twiss (HBT) interferometer (Fig. 2.7)[1] was used in order to correlate time differences between photons from a single quantum dot. An HBT overcomes the inherent dead time of 50 ns associated with the Si-based single photon avalanche detectors (SPADs) used for single photon detection by using two detectors. The movable mirrors allowed the selection of a ~50 μeV bandwidth from the available light

---

[1] constructed by Daniel Brunner

(using a single mode input and output fibre [7]), and as such it was possible to measure correlations between excitons provided they were suitably chromatically isolated from other light sources.

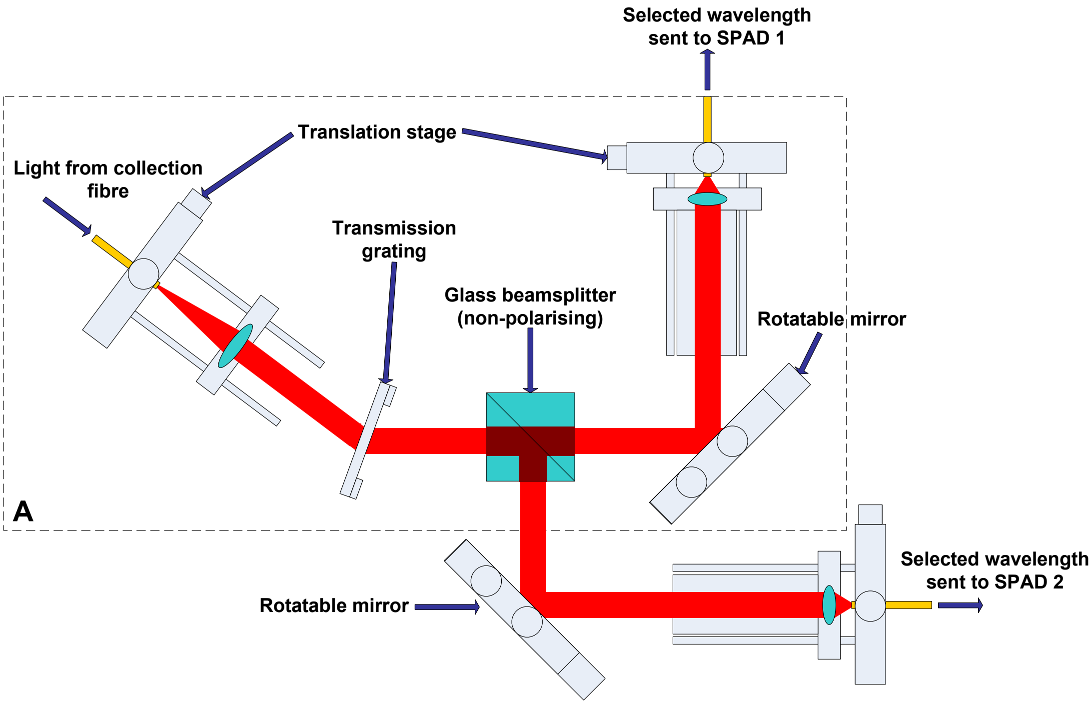

Figure 2.7: Schematic of the Hanbury Brown-Twiss setup. Any light incident on the grating will be diffracted, and then passes through the beamsplitter. The movable mirrors allow selective chromatic coupling into each fibre with a throughput of ~29%. If the beamsplitter is removed, **A** defines the section which can be used as a wavelength tunable filter.

In order to calibrate the HBT, a broadband white light source was coupled into the input fibre and each output fibre was individually coupled into the spectrometer. This allowed the rotatable mirrors to be adjusted, so the correct wavelengths are selected for coupling into each fibre. Dot PL is then coupled into the input fibre (the collection fibre from the microscope head), and the output fibres are connected to two SPADs. Fine adjustments can be made to the rotatable mirrors and translation stages using the dot PL detection rate from each SPAD.

SPADs

The SPADs used in this project were made by Perkin Elmer optoelectronics (Part number SPCM-AQR-15-FC). The have a jitter of ~400 ps FWHM between successive single photon measurements, a dark count rate of ~80 Hz, and an quantum efficiency of ~25 % at 950 nm. Silicon avalanche photodiodes emit a small quantity of broadband light on detection of a photon, which can be detected by the second

SPAD in the HBT. This has been observed in autocorrelations when the PL rate from the dot was extremely low (Fig. 2.8).

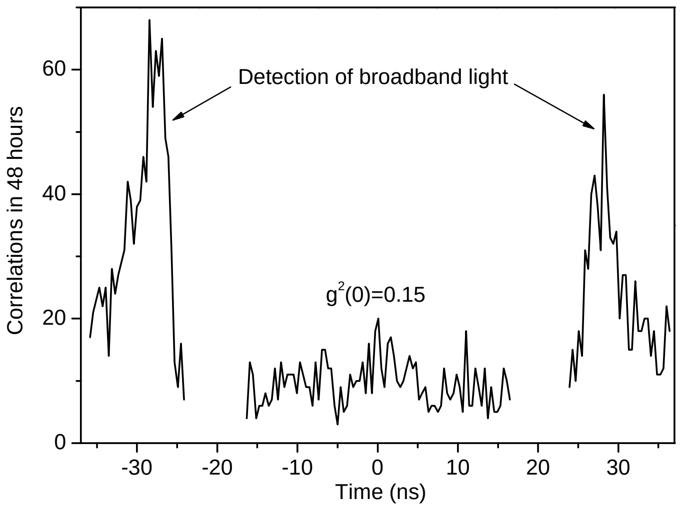

Figure 2.8: Pulsed autocorrelation (abridged) of X^{1-} PL for a single dot (taken from Fig. 5.19 in Chapter 5). Included is the $g^2(t \backsimeq 0)$ region, and the signal at $t \backsimeq \pm 27$ ns due to the detection of broadband light. Initial detection of dot PL at t=0 results in the emission of broadband light by the SPAD. Reflections of the emitted light are detected at $t \backsimeq \pm 27$ ns by the other SPAD.

2.3.1 Wavelength tunable filter

A simple adjustment to the HBT setup is shown as **A** in Fig.2.7. The beamsplitter is removed, allowing the efficient use of the equipment as a tunable filter. This was used in two different ways. Firstly, using a 50 μm multimode input fibre (in order to conserve the excitation power) and a single mode output fibre which then connects to the excitation arm of the microscope head, the tunable filter could be used to select a 0.37 meV bandwidth region from a broadband pulsed laser, which was then used to resonantly excite a dot. Secondly, using a single mode input fibre from the collection arm of the microscope head (in order to maintain a small collection spot size at the sample, see section 2.1.1) and a 50 μm multimode output fibre connected to a spectrometer or single photon detector, a single exciton PL line could be preferentially filtered (from other dot emission and any reflected laser light) and measured, while still collecting the maximum amount of light (58.1% [7]). These combinations were more preferable than using single mode fibres for both input and ouput coupling, which gave a throughput of 25% and a bandwidth of 0.05 meV [7].

2.4 PL power dependence and TRPL

2.4.1 PL power dependence

The power dependence of PL from a dot which has been optically excited with non-resonant laser light is an important parameter in several effects observed in this work. In order to investigate the power dependence of any particular effect, it is important to understand first how a dot normally responds to increasing optical excitation. In Fig. 2.9 a single dot was excited with 830 nm cw laser light, and the emitted PL was recorded with the spectrometer. The integrated count rate of the X^0 and X^{1-} PL peaks were recorded against increasing power. The PL for both excitons rises approximately linearly with increasing power until $\sim 8\ \mu\mathrm{W}\ \mu\mathrm{m}^{-2}$, where the PL stops increasing. The point at which the PL stops increasing with power is generally referred to as the PL saturation point, and varies from dot to dot. Beyond this power the PL emission rate starts to decrease again as it becomes more likely that other excitons will preferentially form in the dot. In most instances, measurements are taken at lower power than this saturation value.

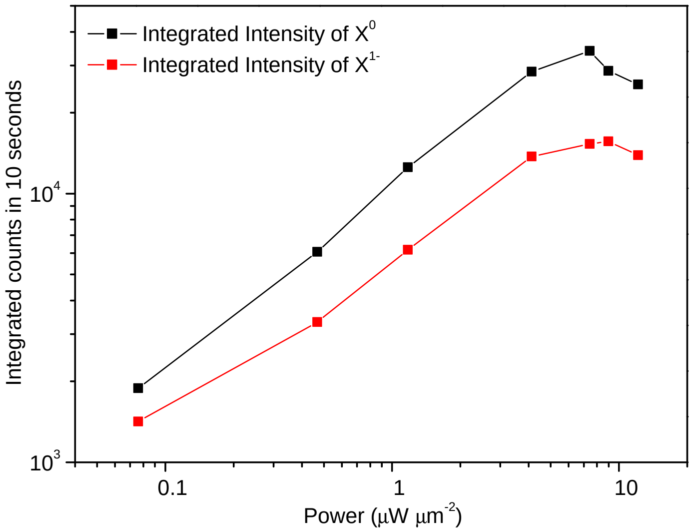

Figure 2.9: The integrated exciton PL counts versus excitation power for X^0 and X^{1-} from a single quantum dot excited with 830 nm cw laser light.

2.4.2 Time correlated single photon counting and saturation

Time-correlated single photon counting (TCSPC) is performed at several points in this work, in order to record time-resolved PL (TRPL) measurements of exciton decay. TCSPC records a histogram of many thousands of timing events, and gives a measurement of the time-averaged probability that a photon will arrive at the detector at each measured time-window. The TRPL in this work was generally performed by exciting the dot with 100 ps pulses of 826 nm laser light and recording the PL using a SPAD with a jitter of ~400 ps. An exponential decay is then convolved with the laser pulse shape as recorded by the SPAD and fit to the data, in order to obtain the lifetime values (τ_1 and τ_2 in Fig. 2.10) of the exciton radiative decay. As observed previously [8], higher power scans (close to the PL saturation power) exhibit saturation effects due to multi-exciton cascades, causing the decay shape to deform. Saturation effects are normally observed in TRPL at a much lower power than simply by observing the PL rate (as in Fig. 2.9). For this reason, TRPL is performed only at low powers, generally ~ 0.1 of the PL saturation power.

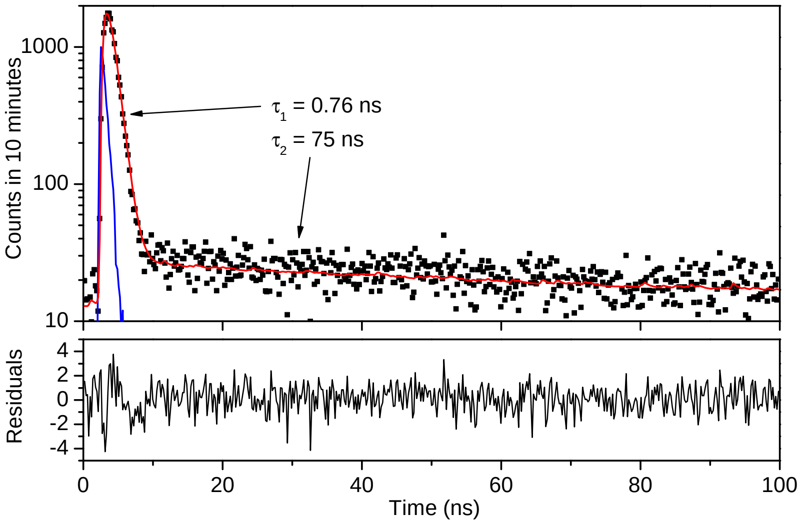

Figure 2.10: TCSPC of X^0 PL from a dot in Wafer B (see section 2.6.2) excited non-resonantly with 100 ps pulses of 826 nm laser light at an average power 136 nW μm^{-2}, and a repetition rate of 10MHz. A bi-exponential decay (τ_1 and τ_2) has been convolved with the temporal response of the detector (blue line). The result (red line) is successfully fitted to the data (black dots) using τ_1=0.76 ns and τ_2=75 ns. The residuals to the fit (black line) shows the difference between the fit and the data.

When taking TRPL measurements, light is normally coupled into the spectrometer from a single mode fibre (from the microscope head collection arm, Fig. 2.2) and collected at the exit aperture by a 50 μm multimode fibre. Only 40% of the light coupled into the spectrometer can normally be measured from the multimode fibre. The SPAD itself has an efficiency of ~25% at 950 nm, so altogether a TRPL measurement will have an efficiency of only ~10%. For this reason, when measuring TRPL in low light levels often the wavelength tunable filter (section 2.3.1) was used instead of the spectrometer for spectral filtering. In the alternative setup, the microscope collection arm single mode fibre is coupled into the wavelength tunable filter and collected by a 50 μm multimode fibre with an efficiency of ~58% [7], giving an overall efficiency (including detection by the SPAD) of ~15%.

2.5 Triggering electronics

At several points in this work separate pieces of equipment had to be synchronised so that optical excitation pulses, GHz bandwidth voltage pulses and TCSPC measurements could occur at the desired times. The timing measurements are in all cases made by SPADs, which are designed to output TTL-like pulses whenever they detect a photon. These TTL-like pulses provide accurate start and/or stop signals to a TCC900 electronic timing card. The timing card then registers a single count for each completed start-stop cycle. In order to build up reliable information from multiple counting events at repetition rates of several kHz to several hundred MHz it was necessary to control the overall timing jitter of the system to $\ll 1$ ns. This was achieved using several master-slave triggering systems.

2.5.1 TRPL using a static voltage bias applied across the sample

For standard TRPL scans with a static voltage bias applied to the sample the pulsed PicoQuant laser controller (PDL800-B) has its own internal timing system which can be used to provide the trigger pulse to the start input of the TCC900 timing card. The stop pulse was provided by the SPAD when a photon was detected. The electronic pulse from the SPAD was passed through an inline 20 dB attenuator and then an Avtech electro systems AVX-2 inline inverter, in order that the pulse was a suitable voltage and polarity for triggering a detection in the timing card.

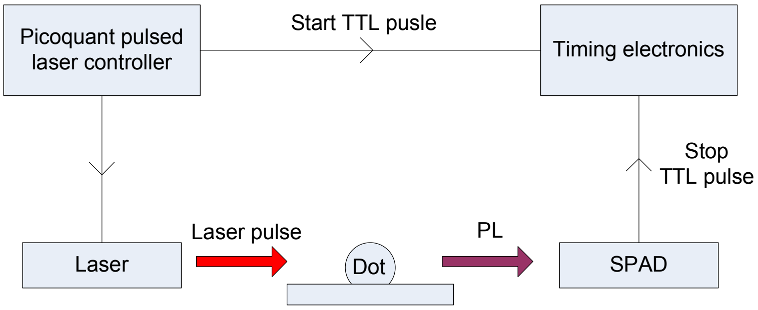

Figure 2.11: The timing setup for standard TRPL.

2.5.2 TRPL using GHz bandwidth voltage pulses applied across the sample

For TRPL in which the dot is subject to a time-varying voltage bias, the Agilent 81133A pulse pattern generator (PPG) provides the bias, and also serves as the master to the triggering system. The PPG provides a trigger to the PicoQuant laser controller (whether or not the pulsed laser is being used), and the laser controller then triggers the start input of the TCC900 card. As in the case of standard TRPL, the stop input pulse is provided by the SPAD when a photon is detected.

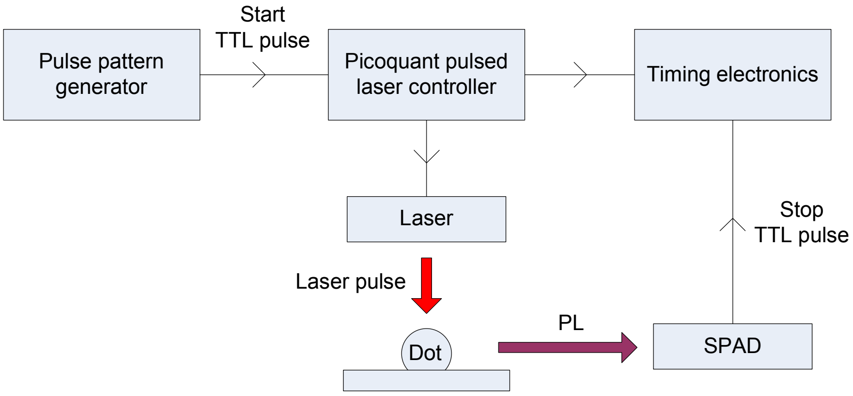

Figure 2.12: The timing setup for TRPL when GHz bandwidth voltage pulses are used. The Picoquant controller is triggered by the PPG.

2.5.3 Timing for autocorrelation

In this case (Fig. 2.13), both the start and stop inputs of the timing electronics are triggered by TTL-like pulses from the SPADs of the HBT, inverted and attenuated as previously. Separately, the PPG triggers the PicoQuant pulsed laser controller (if a pulsed laser is used) so that the delay between voltage pulses and laser pulses can be altered accurately (in the same fashion as Fig. 2.12).

2.5.4 The timing card

The T900 card can be used in either of two modes, forward mode, or reverse mode. In forward mode the basic function of the card starts the charging of a capacitor on the arrival of a START pulse, and stops it on the arrival of a STOP pulse. The charge accumulation on the capacitor can then be converted to a time, and a single count is registered at that time. In this way timing events are recorded in a histogram. In reverse mode, the STOP pulse starts the charging of the capacitor, and the START pulse stops charging.

There are advantages to both modes. Ideally, the mode used should encourage the largest number of completed measurements. For instance, for general use the input with the smaller number of counts should be used to start the capacitor charging, with the rationale that the larger count input is more likely to stop the capacitor and register a count. However, for use with autocorrelations counts are likely to be

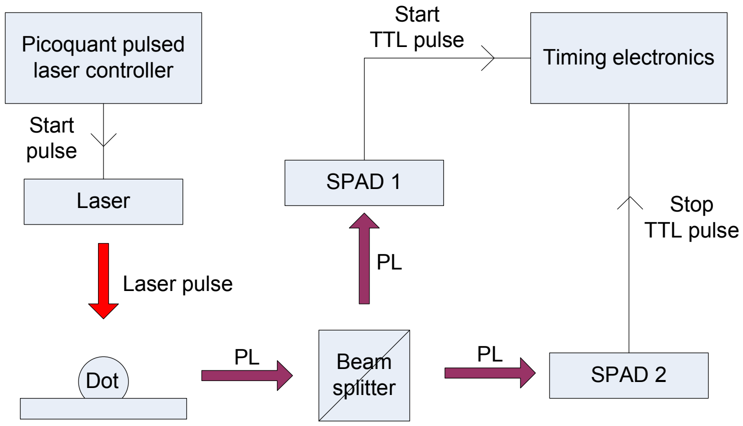

Figure 2.13: The timing setup for Autocorrelation measurements. When fast voltage pulses are used the Picoquant controller is triggered by the PPG.

similar for both inputs, and with TRPL the repetition period is almost always the same as the measurement time window, so by using forward mode it is ensuring that the capacitor is constantly charging. Therefore forward mode was always used for these experiments.

2.6 Wafer material

There were two wafer types used for creation of bias controlled devices. These were sourced from UCSB Santa Barbara from Professor Pierre Petroff. In order to create the completed charge-tunable device a semi-transparent NiCr Schottky gate was evaporated onto the top surface of the wafer, and a Ohmic contact to the back contact was created (details are given in Chapter 4).

2.6.1 Wafer A (10311A–Thick capping layer)

Material	Thickness	Description
GaAs	6.3 nm	
AlAs/GaAs	24x(3.0 nm/2.0 nm)	superlattice
GaAs	30.0 nm	capping layer
InAs	1.0 nm	quantum dots
GaAs	25.0 nm	tunneling barrier
n+ GaAs	20.0 nm	n-doped GaAs back contact $n = 4 * 10^{18}\text{cm}^{-3}$
GaAs	80.0 nm	
GaAs	40x(2.0 nm/2.0 nm)	
GaAs		Substrate

This was the original wafer material as used in previous experiments [1, 9]. The capping layer over the dots is 30 nm thick.

2.6.2 Wafer B (050328B–Thin capping layer)

Material	**Thickness**	**Description**
GaAs	6.3 nm	
AlAs/GaAs	24x(3.0 nm/2.0 nm)	superlattice
GaAs	10.0 nm	capping layer
InAs	1.0 nm	quantum dots
GaAs	25.0 nm	tunneling barrier
n+ GaAs	20.0 nm	n-doped GaAs back contact $n = 4 * 10^{18}\text{cm}^{-3}$
GaAs	80.0 nm	
GaAs	40x(2.0 nm/2.0 nm)	
GaAs		Substrate

This wafer was grown in response to the results in Chapter 3 section 3.3.3, as it was shown that Wafer A was largely unsuitable for the GHz bandwidth voltage manipulation experiments in Chapter 5. The capping layer in this new wafer is 10 nm thick. The rest of the structure remains the same as for Wafer A.

2.7 Microscope and Wiring

The idea behind the confocal setup was to allow single quantum dot excitation with the ability to perform optical alignment in situ. For this reason, only one arm of the microscope, the objective arm, was cooled. The rest remains out of the helium dewar so that alignment can be done by hand. The objective arm is long (~1.2 m) so that the sample is maintained below the liquid helium level for as long as possible while in the helium dewar. The objective lens was chosen to be aspheric in order to achieve diffraction-limited performance on the objective arm axis, and because temperature contractions have a smaller effect on an aspheric lens than on a compound lens. The objective arm (including the sample, nanopositioners, and cabling) is encased in a hollow stainless steel tube which is evacuated down to 10^{-5} mbar in order to prevent condensation. The tube is then filled with ~25 mbar of helium gas in order to allow efficient cooling. The whole objective arm can then be cooled in liquid helium to 4.2 K, as in Fig. 2.14. At low temperature, alignment is achieved by adjusting the microscope head and nanopositioners, using the dot PL intensity as a guide.

2.7.1 Original voltage cabling

The original cabling for the d.c voltage experiments was in the form of brass twisted pairs. The wires were twisted to prevent any adverse magnetic fields affecting the

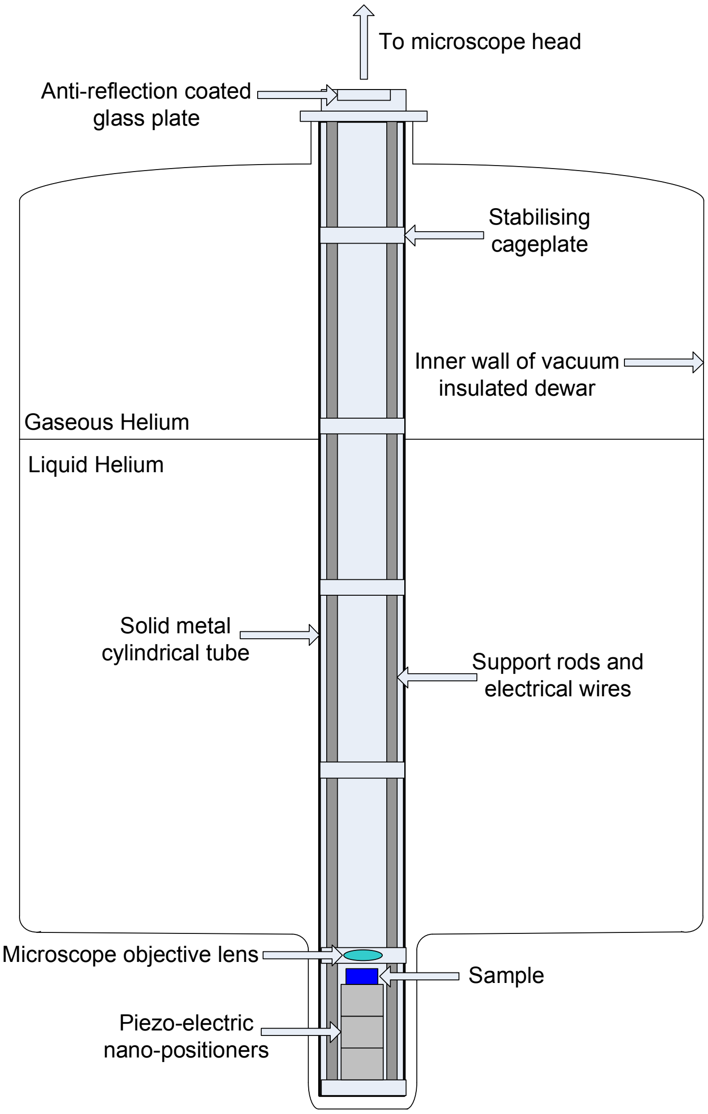

Figure 2.14: Schematic of the objective arm of the microscope inside the dewar. The objective, sample and nanopositioners are located at the bottom of the dewar. The microscope head (shown in Fig. 2.2) sits directly above this setup.

device. The approximate liquid helium boil-off rate of the setup was 2-3 litres per day.

2.7.2 Fast voltage cabling

The original voltage cabling exhibited a large signal attenuation at high frequencies. In order that the voltage experienced by a dot could be altered with a GHz bandwidth signal, the cabling must first be capable of allowing a GHz bandwidth signal to propagate to the device. The microscope cabling was replaced for the GHz bandwidth voltage experiments in Chapter 5 in order to ensure that a voltage applied by the PPG could reach the sample with $\ll$1 ns rise/fall time. The new cabling[2] was in the form of 50 Ω impedance brass coaxial cabling with SMA connectors (as used in [10]). Using this cabling the average helium boil-off was 3-4 litres per day, suggesting that the new cabling was responsible for an additional evaporation of ~1 litre per day. The 10-90% voltage switching time of the cabling connected to the PPG was measured to be 150 ps at room temperature (Fig. 2.15). This cabling was used for all experiments that have a quickly time-varying voltage.

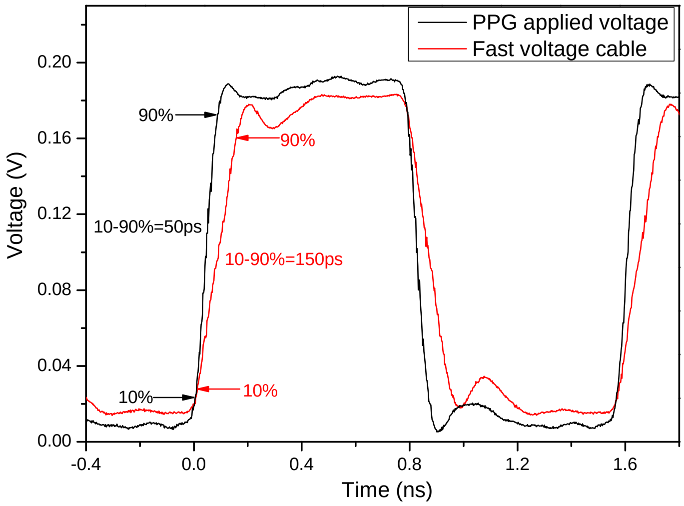

Figure 2.15: 10-90% rise-time measurements for the PPG (black line), and the cabling connected to the PPG (red line) as measured by an Agilent 86100C fast oscilloscope. The PPG has been set to output a 640 MHz repetition rate square wave voltage with a 180 mV peak-peak amplitude.

---

[2] obtained from Dr Robert Hadfield, Heriot-Watt University

2.7.3 Connection to the sample

The microscope cabling was connected to the sample via an intermediate flexible brass 50 Ω impedance coaxial cable[3] made by Axon. The cable connected to the microscope cabling using an SMA connector. The outer and inner of the flexible cable were connected to the device Ohmic contact and Schottky gate respectively, using high conductance silver paint purchased from RS. This cable was also glued to the sample mount in order to provide strain relief in the system (see Fig. 2.17). In this way the sample could be moved in three dimensions using piezo-electric nano-positioners (from Attocube) with respect to the objective lens whilst maintaining a solid connection between the device and the cabling, allowing ns-rise time voltage pulses to propagate to the sample from the PPG.

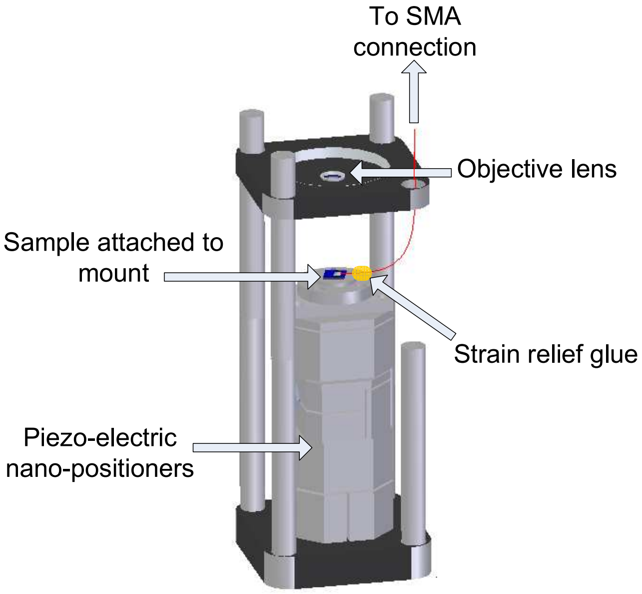

Figure 2.16: Schematic of the sample and motor assembly with SMA cabling.

2.8 Solid Immersion Lenses

Increasing the NA over which light can be collected will increase the collection efficiency of the dot PL. In the original setup a 2 mm diameter hemispherical solid immersion lens (SIL, $n = 2.15$) was used. An investigation was performed to measure the potential suitability of using a 1.8 mm diameter Weierstrass (S-SIL, $n = 2.15$). Shown in Fig. 2.18 is the setup used to measure the resolution of both SILs. A 2 μm period checkerboard pattern of reflective chrome on glass was used in place of the sample in this arrangement in order to function as a measurement standard. On top of the checkerboard was placed either a SIL or an S-SIL. A calibrated iris was added

---

[3] obtained from Stephan Manus, LMU

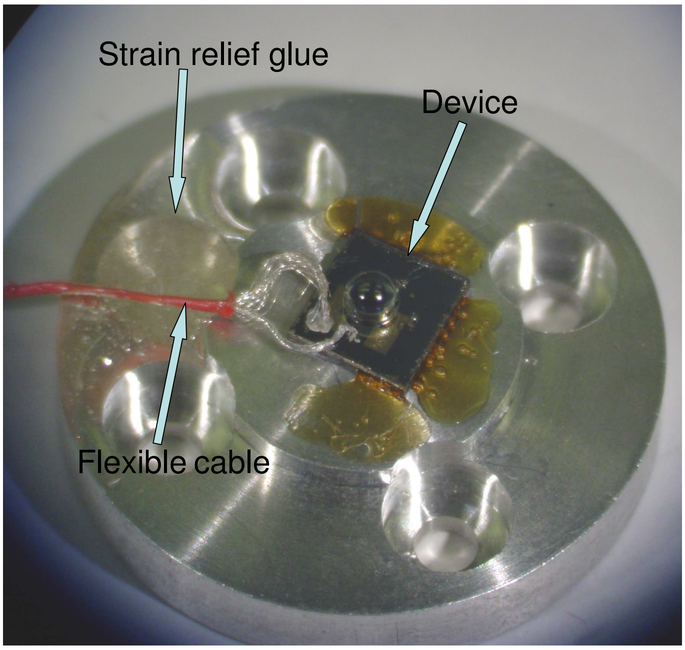

Figure 2.17: A sample with the electrical connections going through a strain relief section on the sample holder.

before the objective lens (a 0.55 NA Mitutoyo achromatic lens) in order to restrict manually the effective NA. The checkerboard was illuminated by a 950 nm continuous wave diode laser which was coupled into a 2x2 single mode fibre splitter (99:1 ratio, from FONT Canada), with 1% of the laser power being coupled into the microscope collection arm. The light reflected by the checkerboard was coupled back into the fibre splitter from the microscope collection arm and 99% of the reflected power was measured by a Si p-i-n detector (Thorlabs DET110). This method was employed in order to simplify the task of alignment by only using one arm of the microscope head.

A voltage source provided as part of an EG & G Instruments 7265 lock-in amplifier was used to provide the X-axis piezoelectric nano-positioner with a slow ramping d.c. voltage (0-10 V) with a superimposed sinusoidal (a.c.) oscillation (130 Hz, 10 mV). The same lock-in was then used as an analogue-to-digital-converter to measure the current amplitude from the Si detector, and the oscillation was used as a reference signal in order to determine the in-phase (real) and 90° out-of-phase (imaginary) components of the current amplitude (Referred to as I_R and I_I respectively).

Shown in Fig. 2.19 are I_R and I_I against the voltage applied to the piezo-electric nano-positioner. The measurements provide an image of the checkerboard as the laser scanned across the metal/glass interface (the d.c. signal, I_R), as well as a measurement of how the real signal changes (the a.c. signal, $I_I = \frac{dI_R}{dV_{d.c.}}$). The d.c. signal can be used as a local measurement standard by identifying a 1 μm checkerboard feature (Fig. 2.19), giving an indication of the distance moved with increasing voltage. The a.c. signal has a Gaussian shape, which is caused by the intensity profile of the laser spot.

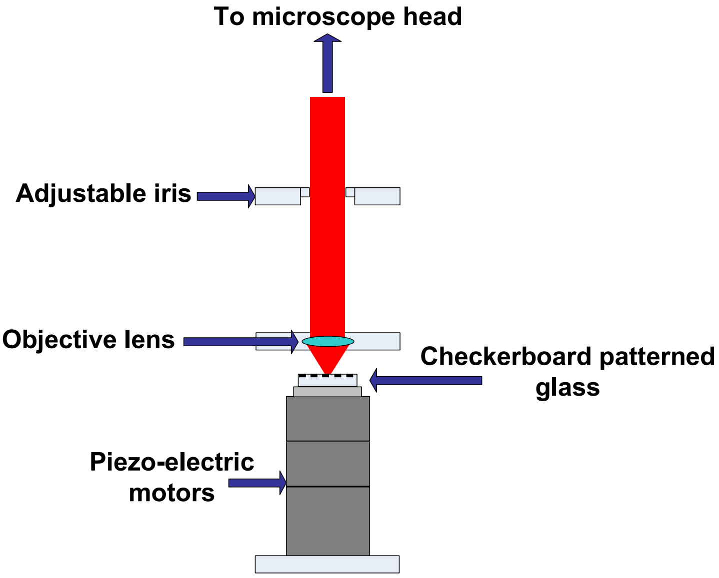

Figure 2.18: Diagram of the setup used to measure the microscope resolution. A chrome checkerboard patterned piece of glass was used as the sample and an adjustable iris was used to vary the NA.

The FWHM of the closest fit Gaussian profile can be considered the spot size.

From the a.c signal data in Fig. 2.19 it is possible make a comparison between the different numerical aperture increasing lenses (NAILs) in Fig. 2.20. As can be seen the spot size of the S-SIL is measured at 275 nm ±13 nm ($\frac{\lambda}{3.5}$), the hemispherical SIL shows a spot size of 540 nm ±10 nm ($\frac{\lambda}{1.8}$), and without a SIL the spot size is 950 nm ±10 nm ($\frac{\lambda}{1}$). This shows that there is a resolution advantage to using a S-SIL. The use of a NAIL here is not valued simply as a resolution increasing device, but instead as a means of increasing collection efficiency [11, 12, 13, 14, 15]. In this case an increased optical collection efficiency is enabled by a larger effective NA, which also increases the resolution of the system.

Resolution tests were performed with the S-SIL as the iris was used to restrict the effective NA of the objective lens (Fig. 2.21). There is no further decrease in spot size beyond approximately 0.4 NA, therefore any objective used should have at least this NA value to gain the full benefit of the S-SIL. Note that this value is considerably lower than the theoretical 0.47 NA value for the S-SIL, calculated using the largest angle of refraction possible for a dot placed centrally underneath the S-SIL. This is because very high angle rays are hard to control, and depend sensitively on the quality of manufacture of the S-SIL.

The lenses of the microscope were changed to accommodate the S-SIL. Beyond the NA, it was also important that the objective lens allows a large enough clearance between it and the sample to house the S-SIL. A 0.40 NA aspheric lens (Thorlabs C110TME-B, with a clear aperture of 7.2 mm diameter) with an anti-reflection coating

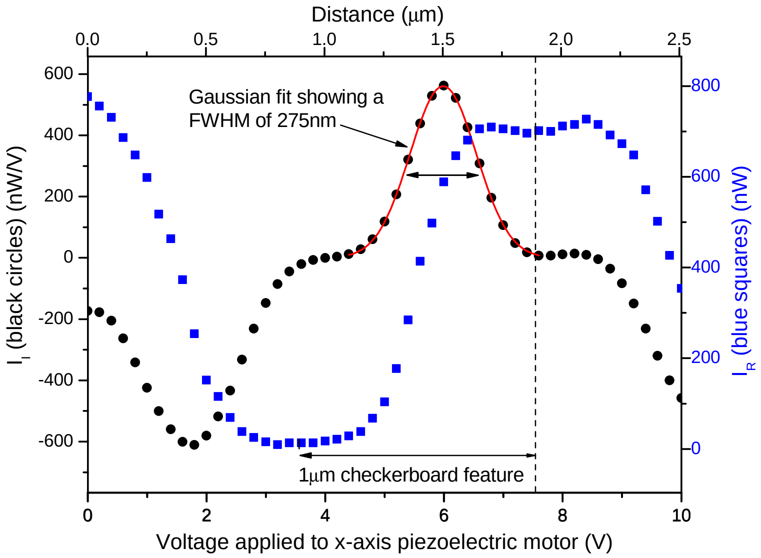

Figure 2.19: I_R (blue squares) and I_I (black circles) as the motor position is changed using the d.c. voltage, performed at room temperature. A 950 nm CW laser is illuminating a 2 μm period checkerboard, on top of which is placed a S-SIL. A Gaussian fit is included (red line) with a FWHM of 275 nm.

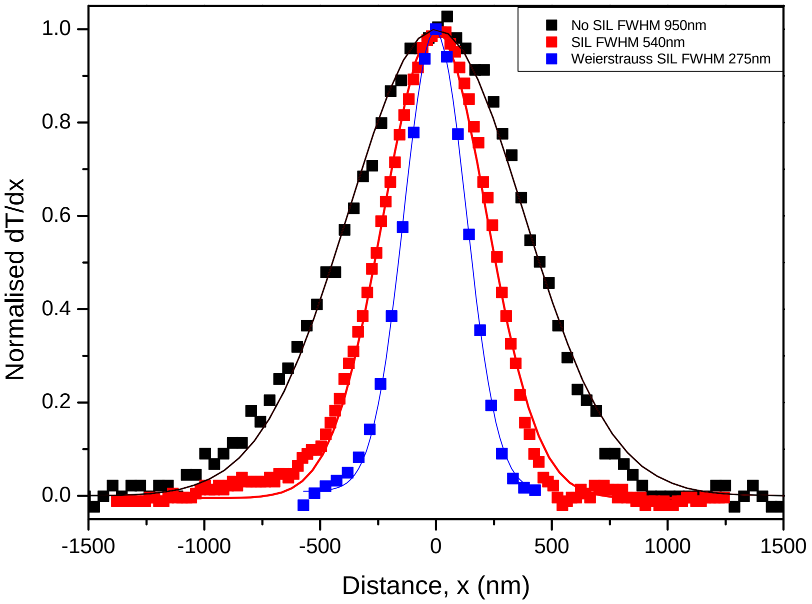

Figure 2.20: Comparison of fitted Gaussian curves for SIL S-SIL and no-SIL experiments using 950 nm CW laser light. The No-SIL data were taken by Paul Dalgarno.

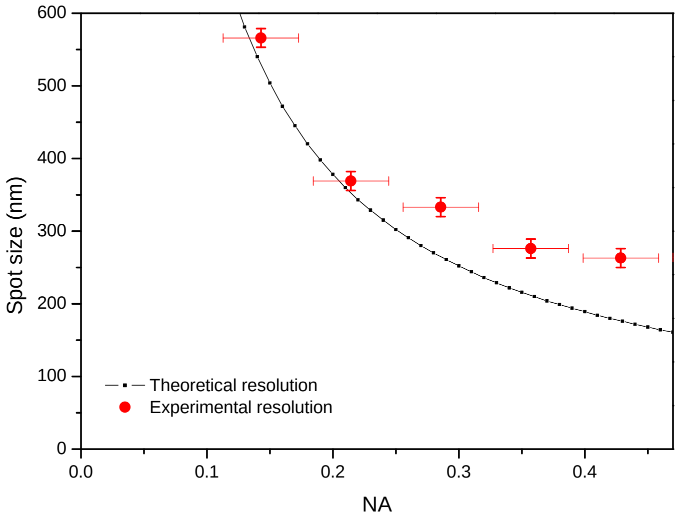

Figure 2.21: Comparison of the S-SIL FWHM spot size against NA, for a 2 μm period checkerboard illuminated with 950 nm laser light as in Fig. 2.18. Here, the calibrated iris was used to restrict the NA of the objective lens. The maximum NA achievable by the objective lens is 0.55 NA. The maximum NA achievable by the S-SIL is 0.47 NA. The theoretical resolution is calculated using Sparrow's criterion ($\Delta x = \frac{0.52\lambda}{NA}$)

for the near infra-red (NIR) was chosen for the objective lens, and a 0.15 NA aspheric lens (Thorlabs C280TM-B, with a NIR anti-reflection coating and a clear aperture of 6.5 mm diameter) was used to couple the light to and from the excitation and collection single mode fibres. The pair of lenses give an effective NA of 0.37 for the objective lens. When a S-SIL is included in the system, the overall effective NA (NA_{eff}) of PL collection from the dot becomes [16]

$$NA_{eff} = \frac{NA_{obj} n_{SIL}^2}{n_s} = 0.49, \tag{2.4}$$

where NA_{obj} is the NA of the objective lens (=0.37), n_{SIL} is the refractive index of the S-SIL (=2.15), and n_{GaAs} is the refractive index of the GaAs (=3.5). This then gives an optical collection efficiency (ξ) of

$$\xi = \frac{1}{2}\left\{1 - \left[1 - NA_{eff}^2\right]^{\frac{1}{2}}\right\}, \tag{2.5}$$

which gives a value of 6.4%. If a normal SIL is used $n_{SIL}^2 \rightarrow n_{SIL}$ in Eqn. 2.4, and (for the same lenses) the collection efficiency becomes 1.3%. This compares to the value of 0.74% calculated in Chapter 1 section 1.4.5 for a system without any SIL.

2.9 Conclusion

Several improvements were made over the original microscope system, implemented in order that a variety of single quantum dot experiments can be performed at low (helium) temperature. Polarisation optics have been added to the confocal microscope, so that polarisation-based efficient optical excitation and filtering can be performed. Close to diffraction-limited operation has been shown with the use of a S-SIL, and the microscope objective lens was changed to accommodate its use. Finally, high frequency electronic cabling was added to the microscope, allowing the opportunity to apply GHz bandwidth voltage pulses to a charge-tunable device.

References

[1] J. M. Smith, P. A. Dalgarno, R. J. Warburton, A. O. Govorov, K. Karrai, B. D. Gerardot and P. M. Petroff, *Voltage control of the spin dynamics of an exciton in semiconductor quantum dot.* Physical Review Letters, **94**, 197402 (2005).

[2] T.R Corle, G. S. Kino, *Confocal Scanning Optical Microscopy and Related Imaging Systems.* Academic Press, San Diego, 1996.

[3] S. Cortez, O. Krebs, S. Laurent, M. Senes, X. Marie, P. Voisin, R. Ferreira, G. Bastard, J.M. Gerard, and T. Amand, *Optically driven spin memory in n-doped InAs-GaAs quantum dots.* Physical Review Letters, **89**, 207401 (2002).

[4] R. Hanson and D.D. Awschalom, *Coherent manipulation of single spins in semiconductors.* Nature, **453**, 1043 (2008).

[5] M. Kroutvar, Y. Ducommun, D. Heiss, M. Bichler, D. Schuh, G. Abstreiter, and J.J. Finley, *Optically programmable electron spin memory using semiconductor quantum dots.* Nature, **432**, 81 (2004).

[6] R.J. Young, S.J. Dewhurst, R.M. Stevenson, P. Atkinson, A.J. Bennett, M.B. Ward, K. Cooper, D.A. Ritchie, and A.J. Shields, *Single electron-spin memory with a semiconductor quantum dot.* New Journal of Physics, **9**, 365 (2007).

[7] D. Brunner, *Laser spectroscopy of single quantum dots.* Final year project report, Heriot-Watt University, 2006.

[8] P. A. Dalgarno, Thesis title: *Time correlated single photon counting on charge tunable quantum dots.* (2005).

[9] M. Ediger, P. A. Dalgarno, J. M. Smith, B. D. Gerardot, R. J. Warburton, K. Karrai and P. M. Petroff, *Controlled generation of neutral, negatively-charged and positively-charged excitons in the same single quantum dot.* Applied Physics Letters, **86**, 211909 (2005).

[10] R. H. Hadfield, P. A. Dalgarno, J. A. O'Connor, E. Ramsey, R. J. Warburton, E. J. Gansen, B. Baek, M. J. Stevens, R. P. Mirin and S. W. Nam, *Submicrometer photoresponse mapping of nanowire superconducting single-photon detectors.* Applied Physics Letters, **91**, 241108 (2007).

[11] B. Bennett, S. Goldberg, B. Ippolito, L. Novotny, Z.H. Liu, and M.S. Unlu, *Immersion lens microscopy of photonic nanostructures and quantum dots.* IEEE Journal of Selected Topics in Quantum Electronics, **8**, 1051 (2002).

[12] K. Karrai, X. Lorenz, and L. Novotny, *Enhanced reflectivity contrast in confocal solid immersion lens microscopy.* Applied Physics Letters, **21**, 3459 (2000).

[13] S. Moehl, H. Zhao, B.D. Don, S. Wachter, and H. Kalt, *Solid immersion lens-enhanced nano-photoluminescence: Principle and applications.* Journal of Applied Physics, **93**, 6265 (2003).

[14] S. Weiss, *Fluorescence spectroscopy of single biomolecules.* Science, **283**, 1676 (1999).

[15] V. Zwiller and G. Bjork, *Improved light extraction from emitters in high refractive index materials using solid immersion lenses.* Journal of Applied Physics, **92**, 660 (2002).

[16] K. A. Serrels, E. Ramsey, P. A. Dalgarno, B. D. Gerardot, J. A. O'Conner, R. H. Hadfield, R. J. Warburton and D. T. Reid, *Solid immersion lens applications for nanophotonic devices.* Journal of Nanophotonics, **2**, 021854 (2008).

Chapter 3

Application of a static voltage to a single quantum dot

In order that GHz bandwidth voltage pulses could be successfully applied across a charge-tunable structure it was necessary first to characterise some of the main dot properties using a d.c. voltage. Neutral and charged excitons were identified in a single dot as the charge-tunable device was biased with a d.c. voltage. Power dependent measurements show that the device structure allows holes to be trapped in the capping layer. Lifetime measurements reveal electron and hole tunneling effects. Altering the wafer structure allows the suppression of hole tunneling, which is more suitable for future hole storage experiments. Furthermore, intensity autocorrelation measurements point to hole trapping in the dot wetting layer, and the sample dimensions can be used to alter the rate of hole recapture into the dot. Finally, a region was identified at the low bias edge of X^0 which allows a novel approach to resonant excitation and PL collection from a single dot.

3.1 The charge-tunable device

The charge-tunable devices used allow a voltage to be applied between the top NiCr Schottky gate and the n-doped back contact without any direct current flow. In this way the conduction and valence bands of the wafer can be manipulated as a lever arm, using an applied voltage. GHz voltage bias changes will alter the slope of the lever arm at a rate comparable to a dot exciton radiative recombination. In order to understand the effect of GHz bandwidth voltage pulsing it was necessary first to understand the behaviour of a dot in the structure as the lever arm is set to different positions using a d.c. voltage bias.

3.1.1 The lever arm model

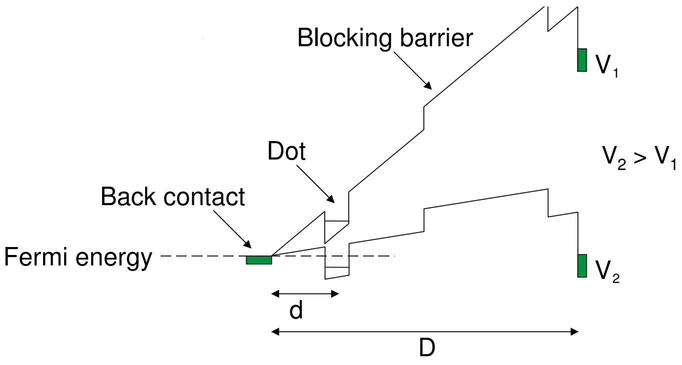

Figure 3.1: Diagram of the wafer conduction band for two applied d.c voltage biases. Shown are the Fermi level ($E = 0$) for the system (defined by the n-doped back contact), the dot and the blocking barrier. As the voltage is increased the dot energy level lowers with respect to the Fermi level.

A voltage applied between the Schottky gate and the back contact causes an energy gradient along the structure with respect to the Fermi level, set by the back contact [1]. As a voltage (V_{app}) is applied, the voltage experienced by the dot (V_{exp}) is

$$V_{exp} = \frac{V_{app} - V_0}{\lambda}, \tag{3.1}$$

where $\lambda = \frac{D}{d}$ is defined as the lever arm ratio of the structure width (D) to the distance between the dots and the back contact (d) (See Fig. 3.1). V_0 is a constant offset due to the Schottky barrier height, equal to 0.62 V for these devices [1, 2]. For Wafer A (B) the lever arm ratio is 7:1 (6.2:1).

As the voltage is raised the lever arm is lowered (Fig. 3.1), and the energy levels of the dot will lower compared with the Fermi energy. As a conduction energy level in the dot becomes degenerate with the Fermi level, electrons will tunnel between the back contact and the dot. When the same conduction energy level becomes lower than the Fermi level, electron tunneling from the dot to the back contact is suppressed.

In this way electron charging is possible using an applied d.c. voltage, and this will occur on a ps timescale [3].

In order for additional electrons to tunnel into the dot, each electron must first overcome the Coulomb repulsion from the electrons that are already in the dot. This results in distinct bias voltage extents in which only a certain number of electrons can occupy the dot. This is referred to as the Coulomb Blockade [4], and this is useful as it allows complete voltage-enabled control over the number of electrons (the majority carrier) in the dot [5].

3.1.2 Dot charge against gate bias

Optical excitation of the dot provides the minority carrier, the hole. Control over the number of holes available to the dot is therefore possible by altering the excitation power. In much of this work, non-resonant optical excitation at ∼830 nm is used to excite electron-hole pairs into the wetting layer. The electrons relax into the back contact, and depending on the excitation power, one or more holes will relax into the dot. As discussed in Chapter 1, holes relax into the lowest dot energy level available, and do so at a fast pace relative to recombination timescales. Depending on the voltage, one or more electrons may tunnel into the dot, forming an exciton. If the dot contains at least one electron hole pair, recombination will occur on a ns timescale (see section 3.3).

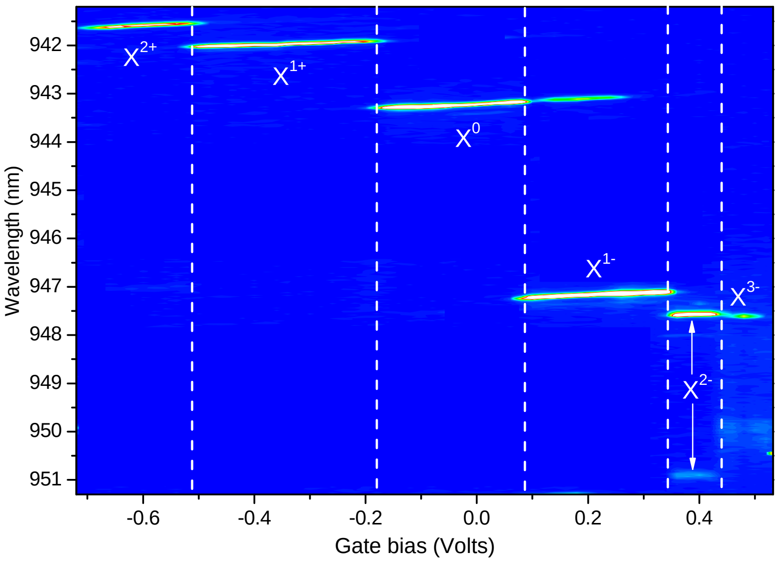

Figure 3.2: Contour plot showing the PL against gate bias recorded from a single dot in Wafer B (050328B) excited with 100 ps pulses of 826 nm laser light with a repetition rate of 10 MHz and an average power of 6.6 nW μm^{-2} at the sample surface. Blue $\simeq$90 counts, green $\simeq$150 counts, yellow $\simeq$200 counts, red $\simeq$270 counts, white = 400 counts or more.

In order to characterise the field dependence of electron charging in the charge tunable structure several dots from each wafer were excited with non-resonant laser light, and the PL was recorded as a function of gate bias. Fig. 3.2 shows PL from a dot in Wafer B excited with 826 nm pulsed laser light at an average power of 6.6 nW μm^{-2}. The distinct PL voltage extents indicate electron charging between different exciton configurations. Easiest to identify is the 5.6 meV redshift between two PL lines at 0.09 V which is indicative of the difference in energy between electron-electron and electron-hole Coulomb energies (E_{ee}^{ss} and E_{eh}^{ss}), confirming electron charging between the neutral exciton (X^0, 1 electron 1 hole) and the negatively charged exciton or negative trion (X^{1-}, 2 electrons 1 hole) [6]. Further to this, TRPL of X^0 and X^{1-} show differences in recombination lifetime behaviour due to the X^0 fine structure (as discussed in 3.3) [3]. Increasing the gate voltage induces further electron tunneling to X^{2-} (3 electrons 1 hole) at 0.35 V and X^{3-} (4 electrons 1 hole) at 0.45 V [6]. The X^{2-} singlet state emission is also visible at 950.8 nm, further confirming this identification [6]. On the low bias side of X^0, any one-hole excitons are ionised at biases lower than -0.18 V, leaving a single hole. The PL observed at 942 nm is therefore from the positively charged exciton (X^{1+}, 1 electrons 2 holes) which is favoured by the Coulomb blockade at this voltage [7]. Using the same argument, at biases lower than -0.52 V all one- and two-hole excitons will be completely ionised due the voltage, so the PL observed at 941.6 nm is due to X^{2+} (1 electrons 3 holes).

3.1.3 The Coulomb model

The Coulomb model [1, 2, 7] can be fitted to the charging diagram in Fig. 3.2, allowing an understanding of electron charging in terms of the absolute energies of any charge configuration in the dot. At $T = 4$ K the dot will undergo fast electron tunneling in order to achieve the lowest energy charge configuration available. The Stark shift is not included in the model. Fig. 3.3 shows the energy of several zero- and one-hole charge configurations in the dot from Fig. 3.2 as the d.c. voltage bias is altered. The zero-hole configurations shown include the empty hole energy ($|0\rangle = 0$ meV), the single electron energy ($E(e)$), and the two s-shell electron energy ($E(2e)$), given (in meV) by

$$E(e) = (V_0 - V_g)\lambda^{-1} - E_c - E_i, \tag{3.2}$$

and

$$E(2e) = (V_0 - V_g)\lambda^{-1} - 2E_c + E_{ee}^{ss} - 4E_i, \tag{3.3}$$

where V_0, V_g and λ are defined in section 3.1, E_c is the ionisation energy of an electron in the s-shell, E_{ee}^{ss} is defined in section 3.1.2, and E_i is the image charge energy for an electron in the dot (=1.1 meV [2]), which takes into account the change in energy at the dot due to the redistribution of charge in the back contact when an electron tunnels into the dot. The one-hole configurations shown include the hole-only energy ($E(h)$), the neutral exciton energy ($E(X^0)$), and the negative trion energy ($E(X^{1-})$), given (in meV) by

$$E(h) = E_0 - (V_0 - V_g)\lambda^{-1} + E_c + E_i, \tag{3.4}$$

$$E(X^0) = E_0 - E_{eh}^{ss}, \tag{3.5}$$

and

$$E(X^{1-}) = E_0 + (V_0 - V_g)\lambda^{-1} - E_c - 2E_{eh}^{ss} + E_{ee}^{ss} - E_i, \tag{3.6}$$

where E_0 is the s-shell valence band to s-shell conduction band energy difference with no carriers in the dot, and E_{eh}^{ss} is defined in section 3.1.2.

Without optical excitation there are no holes, and only the zero-hole charge configurations will be achievable. As the voltage is increased greater than V$_C$ a single electron will tunnel into the dot. The Coulomb blockade prevents more than one electron existing in the dot for any significant time at $T = 4$ K. As the bias is increased beyond V$_D$ a second electron can overcome the Coulomb repulsion from the first, and tunnel into the dot.

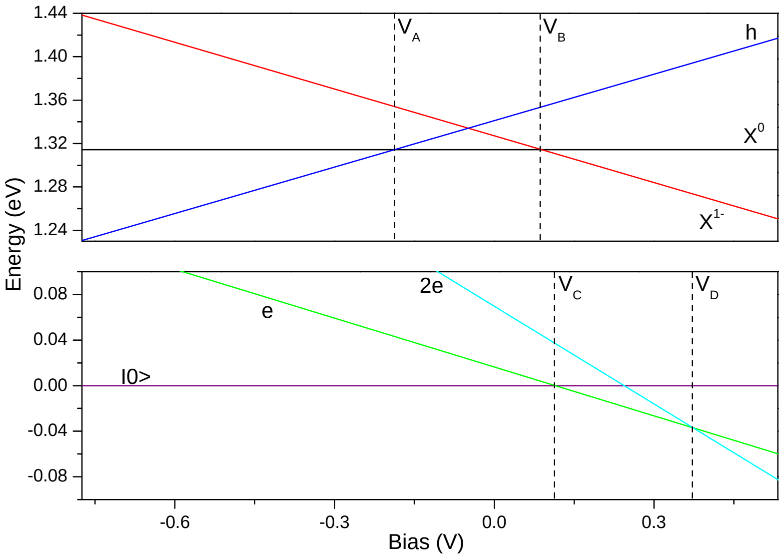

Figure 3.3: Energy level diagram showing the energies of $|0\rangle$ (Pink), h (Blue), e (Green), 2e (Cyan), X^0 (Black) and X^{1-} (Red) against voltage bias for the dot in Fig. 3.2. The fitting values (defined in [1, 2, 7] and later in this chapter as appropriate) are $\Delta V_g = -0.239$ V, $\lambda = 7$, $V_0 = 0.62$ V, $E_0 = 1.34$ eV, $E_c = 114$ meV, $E_i = -1.1$ meV, $E_{ee}^{ss} = 17.8$ meV and $E_{eh}^{ss} = 23.4$ meV.

If the device is optically excited, single hole charge configurations will be allowed to form within the dot. At biases lower than V$_A$, a single hole is stored within the dot. When the bias is larger than V_A an electron will tunnel into the dot forming X^0, which will then decay into $|0\rangle$ if the electron-hole pair recombines. At biases larger than V_B a second electron will overcome the Coulomb blockade and tunnel into the dot, forming X^{1-}. If the electron-hole pair is allowed to recombine, the X^{1-} will decay into a single electron (e). The presence of a hole in the dot lowers the conduction energy levels in the dot with respect to the Fermi level, and as such the $X^0 \rightarrow X^{1-}$ transition occurs at a lower gate voltage than the $|0\rangle \rightarrow$ e transition [8, 9].

Using the Coulomb model, it is possible to deduce other terms not instantly obvious from the charging plot, such as the electron-electron and electron-hole Coulomb energies (E^{ss}_{ee} and E^{ss}_{eh}). Furthermore, the model shows a potentially useful 25mV bias-region between V_B and V_C in which the lowest energy one-hole exciton is the X^{1-} and the lowest energy zero-hole state is $|0\rangle$, which is used successfully in section 3.5 to perform a resonant absorption experiment. Lastly, knowledge of how the Coulomb model applies to a dot in the charge tunable structure is crucial to understanding the behaviour of the dot during GHz bandwidth voltage pulsing.

3.2 Hole trapping at the capping layer

The bias points at which electron charging occurs experience a power-dependent voltage offset which must be taken into account when using GHz bandwidth voltage pulsing. When optically exciting a quantum dot with a non-resonant laser, altering the excitation power from the laser causes a shift of the bias points at which single electron charging occurs [10]. The shift is shown here to be due to photogenerated holes accumulating in the capping layer-superlattice interface region of the charge-tunable structure, and the effect is characterised by taking PL for the same dot for a large range of non-resonant optical excitation powers.

Shown in Fig. 3.4 are the PL against gate bias for the same dot as in Fig. 3.2, at two different excitation powers. The contour taken at larger power (Fig. 3.4(b)) shows a shift towards higher reverse bias, with respect to the lower power (Fig. 3.4(a)). This effect was observed over the entire range of powers measured. The voltage extents of the PL lines associated with each exciton are not affected by any power changes, but the intensity of each PL line becomes larger with increasing power. At higher power (Fig. 3.4(b)) it is possible to observe PL from higher energy excitons forming in the dot. The biexciton ($2X^0$), which consists two s-shell electrons and two s-shell holes can be identified because it cascades into X^0, and also because it emits PL at an energy between that of X^0 and X^{1-} and ionises at lower bias voltages to become X^{1+} [7]. Also from Ref. [7], and because only a single dot is optically excited, it is possible to label the hot biexciton ($2X^0_h$) which consists of two s-shell electrons, one s-shell hole and one p-shell hole. Lastly, $2X^0_h$ ionises at lower voltage biases to become the hot positive trion (X^{1+}_h), consisting of one s-shell electron, one s-shell hole and one p-shell hole.

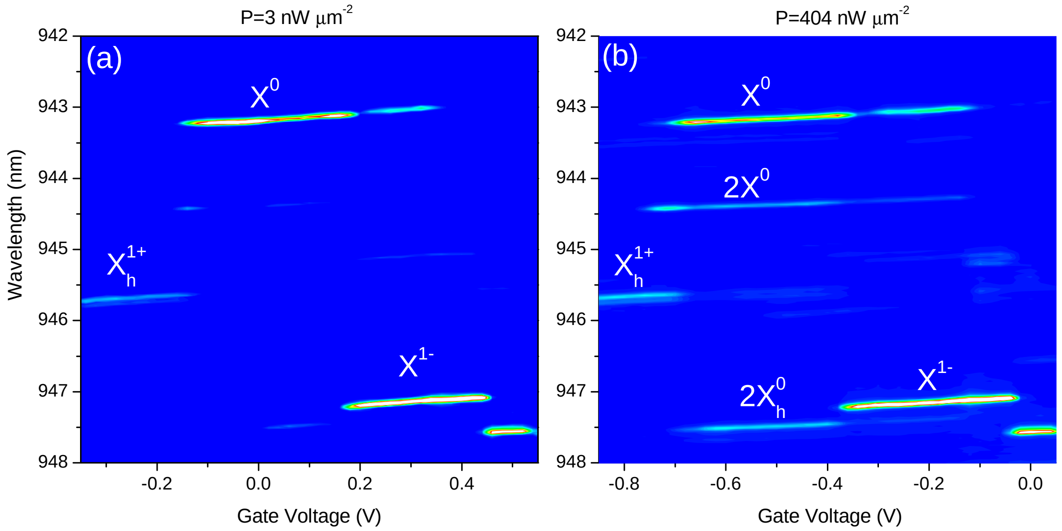

Figure 3.4: PL recorded from the same dot as in Fig. 3.2. The dot is excited with (a) 3 nW μm^{-2} and (b) 404 nW μm^{-2} of CW 830 nm non-resonant laser light. In (a), Blue $\simeq$90 counts, green $\simeq$150 counts, yellow $\simeq$200 counts, red $\simeq$250 counts, white = 300 counts or more. In (b), Blue $\simeq$80 counts, green $\simeq$800 counts, yellow $\simeq$1300 counts, red $\simeq$1800 counts, white = 2000 counts or more.

This result demonstrates that there is a field present in the dot which adds a constant offset to any applied field. Since the result is dependent on power it is reasonable to conclude that the field is due to increasing levels of photogenerated charge accumulation. From the energy band diagram in Fig. 3.1 it can be seen that there is nothing in the conduction band that would allow this to occur. However, looking at the valence band (Fig. 3.5) it can be seen that holes can be stored in the capping layer, which alters the band diagram such that any voltage applied to the dot experiences a positive shift ΔV_g.

This effect has been demonstrated previously [10, 11, 12]. Holes can be trapped in the $n = 1$ triangular well energy level formed in the valence band between the capping layer and the superlattice [12]. This can occur due to relaxation of the hole into the capping layer when the sample is excited non-resonantly, or due to hole tunneling from the dot into the capping layer. The electric field experienced by the dot will become smaller with increasing hole storage, which occurs at higher laser powers.

This effect was characterised for the dot in Fig. 3.6. The h-X^0 charging point was recorded against excitation power in Fig. 3.6(black). In order to make a further assessment the sample structure was approximated as three Gaussian surfaces, one at the back contact, one at the capping layer interface, and one at the Schottky gate. Through consideration of Gauss' law [2] it is possible to associate the voltage shift with a hole density at the interface using the following equation

$$N_h = -\frac{\Delta V_g \epsilon_0 \epsilon_r}{ed}, \tag{3.7}$$

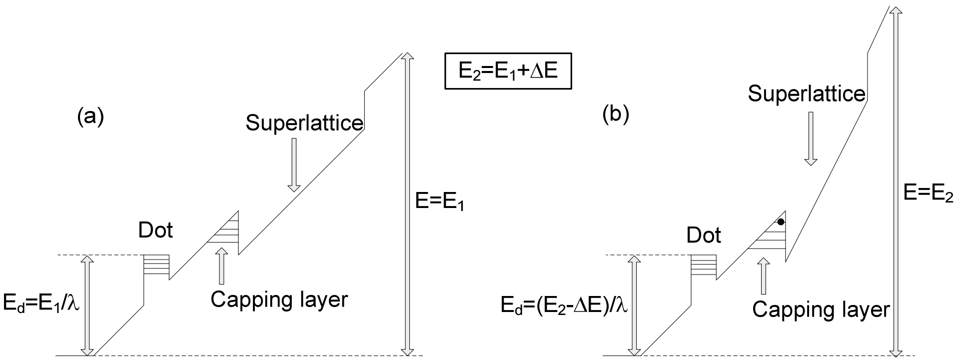

Figure 3.5: Diagram of the wafer valence energy band showing the effect of hole trapping in the capping layer. (a) shows the valence band with no holes trapped. (b) shows the valence band including hole storage effects. The energy (E) is shown relative to the valence band at the back contact. Hole storage causes the energy between the capping layer and the Schottky gate to increase by ΔE. For the dot to have a specific energy (E$_d$), the voltage applied over the wafer in (a) must be larger than that in (b).

where N$_h$ is the hole areal density at the interface, ΔV_g is the voltage shift, ϵ_0 is the dielectric constant for a vacuum, ϵ_r=12.85 is the relative permittivity value for GaAs, e is the electron charge and d=120 nm is the distance from the capping layer to the Schottky gate. Essentially this equation gives the voltage formed between the capping layer interface and the Schottky gate as holes acculmulate in the interface. In this way it was possible to estimate the total number of holes at the capping layer with respect to power for an excitation spot size of 0.25 μm^2 in Fig. 3.6(red).

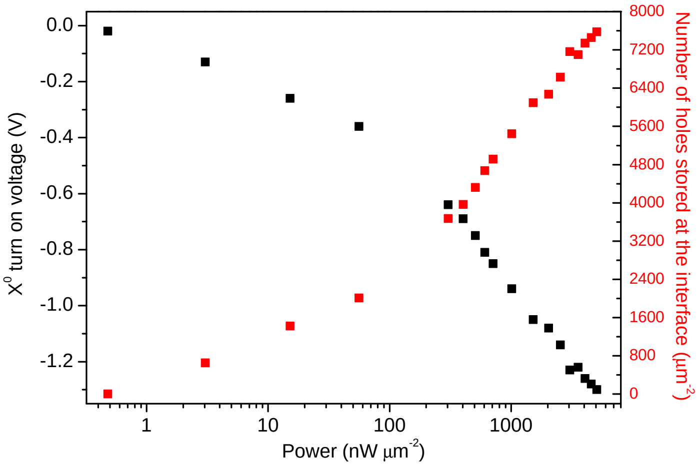

Figure 3.6: Plot recording the h-X^0 charging point (black) alongside the calculated number of holes stored at the interface (red) for the dot in Fig. 3.2, as the power was varied. The estimated laser spot size at the sample surface is 0.25 μm^2.

Hole storage in the capping layer is potentially a problem for use with GHz voltage pulsing. Optical power fluctuations could change the expected dot behaviour at certain gate biases. Hole storage was observed in both Wafer A and Wafer B, however in Wafer B there were some dots that showed very small storage effects (see for example Fig. 3.15(b) in section 3.5). One method of avoiding hole storage in the capping layer is to resonantly excite the dot. In such a situation, holes would be unable to relax into the interface. However, hole tunneling from the dots to the capping layer may still have a negative impact on the PL efficiency, as well as limiting the ability to store holes in the dot during the GHz experiments.

3.3 Lifetime measurements

One of the major goals of this project is to manipulate the electron charge of an exciton in a charge-tunable structure on the time-scale of exciton recombination. In sections 3.1 and 3.2 a detailed knowledge of electron occupation of the dot with respect to an applied voltage bias and with optical excitation power has been established. The time-scales of exciton recombination are presented here for X^{1-}, X^0 and X^{1+}, alongside a discussion of the underlying processes which give rise to the radiative and non-radiative lifetimes. A potential problem has been identified in section 3.2 with respect to hole tunneling from the dot to the capping layer. Simple radiative exciton recombinations within a single dot are expected to display little or no voltage bias dependence (apart from a slight Stark shift), because the voltage does not significantly alter the electron-hole wavefunction overlap. Conversely, a non-radiative process such as tunneling would be likely to exhibit a voltage dependence in time-resolved photoluminescence (TRPL) measurements.

The result of lifetime measurements from several dots in Wafer A (10311A, taken by Paul Dalgarno [2]) allowed the identification of hole tunneling from the dot to the capping layer (see section 3.3.3). In response to this, Wafer B (050328B, see Chapter 2 section 2.6.2) was supplied by Professor Pierre Petroff (University of California, Santa Barbara). Wafer B was designed in order to eliminate hole tunneling, and lifetime measurements are presented here for comparison to Wafer A.

A single dot within a device made from Wafer B (050328B) was excited with 100 ps pulses of non-resonant 826 nm laser light with a repetition rate of 10 MHz and an average power of 6.6 nW μm^{-2}. Time-correlated single photon counting (TCSPC) was performed on X^{1+}, X^0 and X^{1-} against gate bias, and the lifetime values were extracted through reconvolution of the data with the SPAD measurement of the laser response.

3.3.1 The negative trion lifetime

The lifetime data for X^{1-} is presented in Fig. 3.7 (cyan). The negative trion has a single lifetime component at ~900 ps which is not affected by gate bias. Since the two electrons in the dot are in the same energy level, they must have opposite spins (as discussed in Chapter 1). Due to this, there is always a decay path available to the dot. Also, due to the Coulomb blockade (discussed in section 3.1.1) single electron tunneling is prohibited throughout the X^{1-} voltage extent. Therefore, the X^{1-} lifetime gives an example of an unperturbed radiative recombination for an exciton in the dot. TRPL of dots in Wafer A (10311A) also show this behaviour [2].

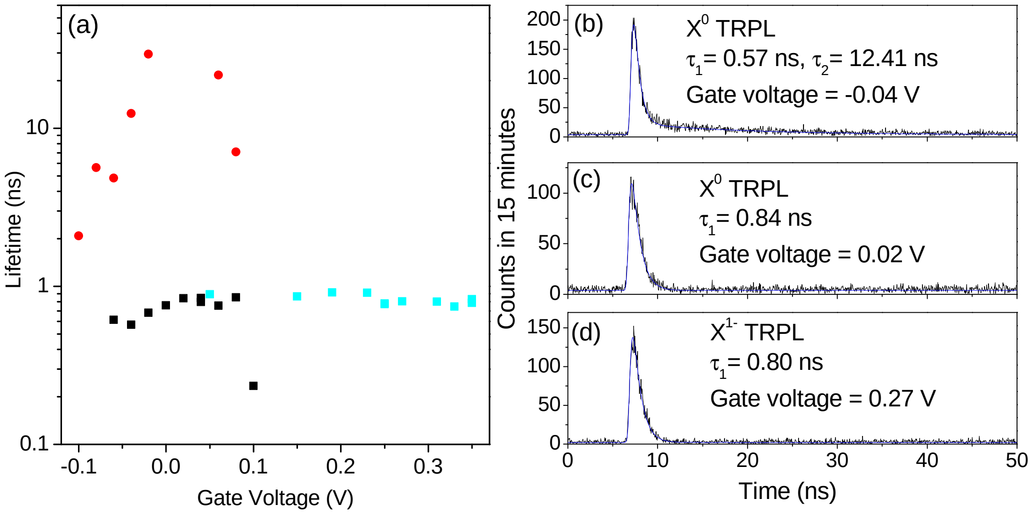

Figure 3.7: (a) The lifetimes obtained from the same dot as in Fig. 3.2, when TCSPC was performed on the PL from X^0 (black and red) and X^{1-} (cyan) as a function of bias, excited with 100ps pulses of non-resonant 826nm laser light at an average power of 6.6 nW μm^{-2}. (b), (c) and (d) are examples of the TRPL obtained (black), including a convolution fit to the data (blue line) as in Chapter 2 section 2.4.2.

3.3.2 The neutral exciton lifetime

TRPL of X^0 has two distinct lifetime components (Fig. 3.7, black and red). The primary lifetime component (black) is ~800 ps and does not vary with gate bias (except near the charging point at 0.1 V where electron tunneling changes the lifetime). The secondary lifetime component (red) can be much larger, several 100 ns in the plateau centre, and drops rapidly at both edges of the plateau. The two lifetimes are indicative of two separate processes which result in recombination. This behaviour also occurs in in Wafer A (10311A) [2].

The bias independent primary lifetime of the neutral exciton is due to radiative recombination of the bright state where the hole and electron have opposite spin (angular momentum $L = \pm 1$). The secondary lifetime is due to the dark exciton [3] in which the hole and electron have the same spin ($L = \pm 2$, discussed in Chapter 1 section 1.3.2). A dark exciton is unable to couple to a photon ($L = \pm 1$) and conserve angular momentum. In order to recombine a dark exciton must therefore first experience a spin flip of either the electron or the hole.

As the X^0 secondary lifetime changes with respect to the electron charging points, it is reasonable to conclude that electron tunneling is responsible for the dark-to-bright spin flip of the neutral exciton. However, first-order electron tunneling is prohibited due to the Coulomb blockade. It is a second-order electron tunneling interaction that allows an electron to swap its spin with the spin of an electron in the back contact through the use of virtual states [3]. As the electron energy level in the dot becomes closer to the Fermi level the electron spin swap interaction occurs at a faster rate, randomising the spin of the electron more quickly and allowing the X^0 to become bright and recombine.

3.3.3 The positive trion lifetime

Shown in Fig. 3.8(a) and (e) is the voltage-dependence of the X^{1+} lifetime extracted from TRPL, for each wafer type. The fitted TRPL for Fig. 3.8(a) are shown in Fig. 3.8(b), (c) and (d). The fitted TRPL for Fig. 3.8(e) are shown in Fig. 3.8(f), (g) and (h). The data in Fig. 3.8(a), (b), (c) and (d) are from Wafer A (10311A), taken from Ref. [13]. The data in Fig. 3.8(e), (f), (g) and (h) are from Wafer B (050328B), measured from the same dot as in Fig. 3.2. The lifetime data in Fig. 3.8(a) are considerably different between other excitons in the same wafer (see sections 3.3.1 and 3.3.2), and between wafers (Fig. 3.8(e)).

In Wafer A (Fig. 3.8(a)), there is a strong bias dependence of the lifetime. From a gate bias of -1.23 V to -1.20 V there is a decrease in lifetime from 0.3 ns to 0.06 ns. This occurs as X^{1+} charges to $2X^0$, and therefore can be attributed to increasingly rapid electron tunneling from the back contact into the dot. There is another lifetime decrease in X^{1+} from a gate bias of -1.23 V to -1.35 V, from 0.3 ns to 0.1 ns, which is accompanied by an associated decrease in PL rate (shown in Ref. [13]). Only in X^{1+} is there a gate dependence of both lifetime and PL intensity, compared with other excitons [13].

Simple radiative recombination (as in the lifetime of X^{1-}, see section 3.3.1) should show no field dependence of the lifetime (apart from a slight Stark shift), because the voltage does not significantly alter the electron-hole wavefunction overlap. This implies that the field dependence of X^{1+} is dominated by carrier tunneling. The Coulomb blockade prohibits first-order electron tunneling in the centre of the X^{1+} voltage extent, and second-order electron tunneling (i.e. an electron spin swap with the back contact) would have no effect due to the lack of fine structure in X^{1+}. Also, the energy difference between X^{1+} and any other charge combination in the dot is far greater than k_BT (0.4 meV at 5 K) [13], so a phonon-enabled change of the electron population in the dot can be ruled out. Therefore, the voltage dependent behaviour of the X^{1+} lifetime is due to hole tunneling.

In order that hole-tunneling can occur for an exciton in the dot, there must be a hole continuum nearby. This is conveniently found in the 2-dimensional triangular

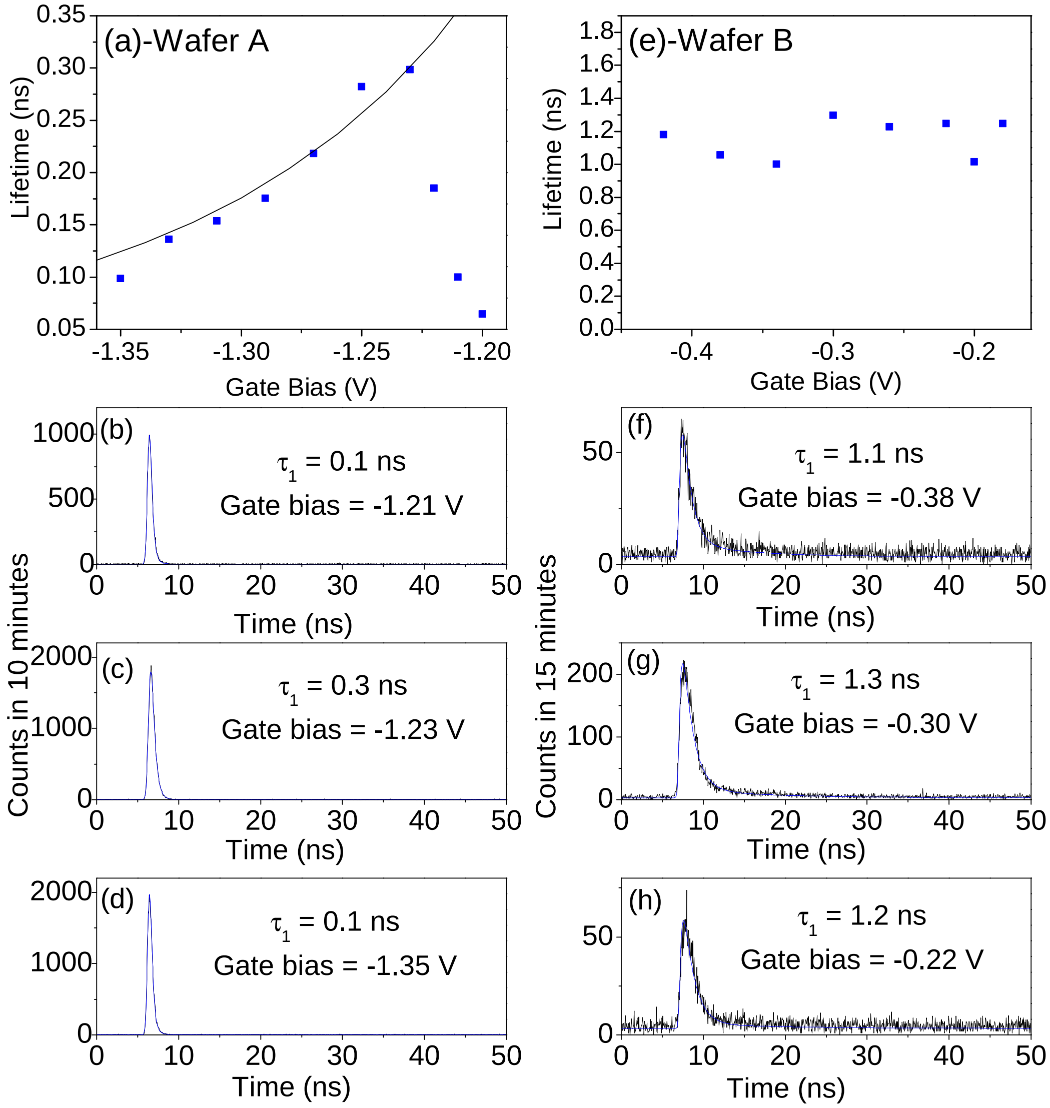

Figure 3.8: (a) The lifetimes obtained from a single dot in Wafer A (10311A) [13]. (b), (c) and (d) are examples of the TRPL obtained in (a) (black), including a convolution fit to the data (blue line) as in Chapter 2 section 2.4.2 (Data taken by Paul Dalgarno). (e) The lifetimes obtained from a single dot in Wafer B (050328B), the same dot as in Fig. 3.2. (f), (g) and (h) are examples of the TRPL obtained in (e) (black), including a convolution fit to the data (blue line) as in Chapter 2 section 2.4.2.

well formed by the capping layer-superlattice interface (see section 3.2 and Fig. 3.5). Looking at the valence band diagram from Fig. 3.5, it is a reasonable assumption that tunneling from the dot to the capping layer occurs through a triangular barrier, and as such the tunneling time (τ_{tun}) between the 0D dot and the 2D capping layer triangular well valence band energy levels can be modeled with a 0D to 1D WKB tunneling approximation with the equation (Fig. 3.8(a), black line) [2, 13]

$$\frac{1}{\tau_{tun}} = \frac{\hbar\pi}{2m_h^\star L}\exp[\frac{-4}{3\hbar eF}\sqrt{2m_h^\star E_v^3}], \tag{3.8}$$

parameterised with the effective hole mass in a GaAs quantum well, $m_h^\star$=0.25m$_0$ [1], the quantum dot height, L=3 nm [14] and the ionisation energy for a hole in the dot E$_v$ (=76.4 meV when X^{1+} is formed in the dot) [2]. F is the applied field, based on the voltage applied over the dots [2]

$$F = \frac{V_{app} + \Delta V_g - V_0}{D}, \tag{3.9}$$

where V_{app}, V_0, and D are defined as in Eqn. 3.1, and $\Delta V_g = -0.6$ V is the shift due to hole storage at the capping layer (see section 3.2). There are no fitting parameters in this model.

There is a close match between the model and the experiment. The hole tunneling rate is suppressed unless the hole energy level is equal to a capping layer energy level [12], as otherwise the momentum of a hole in the capping layer is not conserved when it tunnels into the dot. This suggests that there is a close match between the dot valence s-shell energy level and a capping layer valence energy level when the dot is occupied by X^{1+}. Modeling the lifetime change with a 0D to 3D WKB approximation gives a similarly close fit [13]. Using the Coulomb model, the hole ionisation energies for X^0 and X^{1-} are found to be ~30 meV and ~60 meV larger than for X^{1+}, respectively [2, 13]. Due to this, the hole tunneling times predicted for X^0 and X^{1-} by Eqn. 3.8 are several hundred times larger than their radiative recombination lifetimes [13], which explains why the bias dependent behaviour of the X^{1+} is not seen for X^0 and X^{1-}.

This result represents a large problem with respect to the potential applications of GHz pulses applied to a single quantum dot. Hole spin storage within a quantum dot is not possible for significant time periods in the presence of hole tunneling. A potential solution to the problem of hole tunneling is to alter the energy levels of the capping layer such that tunneling between the dot and the interface is suppressed. One method of achieving this is to reduce the thickness of the capping layer in order to raise the energy levels of the triangular well with respect to the energy levels of the dot. Wafer B (050328B) was constructed for this reason, and the TRPL lifetime data are shown in Fig. 3.8(e). X^{1+} in Wafer B shows a lifetime component at ~1.2 ns, with no voltage bias dependence. Furthermore, the X^{1+} PL rate also shows no voltage bias dependence (see Fig. 3.2).

Using an infinite triangular well model [2, 12, 15] it was possible to calculate the

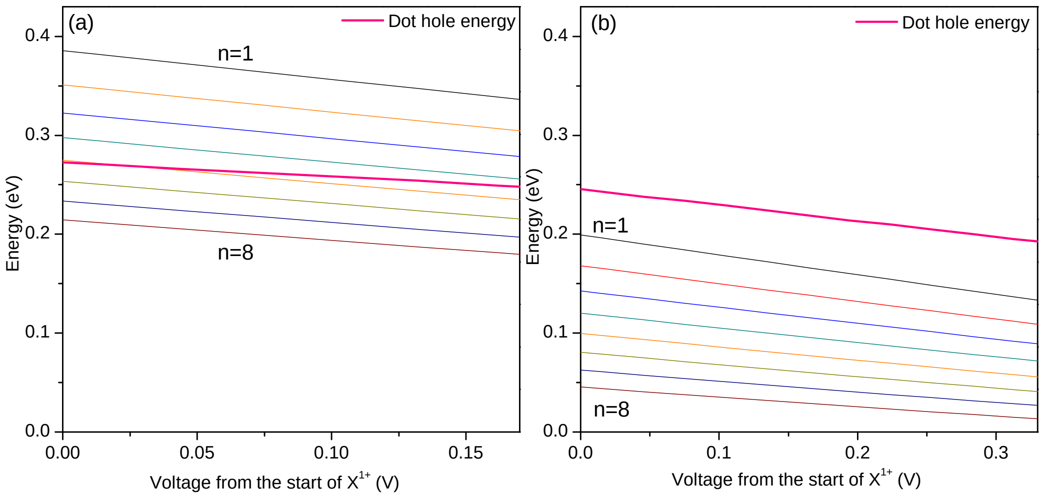

Figure 3.9: Energy of a hole when X^{1+} is formed in the dot (pink), and the energy levels of the triangular well (n=1 to n=8) formed in the capping layer-superlattice interface as the voltage is varied across the X^{1+} extent. (a) shows the energy levels for Wafer A (10311A) using the values E_v=76.4 meV, λ'=3.2, E_i=1.1 meV, V_0=0.62V, $\Delta V_g = -0.600$ V, and D=175 nm. (b) shows the energy levels for Wafer B (050328B) using the values E_v=76.4 meV, λ'=4.4, E_i=1.1 meV, V_0=0.62 V, $\Delta V_g = -0.153$ V and D=155 nm. E=0 is defined here as the Fermi level minus the bandgap energy for GaAs (1.52 eV). In this case the ionisation energy of the hole (E_v) is taken as the ionisation energy of either hole of a X^{1+} in the dot (Ref. [2]).

energy of a hole in X^{1+} within the dot against the energy levels formed in the capping layer-superlattice interface, versus increasing voltage (Fig. 3.9). An infinite triangular well n^{th} energy level has an energy

$$E(n) = (\frac{3}{2}\pi(n - \frac{1}{4}))^{\frac{2}{3}}(\frac{(eF\hbar)^2}{2m^*})^{\frac{1}{3}}, \tag{3.10}$$

where F is the field over the sample (Eqn. 3.9) and m^* is the heavy-hole effective mass ($=0.31m_0$, [16]). Defining E=0 as the Fermi level minus the bandgap of GaAs, the energy levels of the well change with voltage as

$$E(n)_{well} = \frac{e(V_{app} + \Delta V_g - V_0)}{\lambda'} - E(n), \tag{3.11}$$

where V_{app}, ΔV_g and V_0 are defined in Eqn. 3.9, and λ' is the lever arm ratio at the capping layer (=4.4 for Wafer A (10311A), =3.2 for Wafer B (050328B)). This can then be compared with the energy of a hole in X^{1+} within the dot as the voltage changes using

$$E(h)_{dot} = \frac{e(V_{app} + \Delta V_g - V_0)}{\lambda} + E_v - E_i, \tag{3.12}$$

where E_v is defined in Eqn. 3.8 and λ is defined in Eqn. 3.1. E_i is defined in section 3.1.3.

In Wafer B (050328B), the energy of a hole in the dot is ~70 meV higher than the $n = 1$ capping layer energy level (Fig. 3.9(b)). Hole tunneling from the dot to the capping layer cannot occur with this energy difference, explaining why the lifetime in Fig. 3.8(b) shows no bias dependence. This compares with Wafer A (10311A), in which the hole energy is lower than the $n = 1$ capping layer energy level at all points on the X^{1+} extent (Fig. 3.9(a)).

The GHz experiments attempted in this work include hole storage in the dot for significant periods of time. Hole tunneling from the dot to the capping layer would therefore represent a significant disadvantage. The ionisation energy for a single hole in the dot (E_v^0) is expected to be similar to the total ionisation energy for a hole (E_v) when X^{1+} is in the dot, because from the Coulomb model [1, 2, 7]

$$E_v = E_v^0 + E_{eh}^{ss} - E_{hh}^{ss}, \tag{3.13}$$

where E_{eh}^{ss} and E_{hh}^{ss} are the s-shell electron-hole and hole-hole Coulomb energies respectively, which are expected to be similar in value (~30 meV [2]). As such, hole storage experiments using Wafer A (10311A) will have unwanted hole tunneling effects. Due to this, GHz experiments were performed using only Wafer B (050328B).

3.4 Autocorrelation measurements

Quantum dots function as single photon emitters (see Chapter 1 and Ref. [17]). A major goal in the application of GHz bandwidth voltage pulses to a quantum dot is the ability to trigger single photon emission electronically and deterministically. In the previous section it was found that Wafer A (10311A) suffers from hole tunneling effects, which limits its usefulness with respect to the hole storage experiments performed in Chapter 5. Wafer B (050328B) was tested, and does not exhibit hole tunneling effects. However, the capping layer thickness in Wafer B (10 nm) is similar to the height of the quantum dots (∼5 nm), and the dots' ability to emit single photons has never been tested in this structure. In this section, the ability of each Wafer to emit single photons is tested using a d.c. voltage bias and the results are compared.

Autocorrelations were performed on X^{1+}, X^0 and X^{1-} for single dots (different dots to previous sections) in Wafers A and B under non-resonant pulsed optical excitation. The dots were excited with 100 ps pulses from a 826 nm laser with a repetition rate of 20 MHz. The HBT (see Chapter 2 section 2.3) was used to measure the time-correlated PL.

In Wafer A (10311A) the dot studied showed a PL saturation point (P_{sat}, defined in Chapter 2 section 2.4.1) of 2 μW μm^{-2}. Measured in Fig. 3.10 is an autocorrelation plot of the X^{1-} PL emission from the dot in Wafer A when optically excited with $0.05P_{sat}$ at a d.c. gate bias +70 mV from the $X^0 \rightarrow X^{1-}$ charging point (absolute voltage = -0.2 V). Multiple peaks were observed at $t \neq 0$, with a period of 50 ns. As defined in Chapter 1 section 1.4.4 the $g^{(2)}(0)$ value is determined to be 0.028. In other words, multiple-photon emission occurs with ∼3% probability.

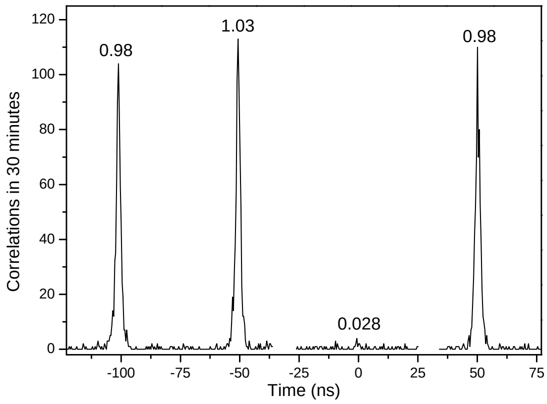

Figure 3.10: Time-resolved histogram showing the correlation of photons for a single dot in Wafer A excited with 100 ps pulses of 826 nm laser light with an average power of 100 nW μm^{-2}, biased at -200 mV so as to form X^{1-}. At each PL peak the normalised count rate has been included. Artifacts due to the SPAD at ±27 ns (see Chapter 2 section 2.3) have been removed.

As the excitation power is increased there is a significant increase in the $g^{(2)}(0)$ value. Measured in Fig. 3.11 is an autocorrelation plot of the X^{1-} PL emission from the same dot as in Fig. 3.10, excited this time with P_{sat} at a d.c. gate bias of -0.2 V. The $g^{(2)}(0)$ value has risen to 0.23, approximately 8 times the value from Fig. 3.10.

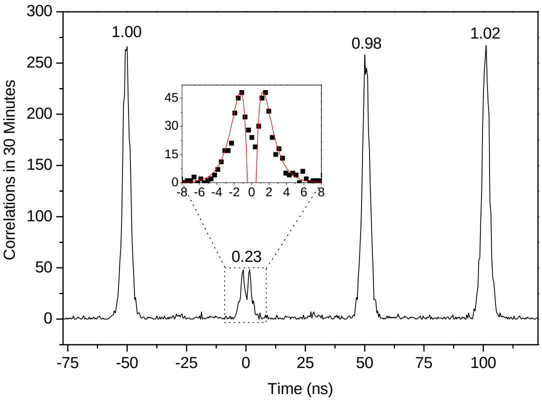

Figure 3.11: Time-resolved histogram showing the correlation of photons for the dot from Fig. 3.10 excited with 100 ps pulses of 826 nm laser light with an average power of 2 μW μm^{-2}, biased at -220 mV so as to form X^{1-}. The dip in the $g^{(2)}(0)$ feature (see inset) consists of 5 data points. The red line is a fit to the data using Eqn. 3.15 with the values τ_{cap}=0.6 ns and τ_{rad}=1.05 ns.

Fig. 3.12(a) records the $g^{(2)}(0)$ value for three different powers (P_{sat}, $0.5P_{sat}$ and $0.05P_{sat}$) as a function of d.c. voltage bias, for X^0 and X^{1-} from the same dot as in Fig. 3.10. $g^{(2)}(0)$ exhibits a bias dependence for both excitons, but does not have any obvious change with a change of dot charge.

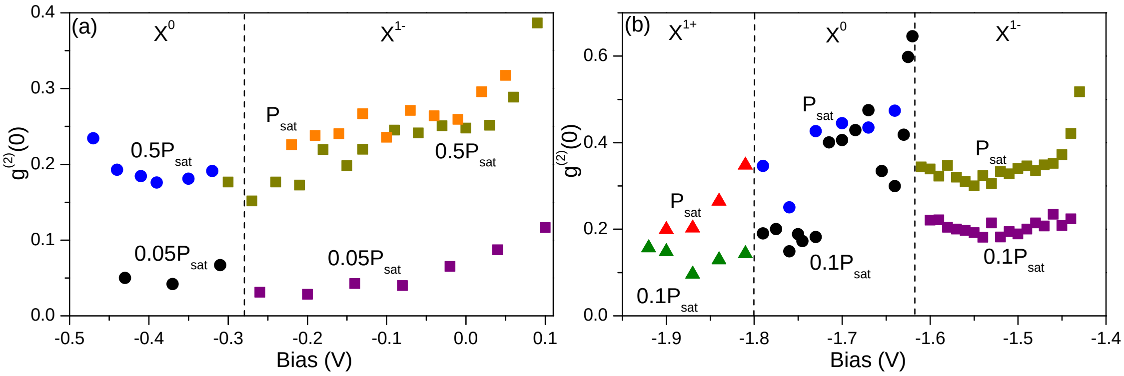

Figure 3.12: Plot showing $g^{(2)}(0)$ values for X^{1+} (red and green), X^0 (black and blue) and X^{1-} (purple and yellow) against gate bias for (a) the dot in Fig. 3.10 (Wafer A, 10311A), and (b) a dot in wafer Wafer B (050328B), taken for several excitation powers relative to P_{sat}.

Fig. 3.11 shows a minimum in correlations at time zero (see inset). Within several ns there is an increase in correlations, despite the excitation pulse being only ~100 ps duration. This implies there is a carrier recapture process which occurs after the initial emission of a photon [18, 19, 20]. Photogenerated charge must be able to relax into the dot, forming an exciton and resulting in re-emission of a second exciton within the same excitation cycle, a few nanoseconds later. The charge tunable structure gives complete control over the electron charge through the Coulomb blockade (discussed earlier in this chapter), which shows no electron tunneling outwith several small voltage regions. Therefore, the recapture process must be related to hole dynamics.

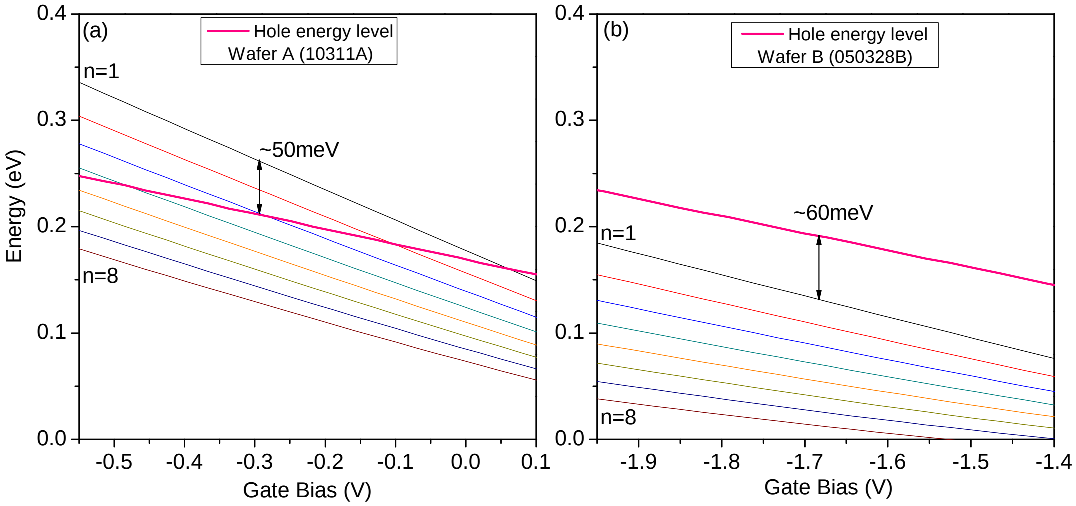

Figure 3.13: Energy of a hole in the dot (pink), and the energy levels of the triangular well (n=1 to n=8) formed in the capping layer-superlattice interface as the voltage is varied. (a) shows the energy levels for Wafer A (10311A) using the values $E_v = E_v^0 = 78$ meV [2], λ'=3.2, E_i=1.1 meV, V_0=0.62V, $\Delta V_g = -0.038$ V, and D=175 nm. (b) shows the energy levels for Wafer B (050328B) using the values $E_v = E_v^0$=78 meV, λ'=4.4, E_i=1.1 meV, V_0=0.62 V, $\Delta V_g = -1.585$ V , and D=155 nm. E=0 is defined here as the Fermi level minus the bandgap energy for GaAs (1.52 eV). In this case the ionisation energy for the hole (E_v) is taken as the ionisation energy of a single hole in the dot ($E_v = E_v^0$). This is different to Fig. 3.9, in which the ionisation energy of the hole is taken as the ionisation energy of either hole of a X^{1+} in the dot (see equation 3.13).

The capping layer contains a reservoir of holes. Is it possible that the hole recapture is due to hole tunneling from the capping layer to the dot? In the triangular well formed by the capping layer the photogenerated carrier density based on the voltage shift (ΔV_g) with optical excitation power is estimated to be less than 1000 holes μm^{-2} at P_{sat} [20]. From this the 2D Fermi energy in the well (ε_F) can be calculated from [15],

$$\varepsilon_F = \frac{\hbar^2 \pi N_h}{m^*}, \tag{3.14}$$

where N_h is the areal carrier density in the well, and $m^* = 0.31 m_0$ as defined in section 3.3.3. A value of $\varepsilon_F \sim$0.8 meV is obtained, which is much smaller than the energy of the n=1 level in the triangular well (between 22 meV and 45 meV at all relevant gate biases, calculated using Eqn. 3.10). Therefore it is reasonable to assume that any holes present in the triangular well will occupy the n=1 energy level at T=5 K. Any hole tunneling from the capping layer to the dot will therefore depend entirely on the n=1 energy level of the triangular well. In Wafer A (10311A), at the low bias end of the X^{1-} plateau (∼-0.3 V, Fig. 3.12(a)), the n=1 energy level of the triangular well is approximately 50 meV higher in energy than the valence s-orbital of the dot (Fig. 3.13(a)). For the majority of the X^{1-} plateau (until ∼0.05 V) the n=1 energy level of the triangular well remains significantly higher than the energy level of the dot. A reasonable conclusion is therefore that hole recapture in this sample is **not** due to hole tunneling from the triangular well to the dot.

Another suggestion is that the dot recaptures holes from the wetting layer. The bandgap difference between GaAs (1.52 eV) and the InAs wetting layer (1.46 eV) is ∼60 meV. The ratio of the wetting layer valence band hole confinement energy to the conduction band electron confinement energy is 1:0.58 (taken from [22]). From this, the valence band hole confinement energy is calculated as ∼22 meV, which is ∼55 meV lower in energy than the valence s-orbital of the dot. It is possible that some holes are trapped in localised potential fluctuations in the wetting layer [23]. After the dot has emitted a photon, a trapped hole in the wetting layer could relax into the dot. Once the hole is present in the dot, either one or two electrons will tunnel into the dot from the back contact depending on the bias, forming X^0 or X^{1-} (see section 3.1.3). The exciton that is formed will then decay to release a secondary photon. This would explain why increasing the optical excitation power causes an increase in the $g^{(2)}(0)$ values (Fig. 3.12(a)): the increase in photogenerated holes leads to an increased hole concentration in the wetting layer, increasing the probability of hole recapture into the dot. Because of this, it is expected that the $g^{(2)}(0)$ feature at $0.05P_{sat}$ would show a similar splitting to the higher power autocorrelations if an increased signal to noise were obtained.

The rise and fall times of the $g^{(2)}(t=0)$ feature in Fig. 3.11 can be fitted in order to estimate the recapture and re-emission times (τ_{cap} and τ_{rad}, respectively). Fig. 3.11(inset, red line) shows a exponential fit to the data using a three level rate equation model [21]

$$g^2(t) \propto [\exp(\frac{-t}{\tau_{cap}}) - \exp(\frac{-t}{\tau_{rad}})]/(\tau_{cap} - \tau_{rad}), \tag{3.15}$$

where τ_{cap} and τ_{rad} are fit to the data with 0.6 ns and 1.05 ns respectively. Accounting for an ∼400 ps instrumental response from the SPADs gives τ_{rad}=0.97 ns, which agrees with the value of 0.97 ns found by reconvolution of TRPL from X^{1-}. From this, a tentative value of ∼450 ps is proposed as the recapture time. This suggests that although two or more photons can be emitted during the same excitation cycle they are not emitted simultaneously, and with an increased temporal resolution the value of $g^{(2)}(t=0)$ would fall to zero.

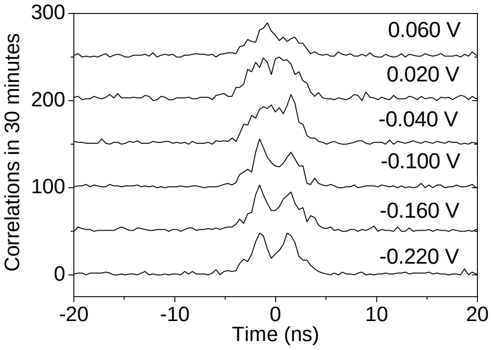

Figure 3.14: Time-resolved measurements of the $g^{(2)}(0)$ peak from the dot in Wafer A (10311A) as the bias is increased, while excited with 100 ps pulses from a 826 nm laser with a repetition rate of 20 MHz, at P_{sat}. The data are offset from each other by 50 correlations.

In Fig. 3.12(a), an increase in $g^{(2)}(0)$ value is observed as the bias increases. Fig. 3.14 presents a close-up of the $g^{(2)}(0)$ feature for X^{1-} as the bias increases, from the dot in Fig. 3.12(a) at P_{sat}. The time-splitting between the peaks of the $g^{(2)}(0)$ feature reduces as the bias increases, suggesting that the value for τ_{cap} is reducing substantially, which is explained by a higher hole accumulation in the wetting layer. The explanation for this is that hole recapture occurs from the wetting layer, and increasing the bias increases the width of the triangular barrier between the dot and the capping layer interface. The tunneling rate from the wetting layer to the capping layer would be reduced with increasing bias, and a larger hole accumulation at the wetting layer would lead to a greater probability of recapture into the dot.

Now that the dynamics behind single photon production are known for Wafer A (10311A), it is possible to comment on the differences with respect to Wafer B (050328B). Fig. 3.12(b) on page 60 shows $g^{(2)}(0)$ as a function of gate bias for X^{1+}, X^0 and X^{1-} for two different excitation powers, P_{sat} and $0.1P_{sat}$ (0.2 μW μm^{-2} and 0.02 μW μm^{-2} for Wafer B, respectively). The $g^{(2)}(0)$ values for Wafer B are approximately twice that of Wafer A. The probability of hole recapture is therefore higher in Wafer B. This is explained by Fig. 3.13(b) on page 61 which shows the energy of the valence s-orbital for the dot with respect to the energy levels in the triangular well. The valence s-orbital for the dot is ~60 meV higher in energy than the triangular well valence energy levels, which means the wetting layer valence band is ~5 meV higher in energy than the triangular well valence energy levels. In Wafer B, holes will not be able to tunnel from the wetting layer into the capping layer interface, and a greater hole density is formed at the wetting layer. As such, the probability of hole recapture into the dot is larger for Wafer B compared to Wafer A, and similarly the $g^{(2)}(0)$ values are larger for Wafer B.

Hole recapture in quantum dots is potentially a large problem for creating an efficient deterministic single photon source, which is one of the major goals of this project. However, an increased temporal resolution in autocorrelation measurements would potentially show that the dots continue to emit single photons. A solution would be to use resonant excitation below the wetting layer band gap, which would avoid the issue of hole storage completely.

3.5 Resonant CW excitation of X^0

From sections 3.3.3 and 3.4 there are two clear outcomes concerning the application of GHz pulses over a quantum dot. Firstly, Wafer B is preferred in order that hole spin storage and readout is possible for significant storage times. Secondly, a method using resonant excitation would be preferable, as this would avoid hole recapture problems that exist with non-resonant excitation.

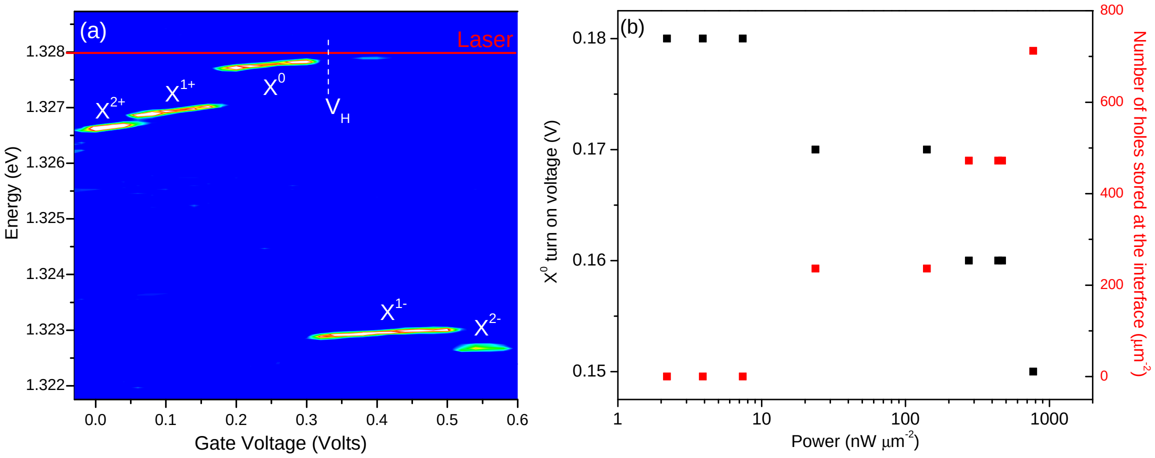

Figure 3.15: (a) The PL against gate bias for a single dot in Wafer B (different from previous dots) excited with a non-resonant CW 830 nm laser at a power of 3.9 nW μm^{-2}. The exciton responsible for each PL line is labelled. The tunable laser energy used in the resonant experiment is shown as a red line. V_H is marked at a point 15 mV beyond the low field edge of the X^0 plateau. Blue $\simeq$90 counts (approximately the readout noise of the spectrometer CCD camera), green $\simeq$110 counts, yellow $\simeq$120 counts, red $\simeq$130 counts, white = 150 counts or more. (b) The h-X^0 charging point (black) alongside the calculated number of holes stored at the interface (red, calculated using Eqn. 3.7 in section 3.2) for the dot in (a), as the excitation power was varied. The estimated spot size at the sample surface is 0.25 μm^2.

Fig. 3.15(a) shows the PL from a single dot (a different dot from previous sections) in Wafer B (050328B) that has been excited with 3.9 nW μm^{-2} of non-resonant 830 nm CW laser light. There is no voltage shift of the charging points at lower excitation powers (Fig. 3.15(b)), which suggests there is no hole storage in the capping layer at this power. The excitons are identified in the same way as explained in section 3.1.2. At a gate bias 15 mV higher than the $X^0 \rightarrow X^{1-}$ charging point, V_H marks a ~30 mV region in which the lowest one hole state is X^{1-}, and the lowest state without any holes is $\mid 0\rangle$ (identified previously in section 3.1.3 for a different dot). This occurs due to the difference between the values for E_{ee}^{ss} and E_{eh}^{ss}, as can be seen on inspection of the Coulomb blockade model [1, 2, 7, 12], which gives

$$V_2 - V_1 = \lambda(E_{eh}^{ss} - E_{ee}^{ss}), \tag{3.16}$$

where V_1 is the voltage at which the energy of a neutral exciton is equal to the energy of a negative trion, and V_2 is the voltage at which the energy of a single electron in the dot is equal to the Fermi level. Fig. 3.16 shows an energy level diagram for the region at V_H, for the dot in Fig. 3.15. The Coulomb model returns values of E_{ee}^{ss}=18.6 meV and E_{eh}^{ss}=23.4 meV when applied to this dot, which (using Eqn. 3.16) returns a value of 29.8 mV for the voltage extent between V_1 and V_2.

A novel resonant excitation scheme is available within the bias region between V_1 and V_2. This is highlighted using the labelled arrows **A**, **B**, and **C** in Fig. 3.16. Starting with an empty dot ($\mid 0\rangle$), resonant excitation (**A**) populates the dot with a single neutral exciton. A second electron will tunnel into the dot from the back contact (**B**), forming X^{1-}. Electron-hole recombination will release a photon which is spectrally filtered and measured, and the dot will be left with a single electron. The electron in the dot will then tunnel into the back contact (**C**), leaving an empty dot ($\mid 0\rangle$) which is free to start another excitation cycle.

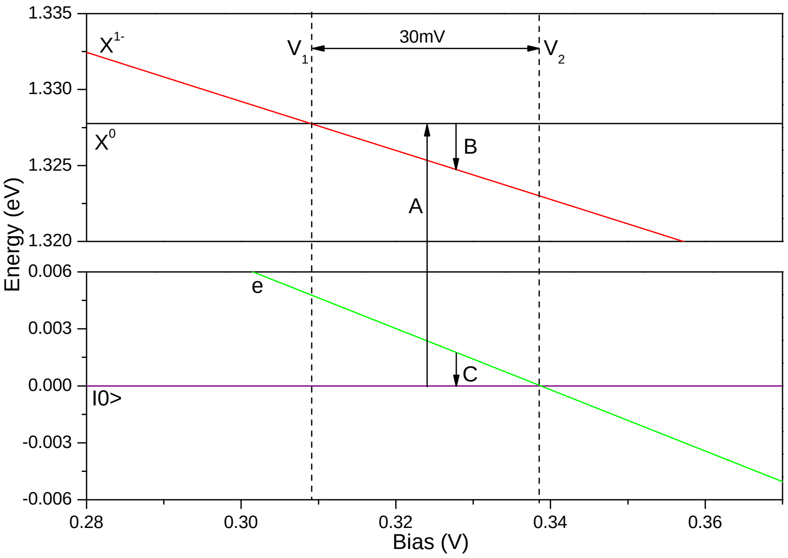

Figure 3.16: The Coulomb model fitted to the dot in Fig. 3.15 with ΔV_g=-0.374 V, λ=6.2, V_0=0.62 V, E_0=1.328 eV, E_c=107 meV, E_i=-1.1 meV, E_{ee}^{ss}=18.6 meV and E_{eh}^{ss}=23.4 meV.

The excitation energy of the $\mid 0\rangle \rightarrow X^0$ transition (Fig. 3.16, **A**) at ~330 mV gate bias was estimated using Fig. 3.15. At bias voltages between V_1 and V_2, no PL is recorded from X^0. The energy of the $\mid 0\rangle \rightarrow X^0$ transition changes linearly with voltage due to the Stark shift. Using the Stark shift observed across the X^0 plateau in Fig.

3.15 as a guide, the $\mid 0\rangle \rightarrow$X^0 transition energy was estimated at 1.328 eV for a gate bias of ~330 mV.

A 1 MHz bandwidth tunable laser was used to excite the dot with 1.328 eV CW light (represented as a red line in Fig. 3.15), at a power of 4 mW μm^{-2}. The PL and reflected laser light were coupled into the spectrometer. Excessive light levels incident on the spectrometer silicon detector array can cause a charge build up on the pixels, and when any one pixel is full charge can leak into the surrounding pixels, causing an increase in noise levels. In order to avoid this, the blazed grating in the spectrometer was angled such that any reflected laser light (at 1.328 eV) from the sample surface was diffracted away from the silicon detector array, but the X^{1-} PL (at 1.323 eV) was still incident on the chip.

Fig. 3.17(a) shows the X^{1-} PL against gate bias for the same dot as in Fig. 3.15, excited with 4 mW μm^{-2} of CW laser light at 1.328 eV. The X^{1-} PL emission has a bias extent of ~50 mV, which is considerably larger than the ~30 mV range expected from the Coulomb model in Fig. 3.16. Within the region between V$_1$ and V$_2$ X^{1-} PL emission is observed, confirming that after emission of a photon, a single electron is left in the dot which tunnels into the back contact. At biases higher than V$_2$ electron tunneling does not occur (because a single electron in the dot has a lower energy than $\mid 0\rangle$, see Fig. 3.16), the system does not reset to $\mid 0\rangle$ after the first excitation cycle, and the dot does not have the ability to absorb another photon from the laser. As such Fig. 3.17(a) does not show X^{1-} PL at gate biases higher than V$_2$. At biases lower than V$_1$, the dot should not have the ability to form X^{1-}. From Fig. 3.16 we can see that at the low bias end of the X^{1-} PL (0.29V), X^{1-} is actually 3 meV higher in energy than X^0, which is ~8 times k$_B$T (0.4 meV). It is unknown why X^{1-} PL is observed at gate biases lower than V$_1$.

Fig. 3.17(b) shows the linewidth of the X^{1-} PL from Fig. 3.17(a), against gate bias. The linewidth decreases with increasing voltage bias, and shows a pronounced dip slightly beyond V$_1$ (centred at 317 mV), where X^0 charges to become X^{1-} (as observed in Fig. 3.15). The linewidths are symmetric (see Fig. 3.18), which suggests that there is no coherent interaction between the dot and the back contact [8]. Fig. 3.17(c) shows the total intensity of the X^{1-} PL from Fig. 3.17(a), against gate bias. The intensity reaches a peak at ~317 mV.

Fig. 3.19 shows the normalised X^{1-} PL rate recorded with changing laser energy for a different dot in Wafer B, with a gate bias ~15 mV beyond the low field edge of the X^0 plateau (marked V$_H$ for the similar dot in Fig. 3.15) and a power of 60 μW μm^{-2}. The fitted Lorentzian (red line) shows that X^0 has an incredibly large absorption range with this region, with approximately 0.14 meV linewidth. This is far larger than a normal exciton linewidth (a few μeV). The X^0 PL energy range is marked, and the absorption range extends into this energy region.

This method of resonant excitation and PL collection is unique as it does not rely on the usual methods of detection, such as absorption microscopy [24], or excitation

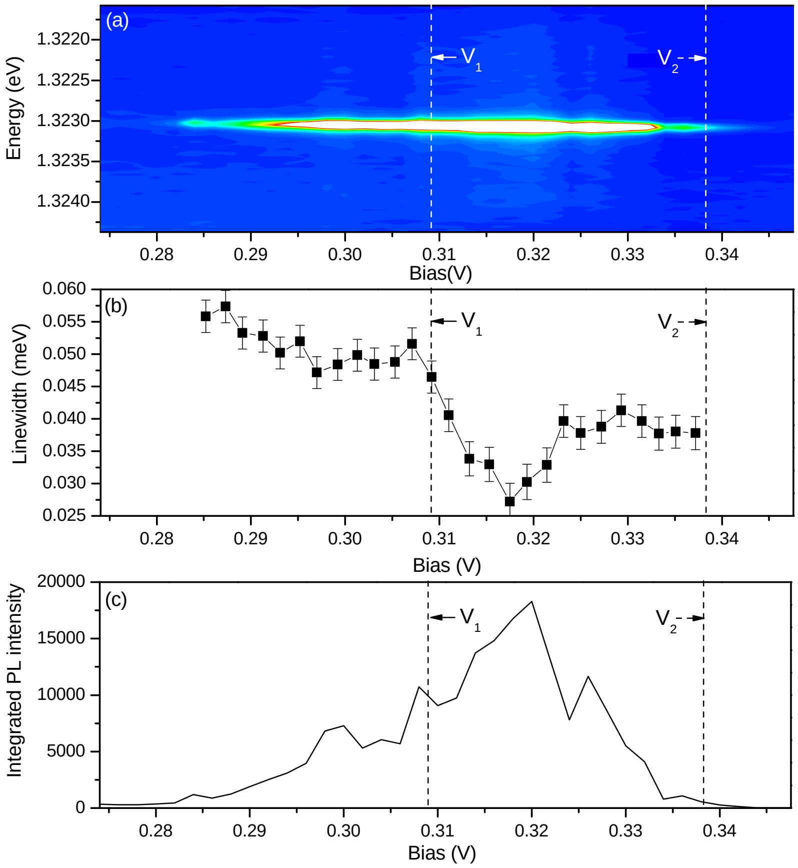

Figure 3.17: (a) Contour showing the X^{1-} PL from the dot in Fig. 3.15 as a function of bias, when resonantly excited into X^0 with a 1.338 eV CW laser at a power of 4 mW μm^{-2}. Blue $\simeq$100 counts, green $\simeq$300 counts, yellow $\simeq$800 counts, red $\simeq$1000 counts, white = 1500 counts or more. (b) The linewidth against bias measured from the PL of X^{1-} in (a). (c) The total intensity against bias for the PL of X^{1-} in (a). V_1 marks the bias point at which X^{1-} and X^0 have equal energy (measured from the low power contour in Fig. 3.15(a)). V_2 marks the bias point at which $\mid 0\rangle$ has the same energy as a single electron (Estimated from the application of the Coulomb model to the dot, Fig. 3.16).

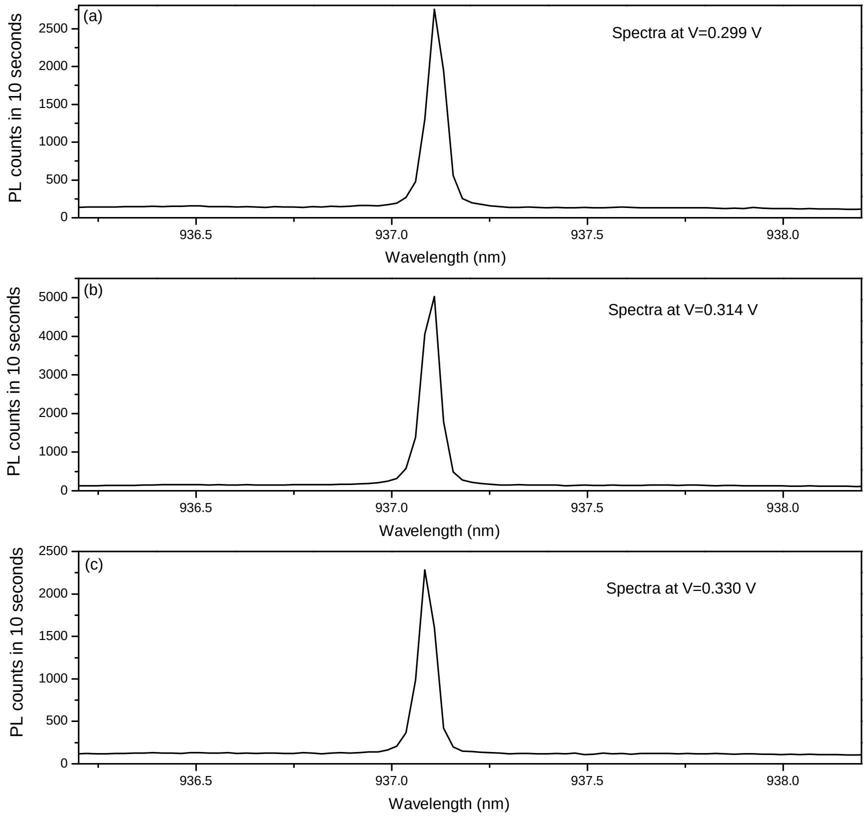

Figure 3.18: Spectra of X^{1-} PL from Fig. 3.17(a) for three different d.c. voltage biases. (a),(b) and (c) are spectra taken at 0.299 V, 0.314 V and 0.330 V respectively.

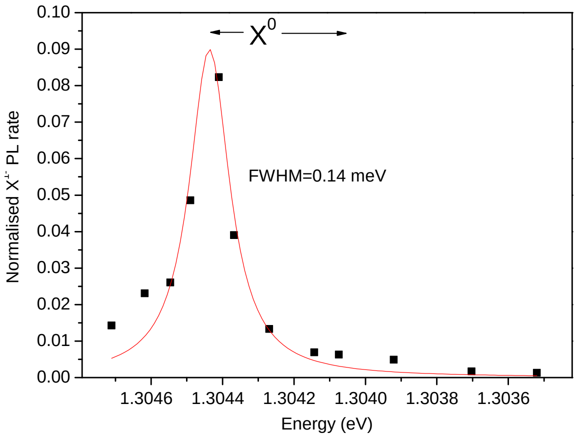

Figure 3.19: Plot showing the X^{1-} PL counts against laser energy, at a power of ~60 mW μm^{-2} for a different dot to that in Fig. 3.15 (in Device D, Wafer B). Included is the X^0 PL energy extent due to the Stark shift, showing that the interaction region between the tunable laser and the dot is centred at the high energy (and therefore high bias) edge of X^0. A Lorentzian lineshape is fitted (red line) with a width of 0.14 meV.

within a waveguide mode [25]. GHz bandwidth voltage pulsing is used in conjunction with resonant excitation in Chapter 5, in order to avoid the hole storage and recapture effects seen in section 3.4.

3.6 Conclusion

The behaviour of a quantum dot under an applied d.c electric field, with and without optical excitation, was discussed and characterised for use with GHz bandwidth voltage pulsing. First-order electron tunneling between the dot and the back contact was identified, and related to a Coulomb blockade model for charge-tunable structures. Hole storage was identified at the capping layer-superlattice interface of the structure. Recombination lifetimes for neutral and singly-charged excitons were recorded for two different wafer structures. Furthermore, the field-dependent nature of the exciton lifetimes were used to identify second-order electron tunneling between the dot and the back contact, and also hole tunneling between the dot and the capping layer-superlattice interface. Autocorrelation data was taken for both wafer structures, and used to identify a hole recapture process between the dot wetting layer and the dot. Lastly, resonant excitation of X^0 was performed, using a novel method that takes advantage of the difference between the electron-electron and electron-hole Coulomb energies in the dot. From the data, a single wafer (Wafer B, 050328B) was designed and tested for use with GHz bandwidth voltage pulses.

References

[1] R. J. Warburton, B. T. Miller, C. S. Dürr, C. Bödefeld, K. Karrai, J. P. Kotthaus, G. Medeiros-Ribeiro, P. M. Petroff and S. Haunt, *Coulomb interactions in small charge-tunable quantum dots: A simple model.* Physical Review B, **58**, 16221 (1998).

[2] P. A. Dalgarno, Thesis title: *Time correlated single photon counting on charge tunable quantum dots.* (2005).

[3] J. M. Smith, P. A. Dalgarno, R. J. Warburton, A. O. Govorov, K. Karrai, B. D. Gerardot and P. M. Petroff, *Voltage control of the spin dynamics of an exciton in a semiconductor quantum dot.* Physical Review Letters, **94**, 197402 (2005).

[4] B. T. Miller, W. Hansen, S. Manus, R. J. Luyken, A. Lorke, J. P. Kotthaus, S. Haunt, G. Medeiros-Ribeiro and P. M. Petroff, *Few-electron ground states of charge-tunable self-assembled quantum dots.* Physical Review B, **56**, 6764 (1997).

[5] R. J. Warburton, C. S. Durr, K. Karrai, J. P. Kotthaus, G. Medeiros-Ribeiro and P. M. Petroff, *Charged excitons in self-assembled semiconductor quantum dots.* Physical Review Letters, **79**, 5282 (1997).

[6] R. J. Warburton, C. Schäflein, D. Haft, F. Bickel, A. Lorke, K. Karrai, J. M. Garcia, W. Schoenfeld and P. M. Petroff, *Optical emission from a charge-tunable quantum ring.* Nature, **405**, 926 (2000).

[7] M. Ediger, P.A. Dalgarno, J. M. Smith, B. D. Gerardot, R. J. Warburton, K. Karrai and P. M. Petroff, *Controlled generation of neutral, negatively-charged and positively-charged excitons in the same single quantum dot.* Applied Physics Letters, **86**, 211909 (2005).

[8] P. A. Dalgarno, M. Ediger, B. D. Gerardot, J. M. Smith, S. Seidl, M. Kroner, K. Karrai, P. M. Petroff, A. O. Govorov and R. J. Warburton, *Optically induced hybridization of a quantum dot state with a filled continuum.* Physical Review Letters, **100**, 176801 (2008).

[9] S. Laurent, B. Eble, O. Krebs, A. Lemaitre, B. Urbaszek, X. Marie, T. Amand and P. Voisin, *Electrical control of spin relaxation in charge tunable InAs/GaAs quantum dots.* Physical Review Letters, **94**, 147401 (2005).

[10] B. Urbaszek, E. J. McGhee, J. M. Smith, R. J. Warburton, K. Karrai, B. D. Gerardot, J. M. Garcia and P. M. Petroff, *Charged excitons in individual quantum dots: effects of vertical electric fields and optical pump power.* Physica E, **17**, 35 (2003).

[11] J. M. Smith, P. A. Dalgarno, B. Urbaszek, E. J. McGhee, G. S. Buller, G. J. Nott and R. J. Warburton, *Carrier storage and capture dynamics in quantum-dot heterostructures.* Applied Physics Letters, **82**, 3761 (2003).

[12] S. Seidl, M. Kroner, P. A. Dalgarno, A. Hogele, J. M. Smith, M. Ediger, B. D. Gerardot, J. M. Garcia, P. M. Petroff, K. Karrai and R. J. Warburton, *Absorption and photoluminescence spectroscopy on a single self-assembled charge-tunable dot.* Physical Review B, **72**, 195339 (2005).

[13] P. A. Dalgarno, J. McFarlane, B. D. Gerardot, R. J. Warburton, K. Karrai, A. Badolato and P. M. Petroff, *Decay dynamics of the positively charged exciton in a single charge tunable self-assembled quantum dot.* Applied Physics Letters, **89**, 043107 (2006).

[14] D. Granados and J. M. Garcia, *In(Ga)As self-assembled quantum ring formation by molecular beam epitaxy.* Applied Physics Letters, **82**, 2401 (2003).

[15] J. H. Davies, *The physics of low-dimensional semiconductors.* Cambridge University Press, (1997).

[16] D. Reuter, P. Kailuweit, A. D. Wieck, U. Zeitler, O. Wibbelhoff, C. Meier, A. Lorke and J. C. Maan, *Coulomb-interaction-induced incomplete shell filling in the hole system of InAs quantum dots.* Physical Review Letters, **94**, 026808 (2005).

[17] V. Zwiller, T. Aichele and O. Benson, *Quantum optics with single quantum dot devices.* New Journal of Physics, **6**, 96 (2004).

[18] T. Aichele, V. Zwiller and O. Benson, *Visible single-photon generation from semiconductor quantum dots.* New Journal of physics, **6**, 90 (2004).

[19] E. Peter, S. Laurent, J. Bloch, J. Hours, S. Varoutsis, I. Robert-Philip, A. Beveratos, A. Lemaître, A. Cavanna, G. Patriarche, P. Senellart and D. Martrou, *Fast radiative quantum dots: From single to multiple photon emission.* Applied Physics Letters, **90**, 223118 (2007).

[20] P. A. Dalgarno, J. McFarlane, D. Brunner, R. W. Lambert, B. D. Gerardot, R. J. Warburton, K. Karrai, A. Badolato and P. M. Petroff, *Hole recapture limited single photon generation from a single n-type charge-tunable quantum dot.* Applied Physics Letters, **92**, 193103 (2008).

[21] G. Bastard, *Wave mechanics applied to semiconductor heterostructures.* Halstead, New York (1988).

[22] J. Brübach, A. Y. Silov, J. E. M. Haverkort, W. V. D. Vleuten and J. H. Wolter, *Coupling of ultrathin InAs layers as a tool for band-offset determination.* Physical Review B, **59**, 10315 (1999).

[23] E. S. Moskalenko, M. Larsson, W. V. Schoenfeld, P. M. Petroff and P. O. Holtz, *Carrier transport in self-organized InAs/GaAs quantum-dot structures studied by single-dot spectroscopy.* Physical Review B, **73**, 155336 (2006).

[24] B. Alen, F. Bickel, K. Karrai, R. J. Warburton and P. Petroff, *Stark-shift modulation absorption spectroscopy of single quantum dots.* Applied Physics Letters, **83**, 2235 (2003).

[25] A. Muller, E. B. Flagg, P. Bianucci, X. Y. Wang, D. G. Deppe, W. Ma, J. Zhang, G. J. Salamo, M. Xiao, C. K. Shih, *Resonance fluorescence from a coherently driven semiconductor quantum dot in a cavity.* Physical Review Letters, **99**, 187402 (2007).

Chapter 4

Construction of a GHz bandwidth device

The application of GHz bandwidth voltage pulses to a charge-tunable quantum dot heterostructure necessitated an investigation into the frequency response of the macroscopic devices. In this section the macroscopic device construction is detailed, and tests to the device show an inability to respond to a GHz bandwidth voltage pulse. The resistive and capacitive properties of the device were reduced by designing and realising a micron-scale device using photolithography and e-beam evaporation. Two small devices were created, one with an easily accessible Ohmic contact placed $\sim$3 mm from the Schottky gate, and the other with a low-resistance Ohmic contact placed $\sim$10 μm from the Schottky gate. Optical measurements were conceived and performed on both devices in order to determine their respective response times to an applied voltage.

4.1 The original (macroscopic) samples

It was desirable that a dot within a charge-tunable structure could respond to GHz bandwidth voltage pulses. In order to achieve this, devices were constructed in the same style as those currently being used for experiments with a d.c. voltage bias [1, 2, 3]. An investigation of the voltage response bandwidth was performed, with a view to increasing the bandwidth by altering the design.

4.1.1 Preparation of the sample

A 3 mm x 3 mm sample was cleaved from the unprocessed 2” diameter wafer (Wafer B, 050328B) using a diamond tipped scribe, and washed in an acetone ultrasonic bath. Indium wire was cut into small cubes using a razor blade and sharp tweezers. Any oxidised metal was removed from the cubes and discarded. Four cubes were positioned on the top surface of the sample. The sample surface was then cleaned in a 10% hydrogen- 90% nitrogen-atmosphere using a small amount of weak sulphuric acid vapour. Finally, a Biorad alloying furnace was used to heat the sample to 350° C for 40 minutes, causing the indium to anneal through the sample surface. The result was the formation of indium Ohmic contacts to the wafer back contact [4] as in Fig. 4.1. A successful sample shows sub-kΩ resistance between indium cubes. A typical success rate of ∼50% per sample was found using this process.

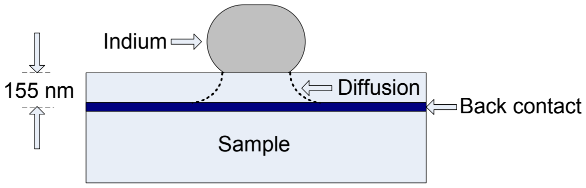

Figure 4.1: Conceptual side view of the sample showing annealed indium forming an Ohmic contact with the back contact.

A shadow mask with a keyhole design (a 2 mm diameter circle with a 1 mm x 1 mm square section protruding from one point on the edge) is used in a thermal evaporator at ∼1x10^{-5} mbar in order to create a 5 nm semi-transparent NiCr Schottky gate on the top surface of the device. A hemispherical SIL was placed on the circular section of the keyhole design using a very small amount of vacuum grease. The completed sample was then glued to a metal holder using Oxford GE varnish. Two thin wires were connected from a d.c. variable voltage supply to two fixed (and insulated) points on the metal holder, creating a strain relief system. The wires continued to the sample from the strain relief point. One wire was contacted to the Schottky gate, and the other to the indium cubes, using high conductive silver paint purchased from RS. In this way a voltage could be applied between the Schottky gate and the back contact of the charge-tunable structure.

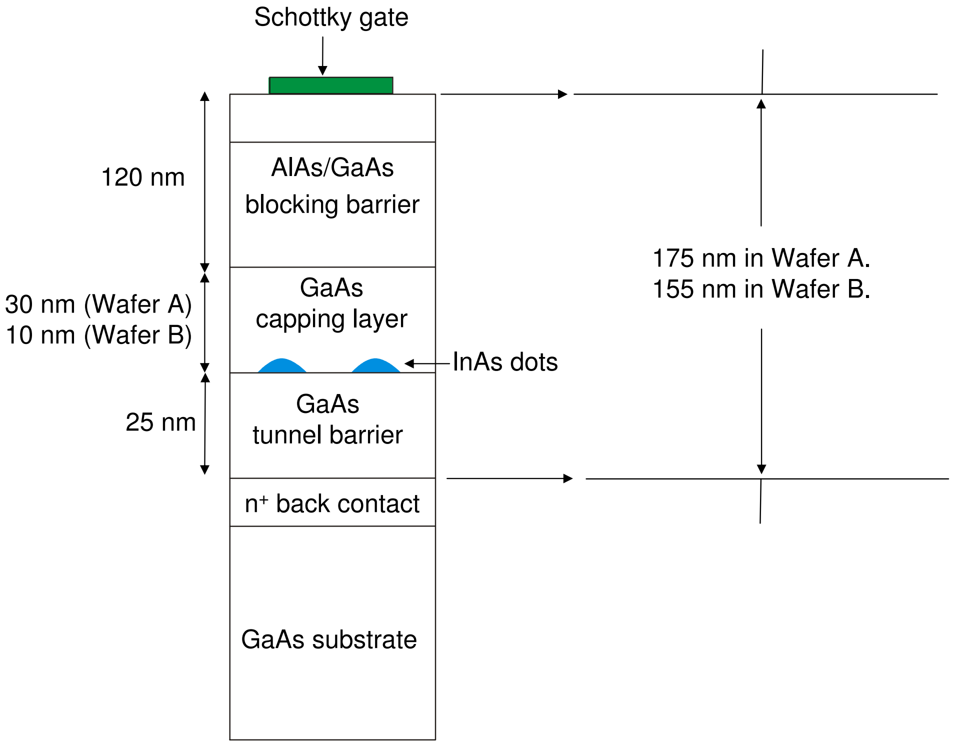

Figure 4.2: Side-view showing the sample layers in a cross-section of a charge-tunable device. Since the wafer structure does not permit current flow, the Schottky gate and back contact can be considered approximately as plates of a capacitor, with a GaAs dielectric. The relative thicknesses for the wafer structure are included.

4.1.2 Electronic properties

Successful samples show capacitor-like properties due to the wafer structure (Fig. 4.2). A voltage source provided as part of an EG & G Instruments 7265 lock-in amplifier was used to provide a sinusoidal oscillation (130 Hz, 10 mV amplitude) between the Schottky gate and the back contact of the sample constructed in section 4.1.1. The same lock-in was used to measure the real and imaginary parts of the current (I_R and I_I, respectively). I_R and I_I were measured as 0 nA and ∼20 nA respectively, giving a phase (θ) of 90°. When visible light is incident on a working sample I_R becomes non-zero and the phase lowers, showing the effects of photocurrent.

The phase of the real and imaginary parts of any complex impedance is given by

$$\tan\theta = \frac{\chi}{R}, \tag{4.1}$$

where R and χ are the resistance and the reactance, respectively. For the sample, a 90° phase confirms a capacitor-like reactance with $\chi \gg R$, the total current (I_{TOTAL})

is therefore

$$I_{TOTAL} = I_R + iI_I = \frac{V}{Z}, \tag{4.2}$$

where V is the voltage and $Z = R + i\chi$ is the impedance, therefore

$$I_{TOTAL} = \frac{V}{(R + i\chi)} \frac{(R - i\chi)}{(R - i\chi)} = \frac{VR - iV\chi}{\chi^2 + R^2}, \tag{4.3}$$

and taking the imaginary part,

$$I_I = \frac{V\chi}{\chi^2 + R^2}, \tag{4.4}$$

becomes

$$I_I = \frac{V}{\chi}, \tag{4.5}$$

where $\chi = \frac{1}{\omega C_S}$, and ω is the angular frequency. From this, the capacitance of the sample (C_S) can be calculated as ~2.4 nF. This can be compared with the capacitance expected from the device dimensions, given by

$$C_S = \frac{\varepsilon_0 \varepsilon_r A}{d}, \tag{4.6}$$

where ε_r is the relative permittivity of GaAs (12.85), A is the area of the Schottky gate (which has the same area as the keyhole-shaped shadow mask), and d is the distance between the Schottky gate and the back contact (155 nm). This gives a value of ~3.0 nF, which is in good agreement with the value of ~2.4 nF calculated from I_I.

At very high frequency capacitance does not contribute significantly to the impedance of the sample (see Eqn. 4.5). In order to measure the sample resistance and inductance the circuit in Fig. 4.3 was constructed and a Agilent pulse pattern generator (PPG) was used to apply a 100 mV amplitude step function voltage signal (~1 ns rise time) to the device (Fig. 4.4, black) at a repetition frequency of 147 kHz, at room temperature.

The sample response was measured by the oscilloscope, as shown in Fig. 4.4(red). At t=0 the sample response shows a voltage rise time of ~1 ns, approximately the same as the applied pulse (Fig.4.4, black). This confirms that the sample has no significant inductance, which would appear as an exponential rise time in the sample response at t=0. It is therefore a reasonable first assumption to consider the sample as electrically equivalent to a simple RC circuit.

Considering the oscilloscope nominal impedance as a resistor in a circuit with multiple resistors and a single capacitor (Fig. 4.3), any step function voltage applied across the circuit at time zero ($V_{applied}$) will initially only exhibit a voltage drop across the resistors. The voltage across the resistors will then fall exponentially as the

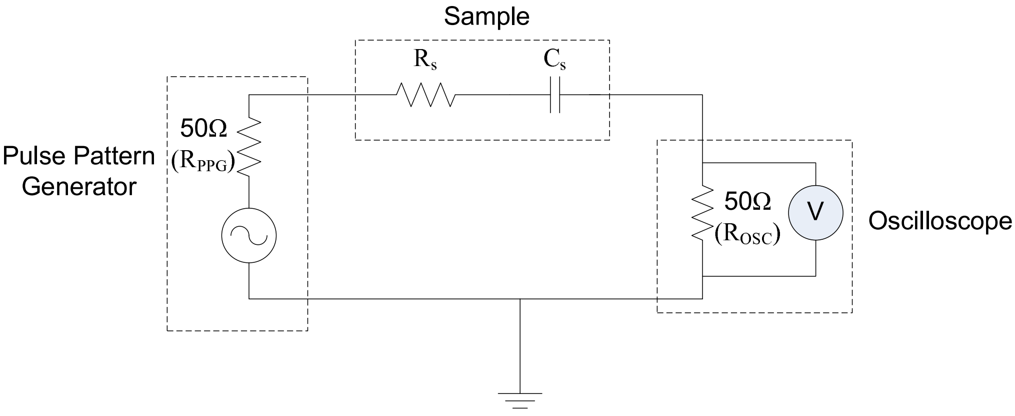

Figure 4.3: Equivalent circuit diagram of the original macroscopic sample when connected to the PPG and fast oscilloscope, showing internal/nominal impedances. The inner coax from the PPG is connected to the Schottky gate of the sample, and the inner of the oscilloscope is connected to the Ohmic contact, the outer (ground) coax from the PPG and oscilloscope are connected together. The sample is shown in a first assumption as a simple RC circuit, with R_s and C_s. The total resistance of the circuit (R_{total}) includes R_s, the 50Ω internal impedance of the PPG (R_{PPG}), plus the 50Ω nominal impedance of the oscilloscope (R_{OSC}).

capacitor charges, with a characteristic time of $R_{total}C_s$. The peak height of the decay at t=0 (V_{peak}) in Fig. 4.4(red) can therefore give an indication of the sample resistance (R_s), with

$$V_{peak} = \frac{V_{applied}R_{OSC}}{R_{total}}, \tag{4.7}$$

where the total resistance of the circuit (R_{total}) is

$$R_{total} = R_s + R_{PPG} + R_{OSC}, \tag{4.8}$$

where $R_{PPG} = 50\ \Omega$ is the internal impedance of the PPG, and $R_{OSC} = 50\ \Omega$ is the nominal impedance of the oscilloscope. A value of R_s=185 Ω was calculated from the peak height measured in Fig. 4.4(red). The same test was performed replacing the sample with a RC series circuit of known values (R=150 Ω and C=1 nF, Fig. 4.4(blue)) and the R_s value found was 164 Ω. This indicates that the value found by this test is likely to be higher than the real value by ~10 %, due to the finite rise time of the voltage pulse applied by the PPG at t=0. The value of R_s for the sample is therefore ~168 Ω.

A reasonable first assumption is that the sample will respond like a simple RC series circuit. The capacitance (C_S) was calculated to be between ~2.4 ns and ~3.0 ns (using equations 4.5 and 4.6), and the resistance was measured to be ~168 Ω (from equation 4.7 and Fig. 4.4), giving an RC constant of ~720 ns. Therefore the voltage measured across R_{OSC} in Fig.4.4(red) would be expected to show a single

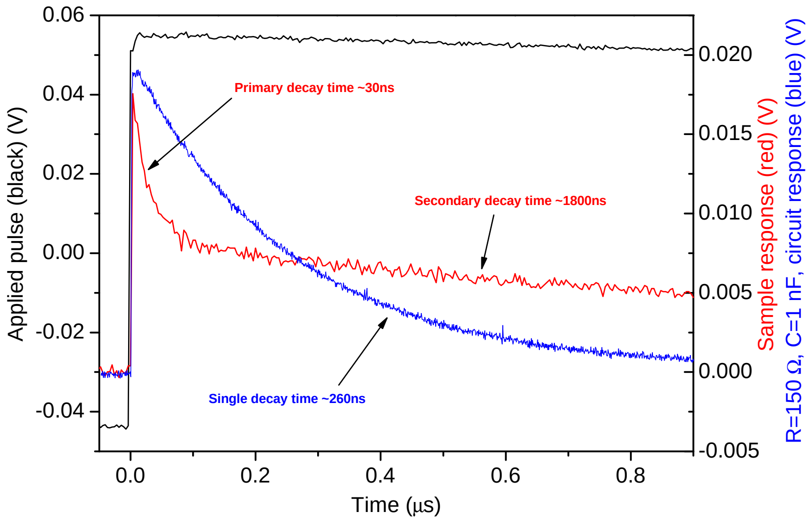

Figure 4.4: The voltage pulse applied over the device by the PPG (black), alongside the sample time response shown on the oscilloscope (red). The voltage pulse shape was measured by connecting the PPG directly to the oscilloscope. Two decays are clearly seen here in the sample response. Also included is the response of a series RC circuit (R=150 Ω and C=1 nF) to the same voltage pulse (blue). The RC circuit response shows a single lifetime.

exponential decay curve with a lifetime of ∼720 ns. However, the voltage response in Fig. 4.4(red) gives two distinct lifetimes (30 ns and 1800 ns). For the same applied voltage, the RC series circuit of known values (R=150 Ω and C=1 nF) gives a single exponential decay with a lifetime of 260 ns (Fig. 4.4, blue). This is slightly larger than the expected RC constant (250 ns), probably because of a lack of impedance matching. Since the sample responds to an applied voltage with two lifetimes, and the RC series circuit responds with only one lifetime, the sample cannot be considered electrically equivalent to an RC series circuit.

Other attempts have been made at constructing an equivalent circuit for a charge tunable device (Fig. 4.5, Equivalent circuit 1 [5] and Equivalent circuit 2 [6]), suggesting that the sample responds as a capacitor (C_{low} in [5], C_2 in [6]) at low frequencies, and a combination of two capacitors at high frequencies (C_{low} and C_{tunn} in [5], C_2 and C_1 in [6]). These models have merit, in that from Ref. [5] and [6] C_{low} is calculated to be 3.6 nF for Wafer B (050328B), which is reasonably close to the value of C_s (=3.0 nF) calculated in Eqn. 4.6. However, if either equivalent circuit were used to replace the sample from Fig. 4.3 (as shown in Fig. 4.5) and a 100 mV amplitude step function voltage signal was applied by the PPG (as in Fig.4.4, black), the voltage recorded across R_{OSC} would experience an initial exponential decay time (τ_{decay}) given by

$$\tau_{decay} = R_{total}C_{total}, \tag{4.9}$$

where C_{total} is calculated using

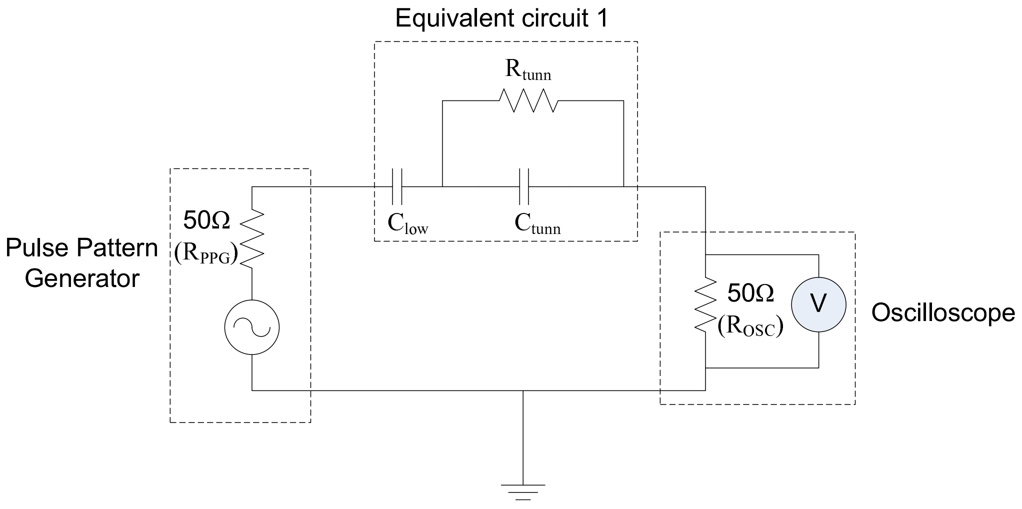

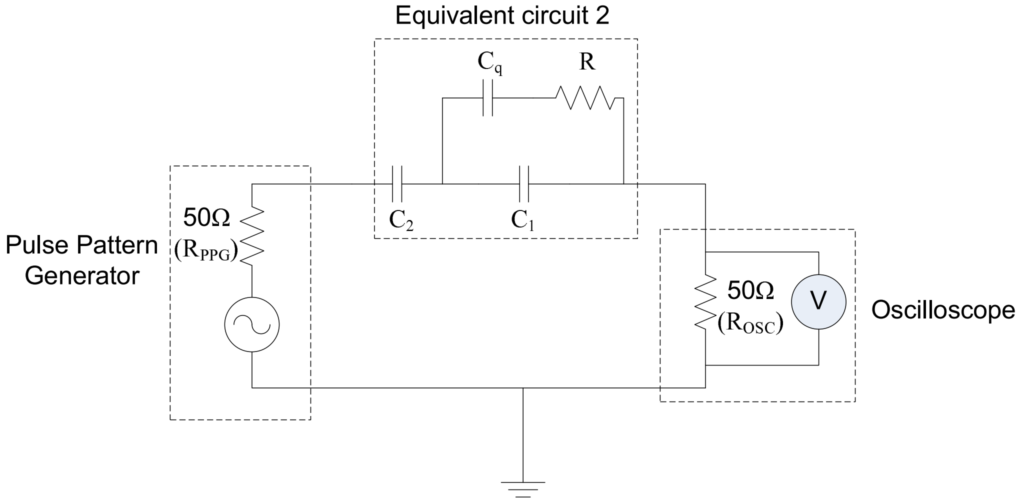

Figure 4.5: (Top) Equivalent circuit (1) of the sample as proposed by Medeiros-Ribeiro *et al.* [5], when connected to the PPG and fast oscilloscope in the same fashion as Fig. 4.3. (Bottom) Equivalent circuit (2) of the sample as proposed by Luyken *et al.* [6], when connected to the PPG and fast oscilloscope in the same fashion as Fig. 4.3. In both cases the inner coax from the PPG is connected to the Schottky gate of the sample, and the inner of the oscilloscope is connected to the Ohmic contact, the outer (ground) coax from the PPG and oscilloscope are connected together.

$$\frac{1}{C_{total}} = \frac{1}{C_{low}} + \frac{1}{C_{tunn}}, \tag{4.10}$$

where C_{low}=3.6 nF, C_{tunn} =18.9 nF (calculated from the device dimensions of Wafer B), and R_{total}=100 Ω (simply the sum of R_{OSC} and R_{PPG}). The initial decay time would therefore be τ_{decay}=302 ns, which is far larger than the primary decay time of 30 ns observed in Fig.4.4(red). Hence the equivalent circuits proposed in Ref. [5] and Ref. [6] do not compare well with the measured data.

Regardless of the exact construction of an electrically equivalent circuit, it is the overall time response of the sample to an applied voltage which is the most important concern with regards to the application of GHz pulses to a quantum dot. The time response measured in Fig.4.4(red), taken simply as the time taken for the voltage to reach $1/e$ of the peak height, was measured as ∼130 ns, which is too large to allow dot charging on the timescale of exciton recombination (∼1 ns, see Chapter 3, section 3.3). For this reason, the device design was altered in order that the voltage response time of the device was reduced.

4.2 The new microscopic samples

In order to reduce the overall time response of the device the design and construction were both altered considerably. Ideally both the resistance and the capacitance properties were to be reduced. It was decided that a photolithographically constructed device was the best way to achieve this.

4.2.1 Basic requirements

There are several prerequisites when considering how to change the device design and construction. The Ohmic contact and Schottky gate need to be changed in order to minimise the RC constant. Stray capacitances in both the sample and the electrical contacts to the sample need to be minimised. Lastly, we need to take into account the wish to use a s-SIL.

Ohmic contact

Low resistance Ohmic contacts are necessary in order to help reduce the overall resistance of the sample. The Ohmic contacts should be preferably positioned close to the Schottky gate, as there is a lower resistance in the metal of the Ohmic contact than in the back contact [4]. Ideally, the contacts should be planar to the sample and less than 1 μm thick in order to allow the correct placement of a s-SIL and the collection of large angle PL rays, without any thin film interference effects. Indium cubes were not suitable given these requirements, and with only 50 % success rate they were also not reliable enough.

Schottky gate

The main requirement for the Schottky gate is to be small, in order to reduce the capacitance of the system (down from ∼3 nF in the macroscopic samples). Ideally, the Schottky gate area should be reduced by at least three orders of magnitude, because as the smallest of the capacitor plates in the system it must also be the defining point for the capacitance. Also, the gate must be semi-transparent, but provide a good electrical contact over the entire surface.

Etch

The sample has to be etched for two reasons. Firstly, by destroying unneeded portions of the back contact it is possible to reduce any stray capacitance. Secondly, by destroying the back contact in some regions it is possible to create a metal contact strip between the coaxial cabling and the Schottky gate, without adding significantly to the capacitance of the device.

Contact metallisation

A low resistance contact to the Schottky gate was needed, as the gate itself was to be placed underneath a S-SIL. The contact needs to be positioned in an etched area, so as not to add to the capacitance, and it also needs to be large enough to provide electrical access in a region that isn't covered by the S-SIL. Lastly, since it will be placed in an etched region, it needs to successfully traverse the etch step in order to contact the Schottky gate.

Immersion lenses

The sample should include alignment markers for both SILs and S-SILs. These markers are to be used in order to position the NAIL centrally over the Schottky gate.

4.2.2 GHz bandwidth device—Mark I

Shown in Fig. 4.6 is the first design for the fast device, created from a section of Wafer B (050328B). The Schottky gate is 5 nm thick NiCr deposited over a small (approximately 15 μm x 25 μm) area. An etch provides an area within which the contact metal does not add significantly to the capacitance, and alignment markers ensure that a SIL or S-SIL will be placed centrally over the Schottky gate. The Ohmic contacts are large and placed ∼2 mm from the etched GaAs. Increasing the distance between the Ohmic contacts and the Schottky gate is expected to result in a larger device resistance, since any electrical pulses will have to traverse a larger region of the back contact. However, Ohmic contacts placed at this distance from the S-SIL will be more easily contacted to the electrical cabling.

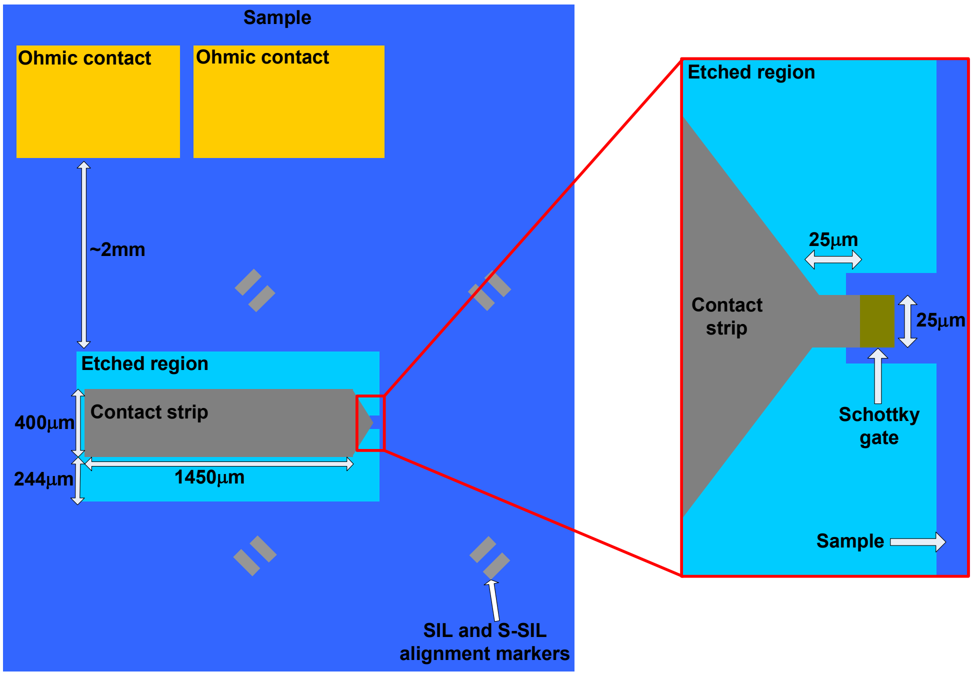

Figure 4.6: Diagram of the Mark I design for the fast device. Here, the Ohmic contacts are large and placed remotely from the Schottky gate and S-SIL position in order that the device may be contacted easily. The red box shows an enlarged view of the Schottky gate area. The relevant sizes are shown on both images.

Voltage time response measurement

Above all other considerations, the only concrete measure of success was the response time of a single quantum dot to an applied voltage. An optical experiment was performed at 4K using a single quantum dot (from Wafer B, 050328B) from a device (Device A) constructed as in Fig. 4.6, in order to measure the voltage time response. A single spatially and chromatically isolated dot was selected and excited with 550 nW μm^{-2} of 830 nm non-resonant CW laser light. The PL was recorded as a function of applied d.c. bias, as shown in Fig. 4.7. The neutral and charged excitons were identified as in Chapter 3 section 3.1.2. Two voltages were chosen to be ~10 mV further than each edge of the X^0 plateau, at which PL from X^0 is no longer likely to be observed (labelled as V_{high} and V_{low} in Fig. 4.7).

While the dot was being illuminated by 830 nm non-resonant CW laser light, the PPG was used to apply a 10 MHz repetition rate square wave voltage pulse oscillating between V_{high} and V_{low}. The PL was sequentially filtered for the X^{1+}, X^0 and X^{1-} wavelengths and TRPL was performed, the results shown in Fig. 4.8. At t=0 $V=V_{low}$ and PL from X^{1+} is observed (Fig. 4.8, black). At t=23 ns (chosen arbitrarily) the voltage changes from V_{low} to V_{high} (Fig. 4.8, purple), and PL from X^0 is observed for 12 ns (Fig. 4.8, red), and then as $V \rightarrow V_{high}$ PL from X^{1-} is observed (Fig. 4.8, blue). At 73 ns the voltage changes from V_{high} to V_{low}, and as $V \rightarrow V_{low}$ PL from X^0

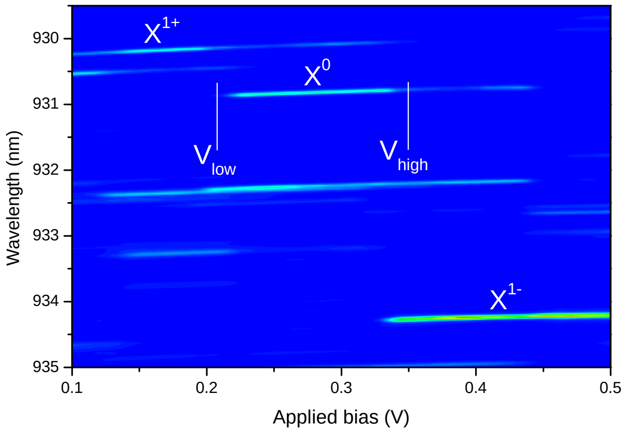

Figure 4.7: PL versus voltage bias for a single dot in Wafer B (050328B) which has been fabricated into a device (Device A) designed as in Fig. 4.6. Blue ≃150 counts, green ≃8000 counts, yellow ≃15000 counts, red ≃18000 counts or more. The dot is excited with 550 nW μm^{-2} of CW non-resonant 830 nm laser light, at a temperature of 4K. The PL due to recombination of X^{1+}, X^0 and X^{1-} have been identified. V_{low} (=208 mV) and V_{high} (=350 mV) are marked as points slightly lower and higher than the X^0 plateau extent.

is observed for 13 ns, then PL from X^{1+}.

The X^0 voltage extent shown in Fig. 4.7 is approximately 80% of the voltage difference between V_{high} and V_{low}. Furthermore, the X^0 voltage extent lies centrally between V_{high} and V_{low}. The full width at half maximum time over which PL from X^0 is recorded in Fig. 4.8(red) can be considered the time period within which the dot experiences a voltage bias which lies within the X^0 bias extent. From this it can be concluded that the sample has a 10-90% voltage response time of ∼13 ns.

This is a encouraging result, showing that a dot can be manipulated on a timescale of ∼13 ns, which is much closer to the timescale of exciton recombination (∼1 ns, see Chapter 3 section 3.3) than the measured response time of ∼130 ns shown by the original macroscopic design (see section 4.1.2). This device design is actually used in Chapter 5 section 5.1 to demonstrate dot charging on the timescale of the neutral exciton recombination lifetime. However, further potential improvements in the design were identified and implemented in order to achieve a GHz bandwidth voltage response.

4.2.3 GHz bandwidth device—Mark II

In section 4.2.2 the distance from Ohmic contacts to the Schottky gate was identified as a potential source of unwelcome resistance. Shown in Fig. 4.9 is the second device design in which the Ohmic contact was placed ∼10 μm from the Schottky gate.

The Ohmic contact, etch, and contact strip in this orientation on the GaAs sub-

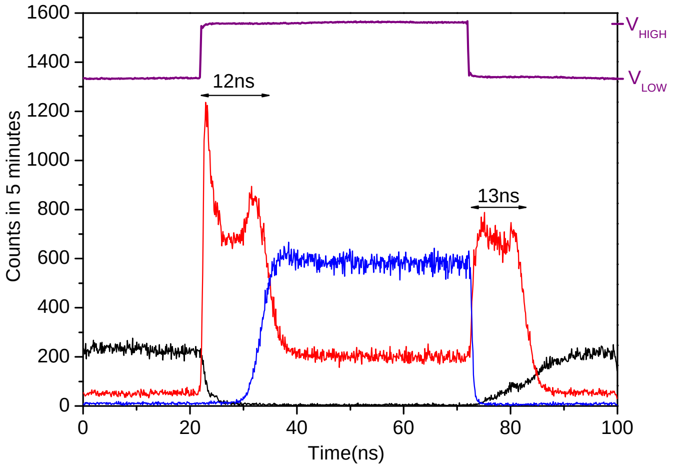

Figure 4.8: TRPL of X^{1+} (black), X^0 (red) and X^{1-} (blue) emission relative to a 10MHz square wave voltage pulse from the PPG (purple), changing between V_{high} and V_{low} as defined in Fig. 4.7.

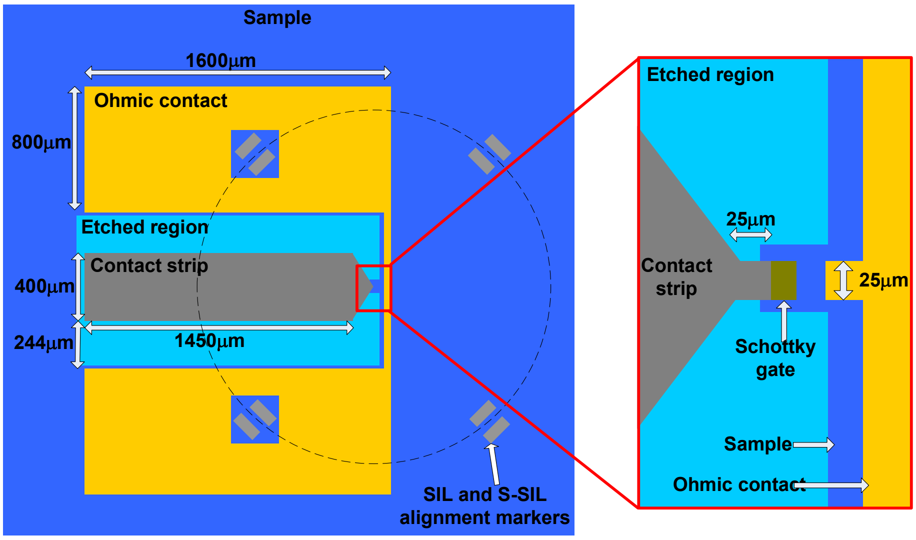

Figure 4.9: Diagram of the Mark II design for the fast device. Here, the Ohmic contacts are placed ∼10 μm from the Schottky gate in order that the device resistance is minimised. The red box shows an enlarged view of the Schottky gate area. The relevant sizes are shown on both images.

strate form a co-planar waveguide which is impedance matched to the 50 Ω impedance of the fast coaxial cabling from the PPG. The appropriate widths of the Ohmic contact, etch, and contact strip were calculated using Ref. [7].

10-90% voltage time response measurement

In the same method as in section 4.2.2, a measurement of the voltage response time was performed using a single dot in Wafer B in a device (Device B) designed as shown in Fig. 4.9. A single dot was selected and excited with 270 nW μm^{-2} of 830 nm non-resonant CW laser light. Two voltages (V_{high} and V_{low}) were positioned ∼10 mV beyond either edge of the X^{1-} plateau (In section 4.2.2 V_{high} and V_{low} were positioned either side of the X^0 plateau, this is an arbitrary choice which gives the same result). The PPG was used to apply a 10 MHz square wave voltage pulse, changing between V_{high} and V_{low}. In this way, the only time the dot was capable of forming X^{1-} was when the bias experienced by the dot was within the X^{1-} extent.

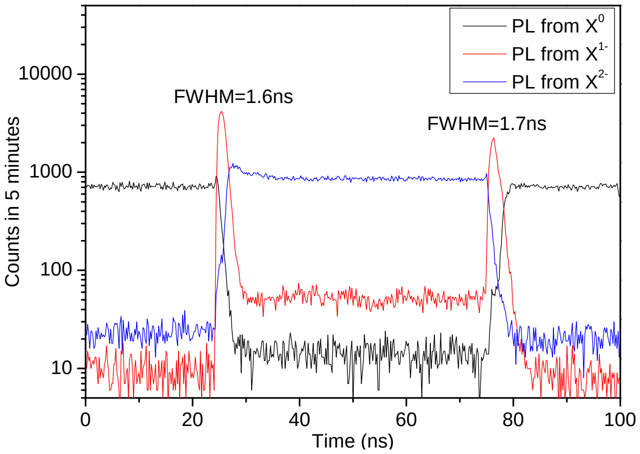

Figure 4.10: TRPL of X^0, X^{1-} and X^{2-} emission relative to a 10 MHz square wave voltage pulse from the PPG, changing between V_{high} and V_{low}. The experimental setup is the same as that for Fig. 4.8.

TCSPC was performed sequentially on the emission due to X^0, X^{1-} and X^{2-}, and the results are presented in Fig. 4.10. The FWHM of the PL peak from X^{1-} at t=23 ns and t=73 ns is significantly shorter than the FWHM of the PL peak from X^0 at the same times in Fig. 4.8, giving a 10-90% voltage response time of ∼1.6 ns for the new device. The jitter of the SPAD (∼400 ps) does not significantly alter this value.

Secondary method for measuring the voltage time response

A second method for measuring the response of a single dot to an applied voltage was tested using the same dot as in Fig. 4.10. In this method, the voltage extent over which X^{1-} PL is emitted (∼130 mV) is used as a probe for a voltage pulse with an amplitude of 200 mV. In order to achieve this, the dot was excited non-resonantly with 270 nW μm^{-2} of 830 nm CW laser light. A square voltage pulse was applied to the sample by the PPG. During the voltage pulse (pulse width Δt) the upper voltage (V$_{high}$) was applied by the PPG, and at all other times the lower voltage (V$_{low}$) was applied by the PPG. The voltage difference between the upper and lower voltages (V$_{high}$ - V$_{low}$, the pulse amplitude) was kept constant at 200 mV. The voltage pulse repetition rate was kept constant at 20 MHz.

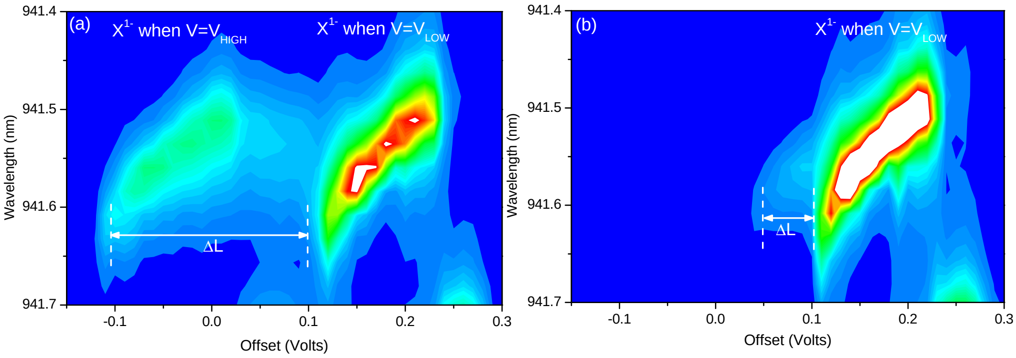

Figure 4.11: X^{1-} PL versus offset voltage recorded while exciting the sample with 270 nW μm^{-2} of 830 nm CW laser light. A 20 MHz repetition rate voltage pulse (V$_{high}$) is applied to the device by the PPG for (a)10 ns and (b) 0.5 ns. At all other times the device is biased at V$_{low}$.

In Fig. 4.11(a) PL was recorded from X^{1-} as the voltage offset (the mean voltage of V$_{high}$ and V$_{low}$) was varied, for a pulse duration Δt=10 ns. PL from X^{1-} was recorded at two separate voltage offset extents. At lower voltage offsets (-0.1 V to 0.02 V) X^{1-} PL is recorded because V$_{high}$ is at a bias which allows X^{1-} to form and recombine, and at higher voltage offsets (0.1 V to 0.23 V) X^{1-} PL is recorded because V$_{low}$ is at a bias which allows X^{1-} to form and recombine. The count rate of the X^{1-} PL recorded at lower bias offset was approximately five times lower because the time spent in V$_{high}$ is 5 times less than the time spent in V$_{low}$. The voltage difference between the onset of the X^{1-} PL extent at lower and higher offsets (ΔL) is $\sim$200 mV, as would be expected for an impedance matched system.

In Fig. 4.11(b) Δt is changed to 0.5 ns, and the X^{1-} PL is recorded against voltage offset in the same fashion as in Fig. 4.11(a). In this case, ΔL has become much reduced, at $\sim$70 mV. This is because the dot takes a finite time to experience a change from V$_{low}$ to V$_{high}$, approximately $\sim$1.6 ns as already measured. This can be explained by Fig. 4.12 which shows a representation of the voltage experienced by a dot with a 1 ns exponential response time. As Δt becomes shorter, the peak voltage reached (otherwise known as the the effective amplitude of the pulse, ΔL) becomes smaller.

This property was successfully used to measure the shape of the voltage change experienced by the dot (ΔL) as it changes over time (Δt). Several plots of PL against voltage offset were recorded in same fashion as in Fig. 4.11, for several values of Δt.

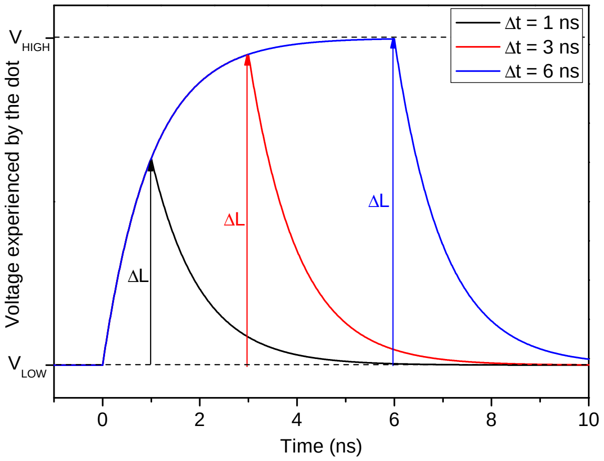

Figure 4.12: A representation of the voltage experienced by the dot against time, for three different pulse lengths. In this representation, the dot is assumed to have an exponential response to any applied voltage, with a $\frac{1}{e}$ response time of 1 ns. Also, the applied pulse is assumed to have an instantaneous rise time, and the sample is assumed to have no inductance. For a pulse length much larger than the response time (Δt=6 ns, blue), the peak voltage experienced by the dot (ΔL, blue) is $\sim$V$_{high}$. As the pulse length is reduced (as in the red and black lines, Δt=3 ns and 1 ns respectively), the peak voltage experienced by the dot (ΔL) becomes smaller.

The value of ΔL was found for each value of Δt and plotted in Fig. 4.13. The data is fitted well by a single exponential with a $\frac{1}{e}$ rise time of 1.0 ns ±0.1 ns (Fig. 4.13, red).

An exponential dot voltage response $\frac{1}{e}$ time of 1.0 ns ±0.1 ns is equivalent to a 10-90% time of 2.2 ns ±0.2 ns, which is slightly larger than the 10-90% value of 1.6 ns found for the same dot using the previous method (Fig. 4.10). However, this confirms that a dot in the new device is capable of responding to an applied voltage with a GHz bandwidth, one of the major goals of this work. This style of device is used for many of the GHz bandwidth voltage pulsing experiments presented in Chapter 5.

4.3 The photolithography process

4.3.1 Spin coating and calibration

Spin coating machine

In order to apply photoresist to the sample a spin coating machine made by Cost Effective Equipment was used. It uses a vacuum to hold a standard 2” wafer onto a plastic chuck, and spins at various programmable speeds and accelerations in order to produce the desired photoresist coating. Calibration tests were performed to find the correct settings for a repeatable ∼1 μm thick resist coating.

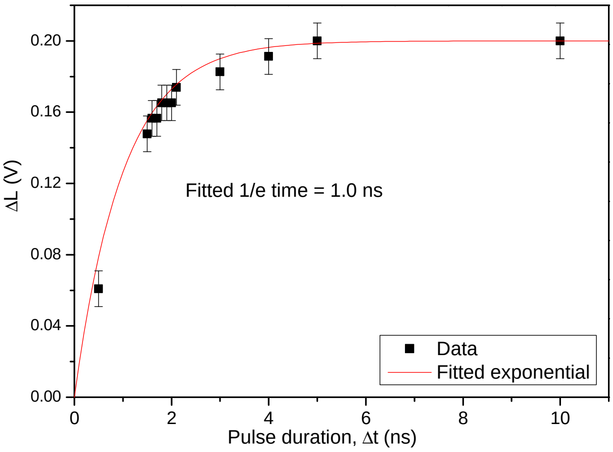

Figure 4.13: ΔL, measured from the X^{1-} PL as seen in Fig. 4.11, measured as a function of pulse length (Δt). The curve is fitted with an exponential, which gives the $\frac{1}{e}$ value of the dot voltage response time.

Sample holder

All devices were constructed on 4 mm x 4 mm square pieces of wafer material, and as such were incompatible with the spin coating machine chuck. A sample holder was constructed on a 2” glass wafer (Fig. 4.14). Various positions were tried, but the most uniform results were achieved when the sample was placed ∼1 cm from the edge of the wafer, and edge effects were minimised when the square sample was placed with one corner pointing towards the centre of the wafer (Fig. 4.14).

Placing the sample in the holder

The best results for spin coating were obtained when the edge intended for the electrically contactable edges of the Ohmic contact and contact metal was placed to be the trailing edge as the wafer is spinning (Fig. 4.14). First the sample and holder must be cleaned thoroughly with IPA and Acetone. Then a small amount of Dow Corning High vacuum grease was placed on the holder before placing the sample on top, in order to stop the sample falling off during spin coating. In order to secure the sample in the holder, two cotton tipped probes were used to press the sample into the vacuum grease until the sample was planar with the glass wafer. It is very important that the probes remain clean, and that no vacuum grease is transferred on to the top surface of the sample.

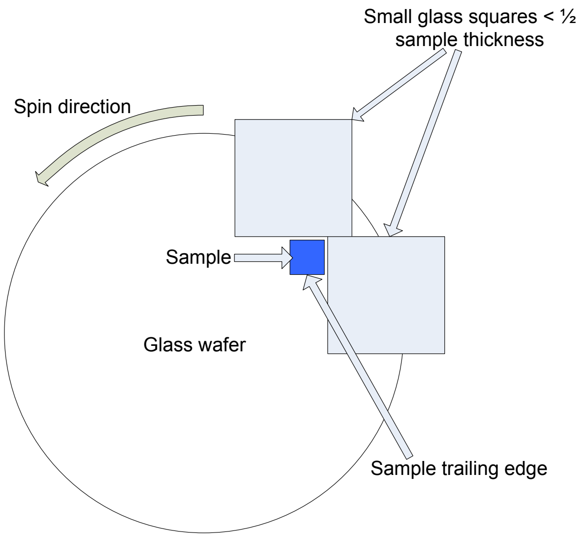

Figure 4.14: Sample position in the spin-coater holder. The glass squares used were 25 mm x 25 mm square cover glass (Thickness no. 1.5) from VWR International. The thickness of the cover glass is 0.16-0.19 mm, chosen to be thinner than the sample itself (0.5 mm) so that photoresist could run freely off the sample during spin coating.

Cleaning the sample in the holder

To test whether or not the sample is clean enough for spin coating, a small drop of acetone was placed onto the sample surface. If the sample is clean the acetone drop will sit unperturbed, otherwise the sample surface will be slightly hydrophobic, causing the acetone to avoid the dirtier surface area. To clean the sample: First rinse with flowing acetone, to remove any large particles. Then, put some acetone onto a cleaning cloth, and press the sample (in its holder) upside down into the cloth. The holder can then be dragged lightly along the cloth, always in a direction which allows the sample to move by being pushed by the cover glasses.

Spin tests

Calibration tests were performed to find the best spin speed, time and acceleration values. In order to measure the depth and consistency of any particular spin coat the sample was baked at 65° C for 2 minutes then 95° C for 5 minutes to remove any moisture. Then, a straight-edged piece of foil was lightly placed over half of the test sample, then illuminated with broadband UV light at a power of 2 mW/cm^2 for 200 seconds, and post-baked at 65° C for 2 minutes then 95° C for 5 minutes. The sample was then developed under flowing AZ developer and dried quickly with compressed Nitrogen gas. A Zygo white light interferometer was then used to measure the resist thickness and the surface fluctuations.

Choosing the photoresist

Two positive photoresist types were tested. The first was a Shipley S1805 resist from Chestech Ltd. The second was Microposit S1813. The Microposit resist was thicker ($\sim$1 μm compared to $\sim$500 nm for the Shipley using a spin of 300 rpm for 30 seconds accelerated from 0 rpm at 1000 rpm s^{-1}), and resulted in a more uniform surface. The process was standardised using 5 drops of resist to completely cover the device.

Edge beads and film fluctuations

Due to surface tension in the resist, beads of resist can form around the edge of the sample. This normally isn't a concern for standard wafers with a large 2" diameter, but with the small samples used for device fabrication in this project edge beads can easily be as large as 1 μm. An "edge-bead removal" spin was added to solve this problem. This additional spin step is performed at the end of the thickness determining spin, when the resist has started to settle at a specific thickness. The edge-bead removal spin is a fast acceleration spin which lasts a very short time. This was set to be 3000 rpm accelerated from 300 rpm at 6000 rpm s^{-1} for 1 second.

Final preparation method

After positioning the sample in the holder, and placing the holder in the spin coating machine. The sample was covered with 5 drops of S1813 photoresist and spun at:

300 rpm accelerated at 1000 rpm s^{-1} from standstill for 30 seconds,
then...
3000 rpm accelerated at 6000 rpm s^{-1} for 1 second.

Finally, the sample was baked at 65° C for 2 minutes then 95° C for 5 minutes, giving a final resist thickness of 800 nm-1μm with only small edge effects.

4.3.2 Alignment and patterning

Mask aligner

A Tamarack 152 mask aligner was used to perform the UV patterning, allowing sample adjustments of $\sim$3 μm relative to the photomask, and allowing UV energy exposures accurate to $\pm$1 mJ cm^{-2}. The aligner functions by using four pneumatic pistons to create a variable air gap between the mask and the sample. In the standard setup the pistons did not have sufficient range of motion to create an air gap between the sample and the mask. 1 mm thick stainless steel plates were designed in order to raise each of the four pistons in order to re-create the air gap for our setup.

Mask

A 5” x 5” chrome-on-glass photomask was made by Compugraphics, with a pattern which was accurate to within 1 μm. In order to use the mask with the mask aligner an adapter plate[1] was used. The mask was taped into the adapter to make a flush finish, allowing the mask to be held by the mask aligner vacuum seals, which were designed for use with 7” x 7” photomasks.

Two methods of alignment were designed into the photomask. In the first, alignment targets were included in every section of the mask containing 1, 2, 5 and 10 μm features which could interlink with the other patterning stages. In the second, the transparent sections of the mask could be used used for basic alignment, though with a slightly reduced accuracy of ± 3 μm.

Alignment sample holder

It was determined that a separate sample holder was required for patterning in the mask aligner than the one used for spin coating. There were two reasons for this. Firstly, the range of motion of the mask relative to the sample does not allow the sample to be patterned with all of the potential fabrication steps. Secondly, patterning the sample involves resting the photomask on top of the sample, which could place a large amount of weight unevenly over the sample surface. It was not uncommon for samples that were imperfectly cleaved to shatter under any kind of stress.

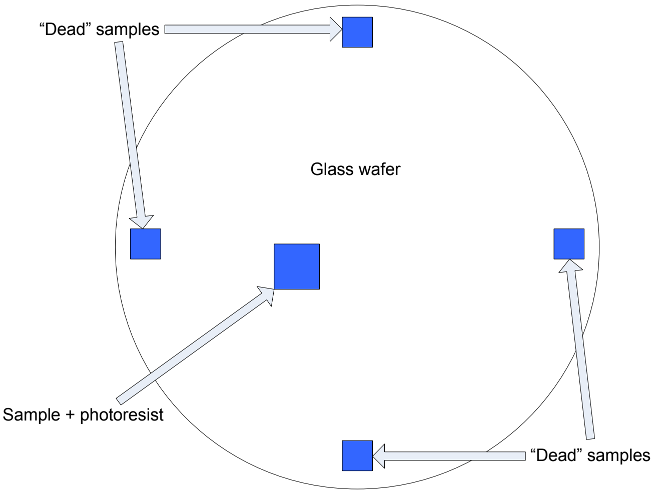

Figure 4.15: The sample position in the alignment sample holder, for use in the mask aligner. The patterned sample was held to a glass 2” wafer with vacuum grease at a position which allowed the relevant photomask section to be used. Four unusable “dead” pieces of wafer material were fixed to the edges of the wafer in order to take the weight of the photomask and to ensure the mask was planar to the sample.

---

[1] made and fitted by Mark Leonard

Fig. 4.15 shows the sample holder that was constructed specifically for use with sample patterning. The main body of the holder was a glass 3” wafer, on top of which the sample could be positioned and held with a small amount of vacuum grease. At four points of the edge of the wafer were placed unneeded pieces of semiconductor material of the same thickness as the wafer to be patterned, held with Oxford GE varnish. The material was included in order to take the weight of the photomask whilst keeping it planar to the sample.

Patterning

Due to the resolution needed it was necessary to use contact printing, but in order to avoid overstressing the sample soft contact printing was used, in which the mask is held onto the sample by gravity.

Once the mask has been positioned correctly, the resist is exposed to 500 mJ cm^{-2} of UV light in ∼14.9 seconds for every single layer of photoresist applied. The light used was filtered in order to allow only the 365 nm peak line from a mercury lamp to propagate to the sample.

After exposure, the sample is baked at 65° C for 2 minutes then 95° C for 5 minutes in order to ensure the borders between exposed and non-exposed areas are well defined.

The pattern was then developed with a 1:3 parts AZ developer to water solution. The sample was removed from the alignment holder and most of the vacuum grease was carefully cleaned off using cotton tipped probes. The sample was then held with plastic-tipped tweezers underneath flowing developer solution, then underneath deionized water. The sample cannot be developed using traditional methods because residual vacuum grease can find its way to the top surface and destroy the pattern. After the pattern emerges the sample top surface was dried with compressed nitrogen gas, and the bottom surface was dried with a cleaning cloth.

4.3.3 E-beam evaporation and the film thickness monitor (FTM)

An Airco Inc. electron beam evaporation chamber was used to evaporate metals onto the surface of the patterned samples. Shown in Fig. 4.16, the sample is held upside down by vacuum grease on a glass wafer placed in a carousel. The metal to be evaporated is placed in a crucible directly underneath the sample. The chamber is then then pumped down to ∼4x10^{-6} mbar in order to prevent air particles interfering with the electron beam. Using a current of ∼25 mA the electrons are directed using electromagnets onto the metal surface, causing fast spot heating and evaporation. A portion of the evaporated metal travels upwards to then resolidify on the sample/resist surface. The main disadvantage to this method is that much of the metal evaporated is wasted, which can be expensive when gold alloys are used.

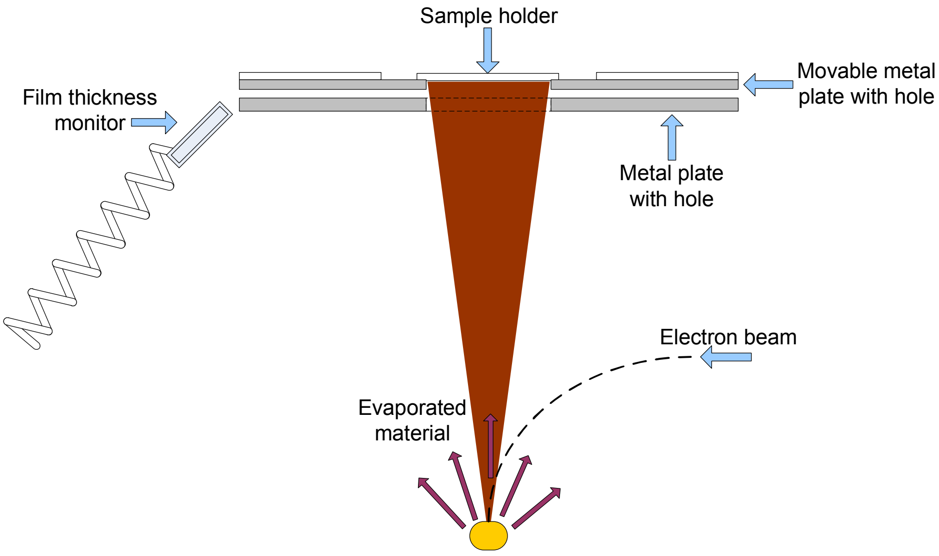

Figure 4.16: Schematic showing the position of the sample while held in the e-beam vacuum chamber. The sample is held upside down on a glass wafer, placed in a large rotatable metal plate. The plate can then spin in/out of alignment with a secondary plate with a single wafer-sized hole. In this way, the sample can be shielded from exposure to any evaporated metal. A film thickness monitor allows an accurate measurement of the evaporation rate.

Crucible choice

The choice of crucible is important because different metal alloys diffuse differently through different crucible materials. The 2 crucible types were: an Alumina short bowl-shaped crucible (LR19) from Almath Crucibles Ltd. for Ni, and graphite (Fabmate EVCFABEB-4) from Kurt J. Lesker Company Ltd. for Au, AuGe and NiCr. It is important not to allow the electron beam to hit the alumina crucible because it has a tendency to explode.

Addition of a film thickness monitor (FTM)

A SF-290 FTM constructed with a $2\frac{3}{4}$" Conflat flange was purchased from Testbourne Ltd., and mounted into the e-beam evaporation chamber. The FTM was mounted at the same distance to the metal as the sample. When calibrated correctly, thickness changes of $\sim$0.1 nm can be successfully measured.

4.3.4 Lift-off

Once the metal has been successfully evaporated over the sample/resist combination the photoresist is removed, removing the metal above the resist, leaving the original pattern from the mask.

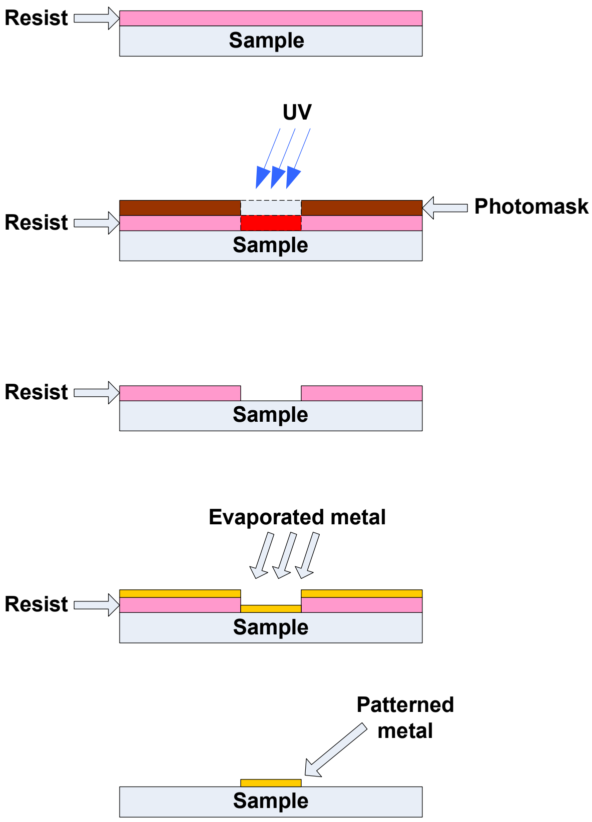

Figure 4.17: Diagram of the patterning and lift off procedure. From the top: The sample is first coated with a layer of positive photoresist. Selected parts of the photoresist are exposed to UV light through a photomask, changing the chemical properties of the resist. The sample is developed with AZ developer, which dissolves any exposed resist. Metal is evaporated over the entire sample/resist surface. Acetone is used to remove the remaining resist, which also removes any metal above it. What remains is a metal pattern of the same pattern as the transparent portions of the photomask.

To perform the lift-off (shown in Fig. 4.17), the sample was first removed from the glass wafer used for evaporation, and cotton tip probes were used to carefully remove the vacuum grease from the underside. Then, the sample was immersed in an acetone ultrasonic bath (a USC300D ultrasonic cleaner from VWR) upside down on full power for ~1 second in order to help break up the metal structure over the resist. After this, the sample was held under running acetone until the unwanted metal and photoresist are completely removed. Lastly, the sample is held underneath running IPA and then dried quickly with compressed nitrogen to avoid any evaporation-based acetone “water marks”.

4.3.5 Ohmic contacts and annealing

AuGe and Ni layers were chosen in order to make Ohmic contacts[2]. Immediately prior to evaporation of the Ohmic contact onto the sample surface using the e-beam, the sample was placed in a 10 % hydrogen- 90 % nitrogen-atmosphere (within a Biorad alloying furnace, unheated) and the top surface of the sample was exposed to trace amounts of sulphuric acid vapour. This served two purposes, firstly as a cleaning action, and secondly to inhomogenise the top surface to provide anchor points for the evaporated first AuGe layer. Then, prior to evaporation, the sample was heated to 105° C for 5 minutes on a hot plate in order to remove any moisture present on the sample surface, again to allow the gold to stick to the surface more easily [8].

The layers evaporated for the Ohmic contact are as follows...

Layer	**Material**	**Thickness**
First	Au(88 %)Ge(12 %) Eutectic	60 nm
Second	Ni	10 nm
Third	Au(88 %)Ge(12 %) Eutectic	60 nm

The first AuGe layer provided Ge as a dopant when annealed through the sample surface [9, 10]. The Ni layer was included to try and minimise balling on the surface (Shown in Fig.4.18), a common problem when AuGe is annealed [9, 10, 11]. The second AuGe layer was included to provide more carriers, to ensure a good surface uniformity despite small amounts of balling, and also to form a low resistance layer for contact to the high speed cabling [9].

After lift off the sample was annealed using a BIORAD alloying furnace in a Hydrogen(10 %): Nitrogen(90 %) atmosphere. First the sample was heated to 110° C for 5 minutes in order to remove any moisture, then 360° C for 2 minutes to melt the AuGe, and finally 420° C for 30 seconds in which time the Ge propogates through the sample, locally doping the wafer between the surface to the back contact (a more detailed explanation can be found in Ref. [11] and Ref. [12]). A successful anneal will

---

[2] based on a recommendation by Stefan Seidl, LMU

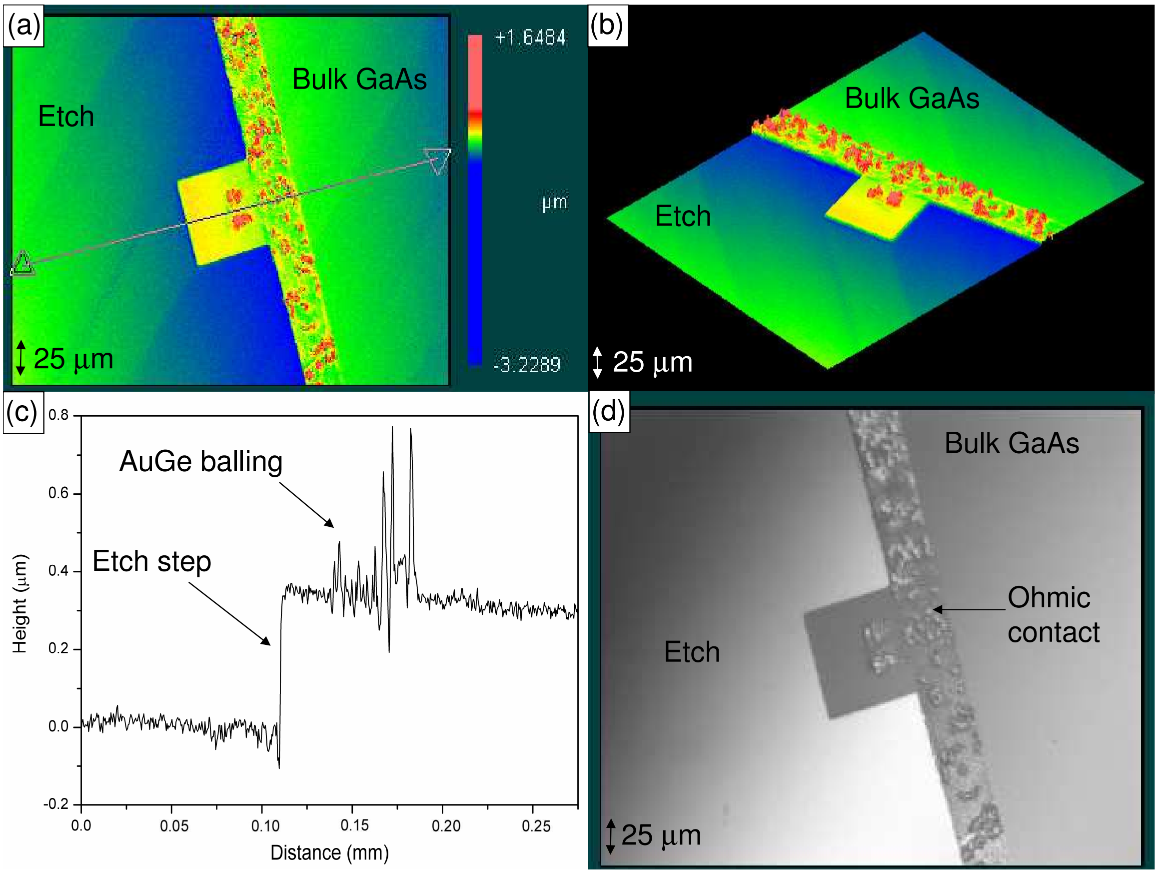

Figure 4.18: Images taken with a Zygo white light interferometer of a partially constructed device in which the Ohmic contacts have been deposited and annealed, and a ∼400 nm wet etch has been performed. The device has an Ohmic contact which shows a significant "balling" effect in which portions of the annealed AuGe have preferentially settled in the same regions, forming irregular lumps which can be up to several hundred nanometers high. (a) shows a plan view computer-generated image of the device with colour-based height information. (b) shows a 3D image computer-generated image created from (a). (c) shows the height information from a single strip from (a), indicated by the line in (a). (d) shows a black and white microscope image of the device.

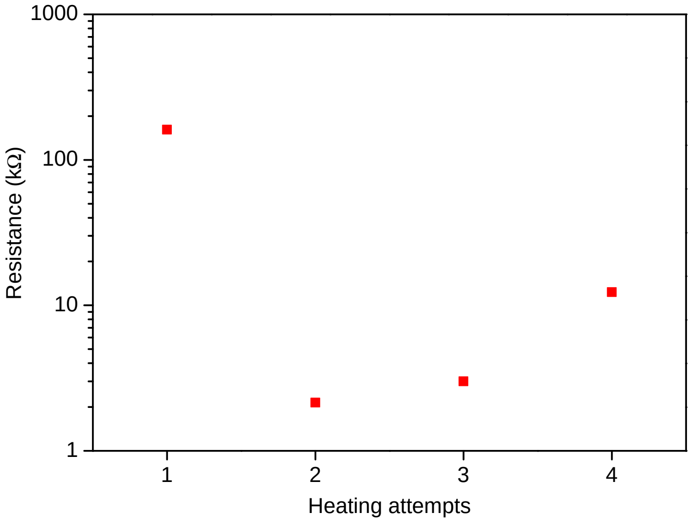

Figure 4.19: The resistance between two Ohmic contacts on the same sample from Wafer B (050328B), against successive annealing attempts. This was performed using an e-beam evaporated Ohmic contact consisting of Ni/ AuGe/ Ni/ Au in thicknesses of 15 nm/250 nm/15 nm/350 nm. Each heating attempt consisted of heating the sample to 110° C for 5 minutes, 360° C for 2 minutes, then 420° C for 30 seconds.

show <1 kΩ resistance between separate annealled areas. A typical value is around 200-300 Ω, which was on average half the resistance of the indium Ohmic contacts.

The Ohmic recipe used had a 100 % success rate with over 20 samples annealled. Also, the resistance did not seem to be affected by over-annealling [9], which is a process whereby over-diffusion of the Ge causes the resistance of the Ohmic contact to increase with further heating. Over annealling was however observed with another Ohmic contact recipe (Fig. 4.19), which consisted of Ni/ AuGe/ Ni/ Au in thicknesses of 15 nm/250 nm/15 nm/350 nm. In this case overannealling possibly occured because a thick (>50 nm) layer of Au was included in the layer structure [13]. It is important to be aware that alloying temperatures and times can have a large effect on the conductivity of the Ohmic contacts [14].

4.3.6 Etch

A sulphuric acid-based wet etch was used to destroy the back contact in selected regions. The acid was mixed in the ratio 1:8:200 of H_2SO_4:H_2O_2:H_2O, giving an etch rate in GaAs of 2.5 nm s^{-1} ± 0.1 nm s^{-1} at room temperature and pressure.

The acid solution was stirred at 5-8 Hz with a magnetic stirring bar, and the patterned sample was held in the solution for 2.5 minutes with plastic tipped tweezers, giving an etch depth of 360-400 nm on the areas of the sample not covered by photoresist. On removal from the solution the sample was immediately washed with deionized water in order to stop the reaction. Acetone was then used to remove the remaining photoresist.

4.3.7 Schottky gate

The Schottky gate was formed by evaporating NiCr eutectic. The NiCr wire purchased from Goodfellows was pre-melted into its crucible before evaporation using the electron beam. 5 nm NiCr was deposited at a rate of 0.1 nm s^{-1} using an e-beam current of ~15 mA.

4.3.8 Contact strip and NAIL alignment markers

NiCr eutectic was used to form the contact strip and the NAIL alignment markers. Au and Ti were also tested for this use, however Au would flake away from the sample easily (similar problems have been observed with Au adhesion to glass [15]), and Ti would stick to itself and the sample with such success that lift-off methods were unsuccessful.

In order to keep the resistance of the contact strip low, a 360 nm-thick layer of NiCr ($1.1\text{x}10^{-6}$ Ωm at room temperature) was evaporated. Since the contact strip needed to overcome the step formed between the etched and unetched material the sample was held at 45° to the evaporating metal using a small piece of rubber cut to the correct angle and glued to a glass plate. NAIL markers were included at this stage because a thick layer of metal would easily be seen under a microscope.

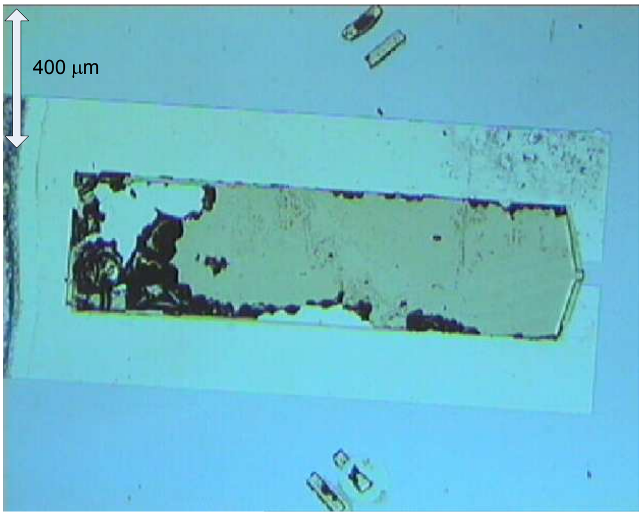

Figure 4.20: Microscope photo of a device NiCr contact strip with clear rippling effects. At the left edge, the thick contact strip is degrading, and will eventually disappear completely. This effect only happens with the thick contact strip, and not the Schottky gate.

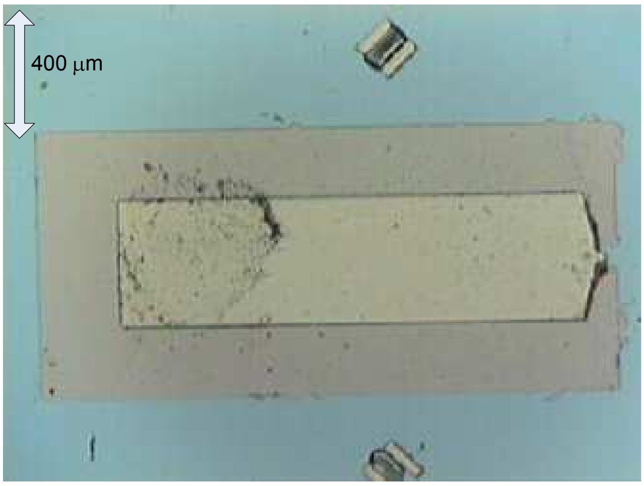

Figure 4.21: Microscope photo of a successful device NiCr contact strip with no rippling effects.

In order to evaporate 360 nm of NiCr normal to the sample surface, 495 nm was evaporated with the sample held at a 45° angle to the evaporating metal. The evaporation rate was kept at ∼1 nm s^{-1} with 5 minute breaks every 100 nm in order that the sample would not be heated beyond ∼110° C [16]. This was done in order to try and prevent prevent adhesion (rippling and lift-off) problems that were seen with faster evaporation rates (See Fig. 4.20 and 4.21). This problem was unfortunately still observed with thermal cycling (repeated cooling of the device to 4 K and warming back to room temperature).

4.4 Contacting

In all cases, fast electronic cabling was contacted to the sample surface through a strain-relief system. Silver conductive paint purchased from RS was used to contact the wire to the sample surface. Ideally, wire bonding to the sample would give a better electrical connection. However, when wire bonding was attempted using a K & S model 4124 wire bonder, the wire was unable to attach to the NiCr contact strip on the device. This could be solved by using a contact strip which consists of a top layer of gold (see Chapter 6 section 6.2).

4.5 Conclusion

Two new sample designs were constructed using photolithography. The ability to apply nanosecond rise-time voltage pulses to a single dot in each design was measured, and it was found that one design was able to respond more quickly than the other by a factor of $\sim$8. In the faster design, it was shown that a dot can respond to any applied voltage with an exponential rise time of 1.0 ns, which is approximately the timescale of an exciton radiative recombination. Lastly, the processing steps for the creation of a GHz bandwidth device were discussed and standardised.

References

[1] R. J. Warburton, C. Schäflein, D. Haft, F. Bickel, A. Lorke, K. Karrai, J. M. Garcia, W. Schoenfeld and P. M. Petroff, *Optical emission from a charge-tunable quantum ring.* Nature, **405**, 926 (2000).

[2] M. Ediger, P.A. Dalgarno, J. M. Smith, B. D. Gerardot, R. J. Warburton, K. Karrai and P. M. Petroff, *Controlled generation of neutral, negatively-charged and positively-charged excitons in the same single quantum dot.* Applied Physics Letters, **86**, 211909 (2005).

[3] J. M. Smith, P. A. Dalgarno, R. J. Warburton, A. O. Govorov, K. Karrai, B. D. Gerardot and P. M. Petroff, *Voltage control of the spin dynamics of an exciton in a semiconductor quantum dot.* Physical Review Letters, **94**, 197402 (2005).

[4] E. H. Rhoderick, R. H. Williams, *Metal-Semiconductor Contacts.* Oxford Science Publications, Second Edition, p204, 1988.

[5] G. Medeiros-Ribeiro, J. M. Garcia and P. M. Petroff, *Charging dynamics of InAs self-assembled quantum dots.* Physical Review B, **56**, 3609 (1997).

[6] R. J. Luyken, A. Lorke, A. O. Govorov, J. P. Kotthaus, G. Medeiros-Ribeiro and P. M. Petroff, *The dynamics of tunneling into self-assembled InAs dots.* Applied Physics Letters, **74**, 2486 (1999).

[7] $http://www1.sphere.ne.jp/i-lab/ilab/tool/cpw\_e.htm$

[8] R. C. Williams and R. C. Backus, *The electron micrographic structure of shadow-cast films and surfaces.* Journal of Applied Physics, **20**, 98 (1949).

[9] H. C. Lin, S. Senanayake, K. Y. Cheng, M. Hong, J. R. Kwo, B. Yang and J. P. Mannaerts *Optimization of AuGe-Ni-Au contacts for GaAs MOSFETs.* IEEE Transactions on Electron Devices, **50**, 880 (2003).

[10] S. P. Morgan and D. V. Morgan, *Characterization of AuGe-based ohmic contacts to n-GaAs fabricated using ion-assisted deposition.* Semiconductor Science and Technology, **9**, 2278 (1994).

[11] G. Y. Robinson, *Metallurgical and Electrical Properties of Alloyed Ni-Au-Ge Films on N-Type GaAs.* Solid-State Electronics, **18**, 331 (1975).

[12] M. Ogawa, *Alloying Behaviour of Ni-Au-Ge Films on GaAs.* Journal of Applied Physics, **51**, 406 (1980).

[13] J. Gyulai, J. W. Mayer, V. Rodrigue, A. Y. C. Yu, H. J. Gopen, *Alloying Behaviour of Au and Au-Ge on GaAs.* Journal of Applied Physics, **42**, 3578 (1971).

[14] F. Lonnum and J. S. Johannessen, *Effect of Au-Ge Thickness on Ohmic Contacts to GaAs.* Electronics Letters, **22**, 632 (1986).

[15] P. Benjamin and C. Weaver, *Adhesion of metal films to glass.* Proceedings of the Royal Society of London. Series A, Mathematical and Physical Sciences, **254**, 177 (1960).

[16] S. Forment, M. Biber, R. L. Van Meirhaeghe, W. P. Leroy and A. Türüt, *Influence of hydrogen treatment and annealing processes upon the Schottky barrier height of Au/n-GaAs and Ti/n-GaAs diodes.* Semiconductor Science and Technology, **19**, 1391 (2004).

Chapter 5

Application of GHz bandwidth voltage pulses to a single quantum dot

The ability to apply GHz bandwidth voltage pulses to a single quantum dot allows fast electron charging/ionisation of an exciton on a nanosecond timescale. The electron from a neutral exciton is removed within the exciton recombination lifetime. A second-order electron tunneling interaction between the Fermi sea and the dot accounts for an increase in the electron spin-swap rate as the neutral exciton is ionised. Single photons can be electrically triggered from a single dot which is optically excited by CW non-resonant light. Single holes in a dot can be stored for >40 μs with no decay route unless they are electrically charged with an electron and allowed to decay as a neutral exciton. A dark neutral exciton can be stored within a single dot for >1 μs and electrical read out of a photon is possible by either altering the electron spin-flip lifetime, or by charging the dot with an additional electron: Electrical read out can be used to measure the non-radiative lifetime of the neutral exciton in low signal limits. Pulsed resonant creation of a hole in a single dot is shown along with electrical read out at several selectable exciton recombination energies. In the final section, adiabatic passage is attempted using electrically controlled CW resonant optical excitation of a neutral exciton into the dot. In an ideal case, a smooth alteration of the dot energy levels (using the Stark shift) through the energy of a tunable laser (tuned to the $|\,0\rangle \rightarrow X^0$ transition) can result in a 100 % probability of exciting the dot. Although the evidence presented here for adiabatic passage is mixed, this technique is shown to produce single photons on demand.

5.1 Charging an exciton within its fluorescence lifetime

In Chapter 4, photolithography was described to create a device allowing a single charge-tunable quantum dot to experience a voltage change on the time-scale of exciton recombination. The test used to measure the voltage time response of a dot in the device (see section 4.2.2, page 82) was performed with a CW laser. In essence, the test measured a time-varying change in the lowest energy charge configuration available to any carriers that relax into the dot. The test did **not** confirm the ability to manipulate electron tunneling to/from the dot with GHz bandwidth voltage pulses. Therefore, the question remains, can the temporal response of an optically excited dot be manipulated with a voltage pulse? It is shown here that a single dot can be charged/ionised through the use of electron tunneling, on the timescale of exciton recombination. This experiment was performed on the first microscopic device manufactured (Device A), constructed from Wafer B (050328B) designed as in Fig. 4.6 (Chapter 4, page 82).

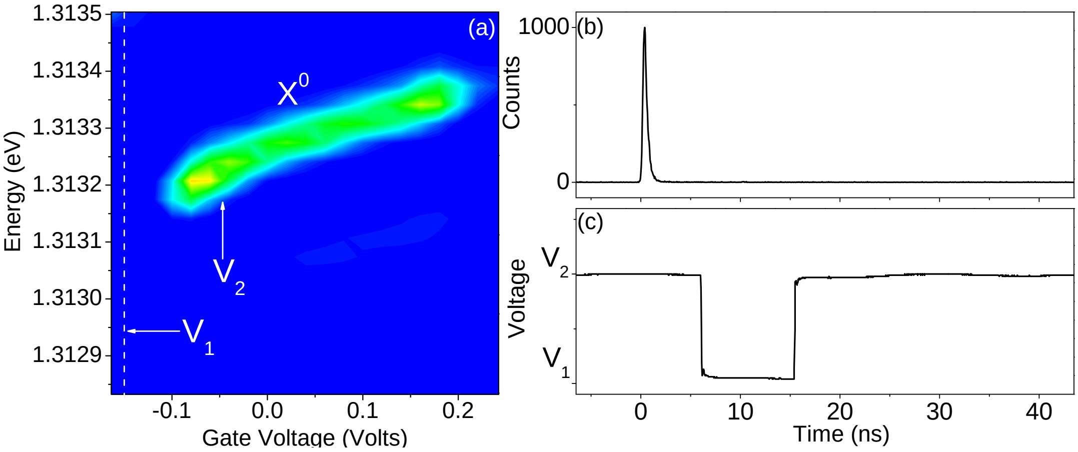

Figure 5.1: (a) Contour plot showing PL from a dot in Wafer B (050328B), constructed within a device (Device A) designed as in Fig. 4.6, as a function of applied gate bias when excited with 7.2 nW μm^{-2} of 830 nm CW laser light. Background counts (<100 counts) are shown as dark blue and increasing counts are shown as light blue (~2000 counts), green (~4000 counts), yellow (~6000 counts) and red (6400 counts). $V_1 = -150$ mV is the voltage point chosen at which only a hole can be stored in the dot. $V_2 = -50$ mV is a point within the X^0 extent at which both lifetime components to the exciton decay are comparable in time. (b) A SPAD-based measurement of the non-resonant 100 ps pulses of 826 nm laser light used to excite the sample with an average of 4.4 nW μm^{-2} at a repetition rate of 20 MHz. (c) An oscilloscope measurement of the time-varying voltage pulse applied between the Schottky gate and the back contact between the voltage points specified in (a) and with a constant phase difference to (b).

A single dot in Wafer B was chosen for being spatially and chromatically isolated with respect to other dots in Device A. The dot was excited with 7.2 nW μm^{-2} of non-resonant 830 nm laser light, and the PL was measured as a function of voltage bias as shown in Fig. 5.1(a). The neutral exciton PL was identified as discussed in Chapter 3 section 3.1.2. Two voltage bias points were chosen: V_1 (=-150 mV) was positioned 60 mV beyond the low bias edge of the X^0 plateau, at which point there is a high probability that non-resonant optical excitation will result in a single hole being trapped in the dot. V_2 (=-50 mV) was chosen to be 100 mV higher than V_1, at which point X^0 TRPL consists of two comparable lifetimes.

The dot was illuminated with 100 ps pulses from an 826 nm laser at a repetition rate of 20 MHz (Fig. 5.1(b)) and an average power of 4.4 nW μm^{-2}. At all times the pulsed laser was triggered by the PPG (as discussed in Chapter 2 section 2.5.2). The bias voltage was held static at V_2 (by the PPG) and TCSPC was performed on the PL from X^0. The resulting TRPL (Fig. 5.2, black) shows a standard X^0 lifetime with two exponential decays. The primary (fast) decay is due to recombination of the bright X^0, which occurs with a lifetime of 1.1 ns (see Chapter 3 section 3.3). The secondary (slow) decay is due to the dark X^0, which cannot radiatively recombine due to its angular momentum $L = 2$ (see Chapter 1 section 1.2.2). The dark exciton must first undergo an electron spin-flip which occurs due to a tunneling interaction between the dot and the back contact (see Chapter 3 section 3.3), allowing recombination with a total lifetime of 6.6 ns for V=V_2.

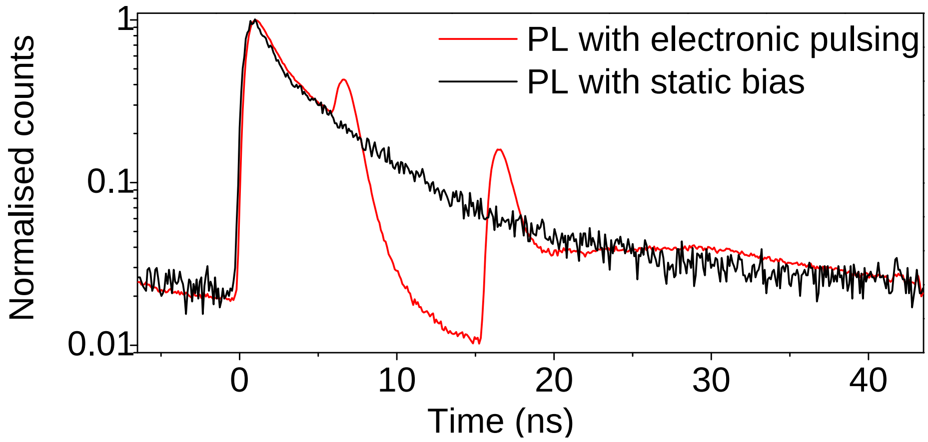

Figure 5.2: TRPL of X^0 from the dot represented in Fig. 5.1(a) when excited by 100 ps pulses of non-resonant 826 nm laser light at a repetition rate of 20 MHz and an average power of 4.4 nW μm^{-2}, as represented in Fig. 5.1(b). In the first case (black line) the applied voltage bias is held static at V_2. In the second case (red line) a time-varying voltage (Fig. 5.1(c)) is applied across the sample between V_1=-150 mV and V_2=-50 mV.

While maintaining the pulsed optical excitation as shown in Fig. 5.1(b), the PPG was used to apply a 20 MHz time-varying voltage pulse (Fig. 5.1(c)) of pulse width 9.4 ns to the sample, between V_1 and V_2. TCSPC was once again performed on the

PL from X^0, and the results are shown in Fig. 5.2(red). There are several significant differences to the static voltage case Fig. 5.2(black), which in and of itself is evidence that the temporal response of the dot has been successfully manipulated using a voltage pulse. There is a pronounced dip in count rate between 8 ns and 16 ns, and immediately before and after this dip are higher count rates at 7 ns and 17 ns, corresponding in time to the voltage pulse applied by the PPG. There is a slightly raised count rate at ∼30 ns, and the count rate at 15 ns is lower than the rate observed just before the laser pulse at t=0. The dip between 8 ns and 16 ns can be shifted in time if the electronic pulse is delayed with respect to the laser pulse.

When $V=V_1$ (between 8 ns and 16 ns) there is almost no emission from the dot. This corresponds to a region within which the energetically favourable single-hole charge combination in the dot is a single hole. It is reasonable to conclude therefore that any neutral exciton in the dot as $V \rightarrow V_1$ will be ionised, leaving a single hole. The experiment has therefore shown that hole ionisation is possible on the timescale of exciton recombination, using GHz bandwidth voltage pulses.

At 7 ns the voltage across the dot starts to change from V_2 towards a lower bias, V_1. From Chapter 3 section 3.3.2 it is known that the X^0 secondary lifetime decreases at each edge of the X^0 PL bias extent, due to a second-order electron tunneling interaction (co-tunneling) between the dot and the back contact. As the electron spin-flip rate becomes larger than the recombination rate, some dark X^0 in the dot experience an electron spin-flip interaction with the back contact, which allows the exciton to become bright and recombine radiatively. It is likely that the peak observed in Fig. 5.2(red) at 7 ns is due to an increased electron spin-flip rate as the voltage lowers towards the edge of the X^0 PL bias extent.

As the voltage becomes lower than the h-X^0 charging point any electrons that are in the dot tunnel out within several ps [2], leaving a single hole. In Wafer B there are no prominent decay paths available to a single hole trapped in a dot at 4 K, without electronic or optical manipulation. A hole can be stored in this way indefinitely (see Section 5.4 on page 111). Between 8 ns and 16 ns, the dip in PL count rate is therefore due to the storage of a single hole in the dot.

After storing a hole for ∼8 ns the voltage starts to return to V_2. As the bias passes the h-X^0 charging point an electron tunnels into the dot within ps [2], creating an X^0. The spin-flip rate is fast at the h-X^0 charging point, so the peak in counts at t=17 ns could reasonably be due to both bright X^0 decay, and dark X^0 which experience an electron spin-flip to become bright X^0 and then decay. As the voltage settles at V_2 the primary and secondary X^0 lifetimes are similar to the lifetimes at t=0, and the X^0 decays as normal.

The background level just before the laser pulse (e.g. t=-1 ns) is higher than that at 15 ns. This is thought to be because while the voltage is within the X^0 plateau (at $V=V_2$) there is a small probability of excess charge remaining in the dot or the wetting layer after optical excitation, which has the potential to recombine as X^0 (as observed in Chapter 3 section 3.4). At t=15 ns and V=V_1 it is impossible to create an X^0 within the dot due to the Coulomb blockade (see Chapter 3 section 3.1.3).

It is not known why there is a comparative PL rate difference between the two scans at t=∼30 ns. A potential cause may be a slight fluctuation in the time-varying voltage pulse.

5.2 Probing the spin-flip peak

The peaks observed in Fig. 5.2 at t=7 ns and t=17 ns are explained with the assumption that there is no significant ringing in the voltage experienced by the dot as it is changing. Presented here is an attempt to check for ringing in the voltage pulse. The idea is to modulate the voltage in a range where the dark–to–bright electron spin flip rate of the neutral exciton is very sensitive to the instantaneous voltage. In this way, any ringing which occurs in the voltage experienced by the dot will appear as an unexpected modulation of the electron spin flip rate.

Using the same dot as in section 5.1, two voltage points were chosen within the neutral exciton plateau (Fig. 5.3(a)). V_2 (=-50 mV) was chosen to be constant at a point on X^0 that emits photons with an obvious bi-exponential decay (40 mV from the h-X^0 charging point). V_1 was initially chosen to be also within the X^0 plateau at a slightly more negative bias, and was decreased to even more negative bias values between successive scans.

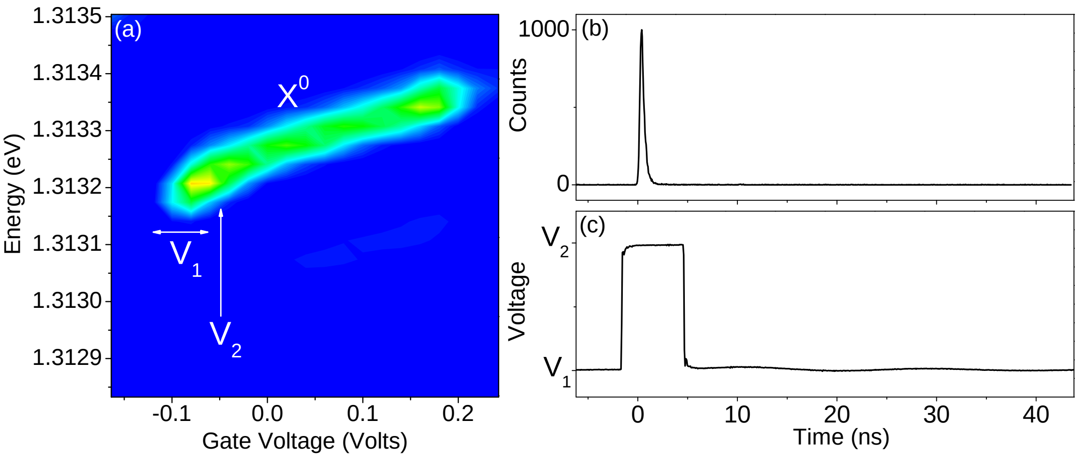

Figure 5.3: (a) The same contour plot as shown in Fig.5.1(a). V_1 was varied between successive scans but is always lower than V_2 (=-50 mV), which was chosen to be 40 mV from the h-X^0 charging point (-90 mV). (b) A SPAD-based measurement of the 100 ps pulses from a non-resonant 826 nm laser used to excite the sample at a repetition rate of 20 MHz and an average power of 4 nW μm^{-2}. (c) An oscilloscope measurement of the time-varying voltage pulse applied between the Schottky gate and the back contact between the voltage points specified in (a).

The dot was illuminated with 100 ps pulses of non-resonant 826 nm laser light with an average power of 4 nW μm^{-2} (Fig. 5.3(b)). The PPG was used to apply time-varying voltage pulse between V_1 and V_2 (Fig. 5.3(c)). Both the laser and electronic pulses had a repetition frequency of 20 MHz. TRPL of X^0 was taken for several values of V_1, shown in Fig. 5.4(a)–(f). As V_1 is moved to lower biases a peak appears at t=6.5 ns, and the rest of the decay after the peak disappears.

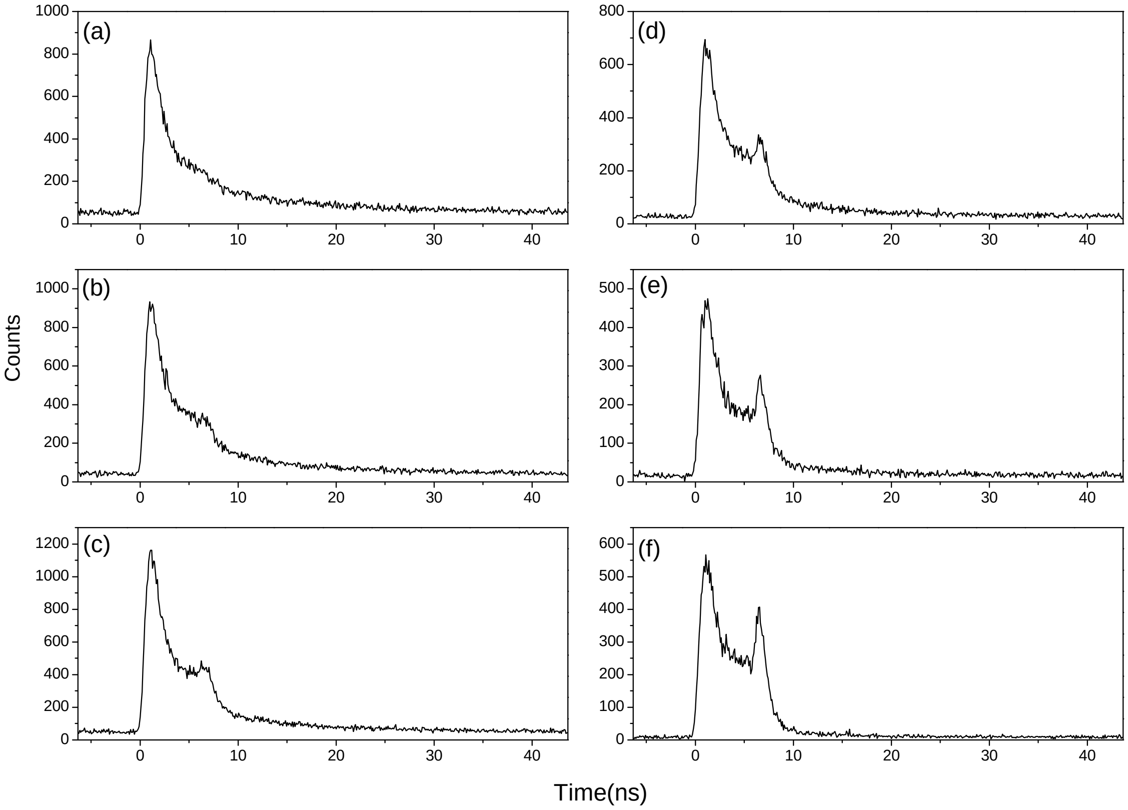

Figure 5.4: TRPL of X^0 from the dot represented in Fig. 5.3(a) when it is optically excited with 100 ps pulses of non-resonant 826 nm laser light with an average power of 4 nW μm^{-2} (Fig. 5.3(b)), and electrically manipulated as in Fig. 5.3(c). V_2 (=-50 mV) is +40 mV from the h-X^0 charging point. V_1 is biased at (a) -60 mV (b) -65 mV (c) -77 mV (d) -81 mV (e) -90 mV (f) -121 mV.

As the voltage applied by the PPG starts to decrease at t=5 ns, the secondary lifetime due to the dark X^0 decreases due to co-tunneling. In this way a faster recombination rate causes an increase in counts at t=6.5 ns. The peak at t=6.5 ns becomes larger as V_1 is decreased because the recombination at V_1 becomes increasingly fast, and as such it is more likely that a recombination will occur at this point. In the same way, as V_1 is lowered there is a decrease in counts in the curve after the peak at t=6.5 ns as there is a smaller probability of finding a dark X^0 in the dot.

The peak at t=6.5 ns increases steadily from (a)–(f), relative to the peak at t=0. Also, the peak at t=6.5 ns always appears at the same time, from (a)–(f). Lastly, no tertiary peaks are observed in any of the TRPL measurements. Any substantial ringing in the voltage pulse experienced by the dot would be expected to show up as an unexpected behaviour in the appearance of the peak at t=6.5 ns. This could reasonably occur as a decrease in the peak height with decreasing V_1 (relative to the peak at t=0), a change in the time the peak appears, or the appearance of tertiary peaks. Therefore it is reasonable to conclude that there is no ringing in the voltage pulse.

5.3 Single photons on demand using CW non-resonant excitation

One of the main goals of this project is to use GHz bandwidth voltage pulses to bias a quantum dot in order to create an electrically triggered deterministic single photon source. The microscopic devices used in this chapter allow optical excitation and electrical manipulation of the charge tunable structure, giving two methods of controlling the behaviour of a dot. Here, a single dot is optically excited with non-resonant CW laser light, creating a single hole in the dot. Fast voltage pulsing is used to control the ability of the dot to form a neutral exciton. The dot is from Wafer B (050328B), embedded within a microscopic device (Device A) constructed as in Chapter 4, Fig.4.6.

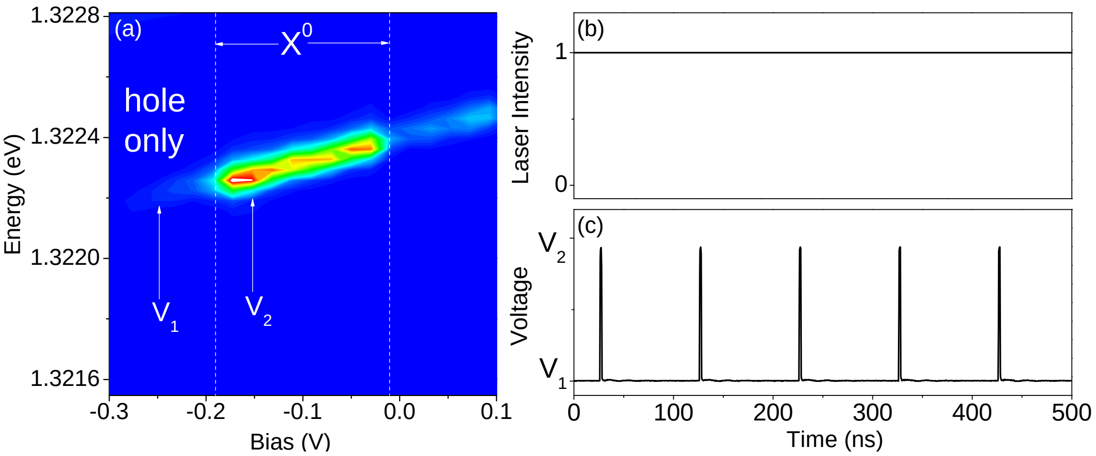

Figure 5.5: (a) Contour plot showing the PL from a dot in Wafer B within a fast device (designed as in Chapter 4, Fig.4.6), as a function of applied gate bias when excited with 13.6 nW $\mu\mathrm{m}^{-2}$ of CW non-resonant 830 nm laser light. Background counts (<100 counts) are shown as dark blue and increasing counts are shown as light blue (∼300 counts), green (∼500 counts), yellow (∼800 counts), red (1000 counts) and white (>1200 counts). (b) The laser intensity showing constant 830 nm CW light at a power of 13.6 nW $\mu\mathrm{m}^{-2}$. (c) An oscilloscope measurement of the time-varying electronic pulse (pulse duration ∼1 ns) applied to the sample.

A single dot (Fig. 5.5(a)) was excited non-resonantly with 830 nm CW laser light

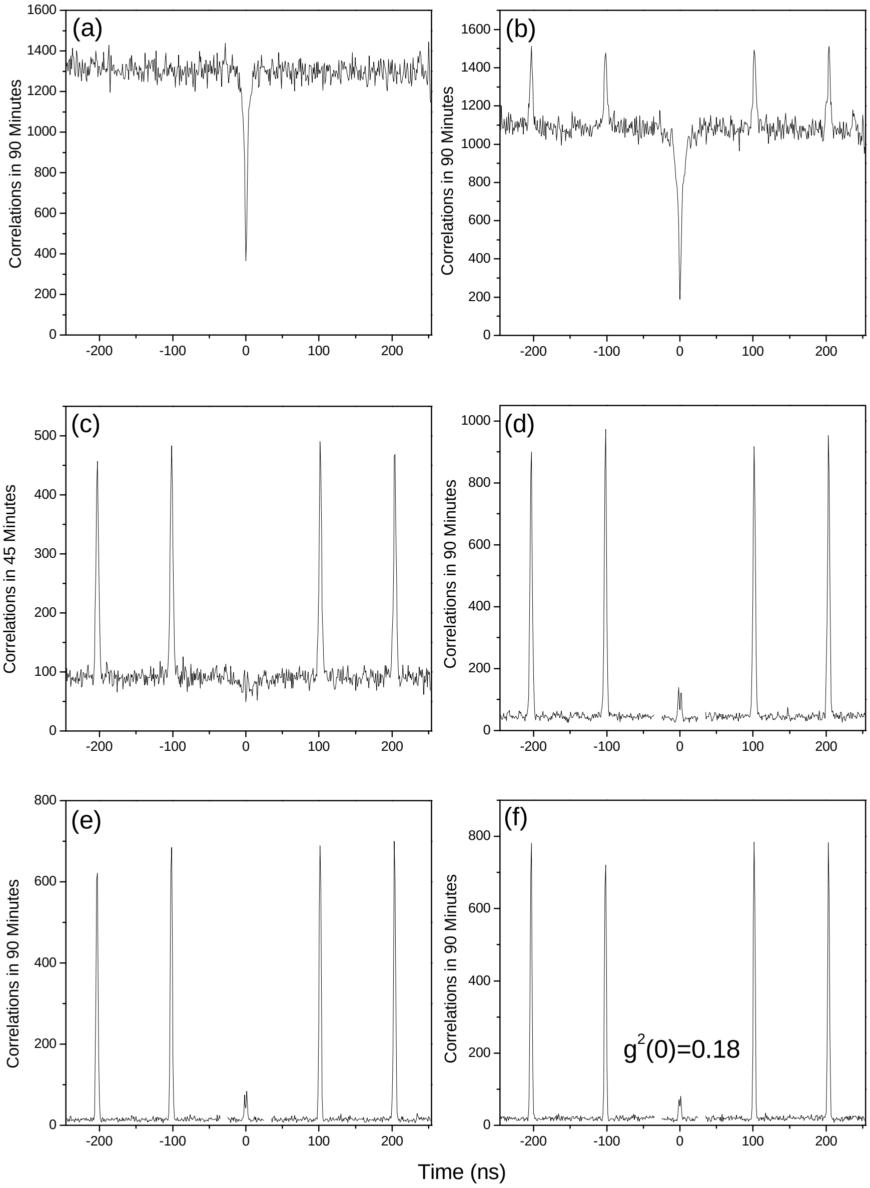

Figure 5.6: Autocorrelation plots for the neutral exciton as the device bias is changed on a nanosecond timescale (as described in Fig. 5.5(c)), while the dot is excited by CW laser light (as described in Fig. 5.5(b)). From (a) through to (f) can be seen a gradual change from CW autocorrelation through to individual photon "Fock" states. Relative to the h-X^0 charging point the V_1 and V_2 values are respectively (a) +60 mV and +160 mV, (b) +20 mV and +120 mV, (c) 0 mV and +100 mV, (d) -20 mV and +80 mV (e) -60 mV and +40 mV, and (f) -100 mV and 0 mV. In (f) the g2(0) value is 0.18. Features due to light emission from the SPADs during photon detection (discussed in Chapter 2 section 2.3) were observed at t=±30 ns in (d), (e) and (f), and have been removed.

(Fig. 5.5(b)) at a power of 13.6 nW μm^{-2}. Two voltage points (V_1 and V_2, Fig. 5.5(a)) were chosen within X^0 with a voltage difference of 100 mV. The PPG was used to apply a voltage $V=V_2$ across the device for ~1 ns with a frequency of 10 MHz (Fig. 5.5(c)). At all other times the PPG was used to apply a voltage $V=V_1$ across the device. Autocorrelation scans of X^0 were taken using the HBT as in Chapter 2 2.3, varying the offset of V_1 and V_2 between successive scans. The voltage difference between V_1 and V_2 was kept constant.

Fig. 5.6 (a)–(f) show the progression as the voltage offset of V_1 and V_2 was decreased to a more negative bias. In (a) the scan resembles a standard autocorrelation with CW optical excitation. In (f) the scan looks remarkably similar to that of an autocorrelation using a pulsed excitation source. Scans (b)-(e) show several intermediate stages in which a hybrid of scans (a) and (f) are observed. Scan (f) has a $g^{(2)}(0)$ value of 0.18.

Fig. 5.6(a) looks identical to a standard CW autocorrelation because voltage pulsing between different points in the centre of the X^0 plateau only slightly affects the exciton recombination energy via the Stark shift, and has little affect on the intensity.

As both voltages are lowered simultaneously V_1 starts to enter the h-X^0 charging region in which there is a smaller probability of an electron tunneling into the dot, and so the median count rate starts to decrease. At $t = 100N$ ns (where N is an integer value) the voltage pulse to V_2 causes a temporary increase in the probability of an X^0 forming in the dot, and an increased count rate is observed.

On approaching the gate voltage conditions of Fig. 5.6(f) the base level drops to the noise level of the system, indicating the only time the system will allow an X^0 to form in the dot and recombine is during an electronic pulse. The $g^{(2)}(0)$ value of 0.18 confirms that although the dot is excited with CW laser light, GHz bandwidth voltage pulsing has forced the PL to be emitted with a sub-Poissonian multi-photon probability. Arguably this is a demonstration of an electrically triggered deterministic single photon source, in which the voltage pulse has an 82% probability of creating a single photon. Although the $g^{(2)}(0)$ value is non-zero, it is expected (based on the results from Chapter 3 section 3.4) that any secondary photons are emitted sequentially, not simultaneously.

5.4 Hole bit storage with neutral exciton read out

In Chapter 3 section 3.3.3 it was concluded that Wafer B (050328B) was preferable for use with GHz bandwidth voltage pulsing because it did not exhibit hole tunneling effects. This is particularly important with regards to the idea of bit memory, in which a hole of known spin is stored within a quantum dot. Hole tunneling from the dot (large T_1 value) to hole continuum states (for instance in the capping layer, small T_1 value) would lose the bit information. Here, GHz bandwidth voltage pulsing is used to determine how long it is possible to store a single hole in a dot from Wafer

B before non-radiative decay paths become relevant. This is achieved by optically exciting a single hole into the dot at high reverse bias, and then some time later using GHz bandwidth voltage pulsing to increase the voltage and introduce a single electron into the dot, forming a neutral exciton and radiatively recombining to release a photon which can be measured. In this way, the observation of a photon serves as a measurement of the probability of a hole existing in the dot at the time of the voltage pulse.

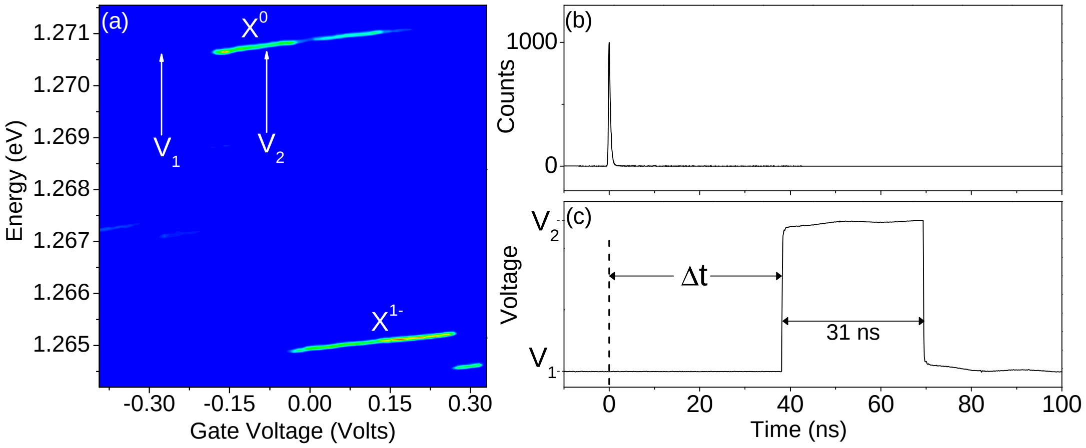

Figure 5.7: (a) Contour plot showing the dot PL against gate bias for a single dot in Wafer B within a device (Device C) designed as in Chapter 4 Fig. 4.9, optically excited with 55.2 nW μm^{-2} of CW non-resonant 830 nm laser light. Background counts (<100 counts) are shown as dark blue and increasing counts are shown as green (~140 counts), yellow (~180 counts), and red (220 counts). V_1 (=-280 mV) is at a bias which allows electron field ionisation and hence hole storage, V_2 (=-75 mV) is at a bias which allows the creation and recombination of X^0. (b) A SPAD-based measurement of the 100 ps 826 nm laser pulse used to excite the sample with a 20 kHz repetition rate and an average power of 0.48 nW μm^{-2}. (c) An oscilloscope measurement of the time-resolved voltage applied between the gate and the back contact, changing between V_1 and V_2 with a 20 kHz repetition rate

A single dot in Wafer B (manufactured within Device C, designed as in Chapter 4, Fig. 4.9) was chosen for being spatially and chromatically distinct from other dots. The dot was excited with 55.2 nW μm^{-2} of CW non-resonant 830 nm laser light, and the PL was recorded as a function of gate voltage in Fig. 5.7(a). Fig. 5.7(a) shows clear charging behaviour, and the excitons are identified as discussed in Chapter 3 section 3.1.2. Two voltage points were chosen: V_1 (=-280 mV) was chosen to be -105 mV from the h-X^0 charging point, at a region in which only a single hole is stored in the dot. V_2 (=-75 mV) was placed +205 mV from V_1, at a point well within the X^0 voltage bias extent.

The dot was excited with 100 ps pulses of non-resonant 826 nm laser light at a repetition rate of 20 kHz, and an average power of 0.48 nW μm^{-2} (as in Fig. 5.7(b)). The PPG was used to apply a voltage V_1 from t=0, and after a delay time Δt the

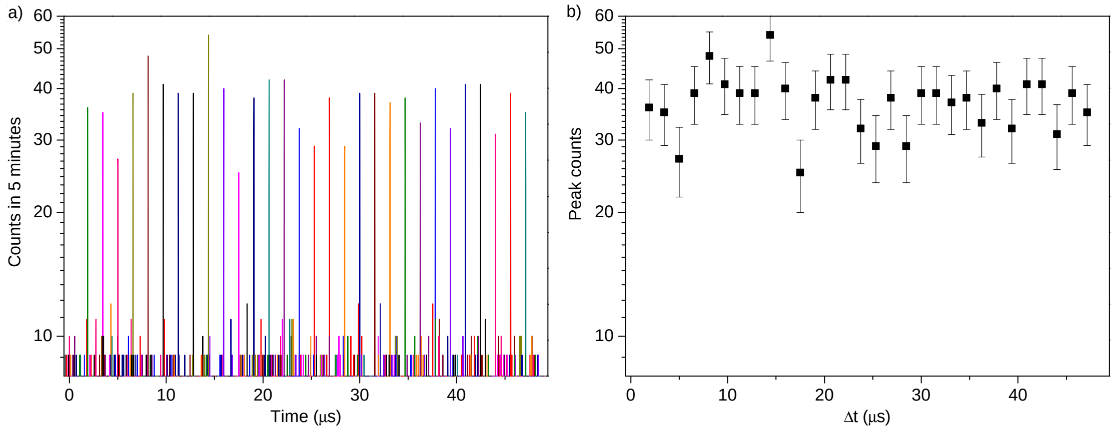

Figure 5.8: (a) TRPL of X^0 showing the number of counts measured for various Δt when the dot represented in Fig. 5.7(a) is excited by 100 ps pulses of 826 nm laser light (Fig. 5.7(b)) with a repetition rate of 20 kHz and an average power of 0.12 nW, and the PPG is used to apply a voltage between the gate and the back contact, as in Fig. 5.7(c). (b) The peak counts from (a) plotted with the estimated error due to shot noise, where the expected shot noise is approximately the square root of the peak count value.

voltage was raised to V_2 for 31 ns (Fig. 5.7(c)). TCSPC of X^0 was performed for each of 30 different values of Δt, and presented in Fig. 5.8.

No significant reduction in count rate was observed in Fig. 5.8 as Δt is increased, even for Δt=45 μs which was the largest time that could be measured with this method, limited by the TCC900 timing card which is used to measure the timing events (see Chapter 2 section 2.5). From section 5.1 it is already known that GHz bandwidth voltage pulses can be used to charge the dot with an additional electron. In this case, if a photon of X^0 PL is recorded at a time Δt from the laser pulse used to excite the dot, it is reasonable to conclude that a single hole has been stored in the dot for a time Δt before being charged with an electron (due to the voltage pulse from the PPG), and recombining to form a photon. Therefore, it is reasonable to conclude that there are no non-radiative paths available to a hole in the dot on a 45 μs timescale. This result is unsurprising as, unlike Wafer A (10311A), in Wafer B (050328B) there are no energy levels within the capping layer that can become resonant with those of the dot (discussed in Chapter 3, section 3.3.3), therefore hole tunneling from the dot into the capping layer is unlikely. Since the dot valence band is at a higher energy than anything else around it there is very little probability of the hole escaping. As such, when the laser pulse excites the sample, the electron relaxes/tunnels into the back contact, and the hole relaxes into the dot and is stored. When the voltage is changed to V_2 an electron tunnels into the dot and the X^0 can recombine, producing a photon. This is expected given the results of Chapter 3 section 3.4 in which the valence s-orbital of the dot is expected to be at least ~55 meV higher in energy than anything around it.

5.5 Dark exciton bit storage with neutral exciton read out

In Chapter 3 section 3.3.2, a second-order electron tunneling interaction between the dot and the back contact was identified due to the change in secondary lifetime of PL from X^0. Essentially, the interaction is revealed by an electron spin-flip, turning a dark X^0 into a bright X^0. In section 5.1, it was shown that GHz bandwidth voltage pulses can electrically trigger this electron spin-flip in a dark X^0, and the resulting bright X^0 will recombine to give an increased count rate. This affords the opportunity to create a memory bit with a defined write-store-read process, in which non-resonant optical excitation is used to "write" a dark X^0 into the dot, which is then "stored" until a GHz bandwidth voltage pulse is used to "read" the exciton by causing an electron spin-flip and recombination as a bright X^0.

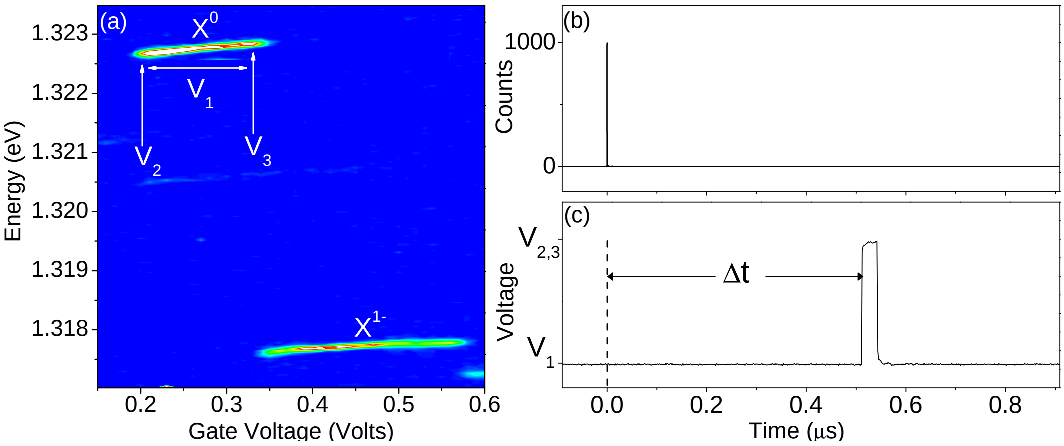

Figure 5.9: (a) The PL against voltage bias for a dot from Wafer B embedded within a fast device (Device B, designed as in Chapter 4, Fig. 4.9), when excited with 100 ps pulses of non-resonant 826 nm laser light with a repetition rate of 1 MHz, and a power of 16 nW μm^{-2}. Background counts (<90 counts) are shown as dark blue and increasing counts are shown as light blue (∼100 counts), green (∼130 counts), yellow (∼140 counts), red (150 counts) and white (>160 counts). (b) A SPAD-based measurement of the 100 ps pulses of non-resonant 826 nm laser light applied to the dot, with a repetition rate of 1 MHz, and an average power of 16 nW μm^{-2}. (c) An oscilloscope measurement of the time-varying voltage pulse applied across the sample between either V_1 and V_2, or V_1 and V_3, with a constant delay with respect to the laser pulse in (b).

A single dot in Wafer B (from within Device B, designed as in Chapter 4, Fig. 4.9) was chosen for being spatially and chromatically isolated. The PL against voltage bias was recorded as the dot was excited with 100 ps pulses of non-resonant 826 nm laser light with a repetition rate of 1 MHz, and a power of 16 nW μm^{-2} (Fig. 5.9(a)). The following static voltage biases are defined: V_1 is chosen to be a point in the centre of the X^0 plateau and is considered the "write" voltage. V_2 (=200 mV) is positioned at the low bias edge of the X^0 extent in which the spin-flip rate is dominant over the radiative lifetime, and functions as a "read" voltage. V_3 (=330 mV) is positioned at the high bias edge of the X^0 extent in which the spin-flip rate is dominant over the radiative lifetime, and also functions as a "read" voltage.

A 100 ps pulse from an 826 nm laser (Fig. 5.9(b)) with a repetition rate of 1 MHz and an average power of 16 nW μm^{-2} was used to excite the dot. The PPG was used to apply a voltage $V = V_1$. At different "storage" values (Δt) the voltage was changed to either V_2 or V_3 (Fig. 5.9(c)) for 63 ns. TCSPC was performed on the PL from X^0 for each Δt value. This was repeated for several values of V_1 across the X^0 voltage bias extent.

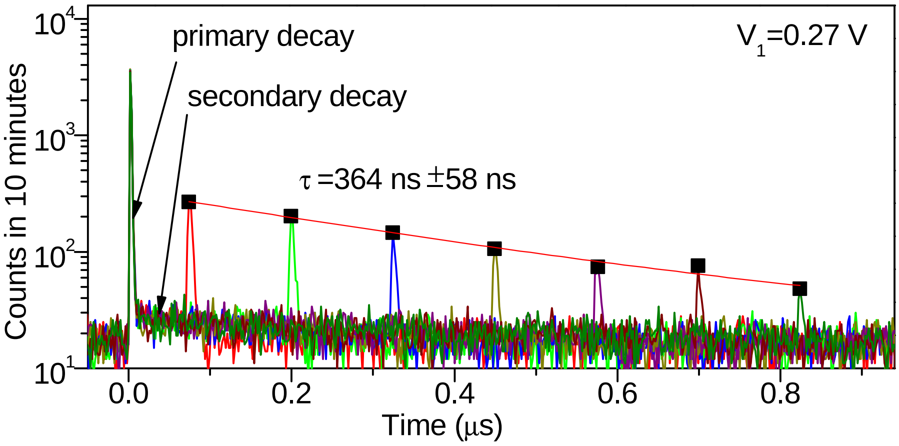

Figure 5.10: TRPL of X^0 recorded when the dot represented in Fig. 5.9(a) is excited with 100 ps pulses of 826 nm laser light with a repetition rate of 1 MHz at an average laser power of 16 nW μm^{-2} (as in Fig. 5.9(b)) and the PPG is used to apply a time-varying voltage (represented in Fig. 5.9(c)) between V_1 (=0.27 V) and V_3 (=0.33 V) across the device. Seven individual scans are included in the plot, for seven different values of Δt (=70 ns (red), =195 ns (green), =320 ns (blue), =445 ns (dark yellow), =570 ns (purple), =695 ns (wine), =820 ns (olive)). The peak counts at Δt in each scan have been fitted with an exponential decay (red line) in order to find the electron spin-flip time (τ) at V_1.

Fig. 5.10 shows the TCSPC for V_1=0.27 V, including seven different values of Δt (70 ns, 195 ns, 320 ns, 445 ns, 570 ns, 695 ns, 820 ns) at which the PPG is used to changed the voltage to V_3. There is a peak at t=0 with a fast primary lifetime (∼600 ps), followed by a secondary slow exponential decay (∼400 ns). At t=Δt the voltage is changed to V_3 and a second PL peak is recorded. Comparing each of the TRPL scans for each Δt value, there is a clear reduction in peak size as Δt is increased. The peak points are fitted well with an exponential decay. The slope of the exponential decay depends on the value of V_1: as V_1 is becomes closer to either edge of the X^0 plateau the exponential decay becomes faster.

In Fig. 5.10, the peak at t=0 has a lifetime component of ~600 ps, and is closely correlated to the time of the laser pulse. A reasonable conclusion is therefore that the peak at t=0 is due to the decay of the bright neutral exciton, which has been "written" into the dot by the laser pulse. The secondary lifetime component (~400 ns) observed must therefore be due to the dark exciton, which is "stored" in the dot until a slow co-tunneling interaction with back contact changes the spin of the electron, causing the dark X^0 to become bright and recombine radiatively within ~1 ns. At t=Δt, the peak observed confirms that randomisation of the electron spin occurs due to the PPG, which raises the voltage to V_3. In this case, the voltage pulse from the PPG forces the co-tunneling rate to increase, and the emission of a photon can be measured in order to form a "read" step. In this way GHz bandwidth voltage pulsing has been successful in using the dark exciton as a memory bit.

Using the PPG to pulse from V_1 to V_2 with the same optical excitation as before (Fig. 5.9(b)) causes the same spin-flip process to occur at t=Δt, and therefore TCSPC of X^0 yields the same result as in Fig. 5.10. The height of the peak at t=Δt can be considered a measurement of the total probability of a dark exciton remaining in the dot at a time Δt after optical excitation, therefore an exponential fit to the peak values (Fig. 5.10, red line) gives a value for the neutral exciton secondary lifetime (τ) at $V=V_1$.

5.6 Dark exciton bit storage with negative trion read out

In section 5.1 it was proven that GHz bandwidth voltage pulsing can be used to charge a dot with an additional electron within the timescale of exciton recombination. In section 5.5, the dark exciton was successfully used as a memory bit. However, the fine structure of the neutral exciton may cause problems with respect to transferring the spin of the hole to the polarisation of the photon. Here, an alternative "read" step is implemented for the write-store-read process demonstrated in section 5.5, in which stored dark excitons are charged with an additional electron to become X^{1-} and recombine in ~1 ns (as expected from Chapter 3, section 3.3.1). X^{1-} has no fine structure, so the hole spin will be transferred to the photon polarisation. However, it was unknown whether a dark exciton in the dot could traverse the co-tunneling bias region (V_3 in section 5.5) without turning bright and recombining, in order to reach the X^{1-} plateau. This experiment uses the same dot as section 5.5.

The dot represented in Fig. 5.11(a) was excited using 100 ps pulses of 826 nm laser light with a repetition rate of 500 kHz and an average power of 9.6 nW μm^{-2} (Fig. 5.11(b)). Two voltages were chosen: V_1 was placed in the centre of the X^0 plateau, as defined in section 5.5. V_4 (=540 mV) is at the high bias end of the X^{1-} plateau (Fig. 5.11(a)), in order to minimise the time over which the dot experiences a voltage

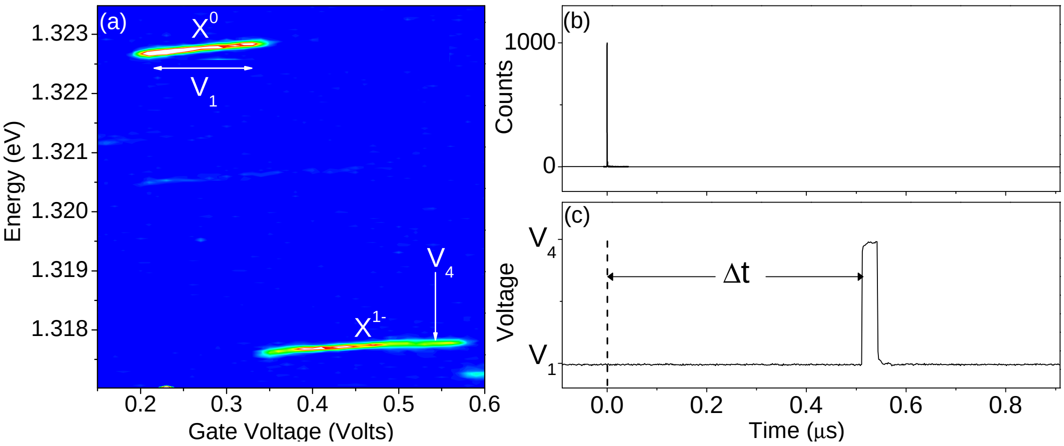

Figure 5.11: (a) The same contour plot as in Fig. 5.9(a). (b) A SPAD-based measurement of the 100 ps pulses of non-resonant 826 nm laser light applied to the dot, with a repetition rate of 500 kHz, and an average power of 9.6 nW μm^{-2}. (c) An oscilloscope measurement of the time-varying voltage pulse applied across the sample between V_1 and V_4, with a constant phase with respect to the laser pulse in (b).

within the X^0 co-tunneling region. The PPG was used to apply a voltage $V=V_1$. At different "storage" values (Δt) the voltage was changed to V_4 (Fig. 5.11(c)) for 63 ns. TCSPC was performed on the PL from X^{1-} for each Δt value. This was repeated for several values of V_1 across the X^0 voltage bias extent.

Fig. 5.12 shows the TCSPC for V_1=0.27 V, including seven different values of Δt (102 ns, 287 ns, 539 ns, 852 ns, 1166 ns, 1416 ns, 1666 ns) at which the PPG is used to changed the voltage to V_4 (=540 mV). At each value of Δt an X^{1-} PL peak is recorded. Comparing each of the TRPL scans for each Δt value, there is a clear reduction in peak size as Δt is increased. The peak points are fitted well with an exponential decay. The slope of the exponential decay depends on the value of V_1: as V_1 is placed closer to either edge of the X^0 voltage bias extent the exponential decay becomes faster.

As in Section 5.5, when the laser pulse (Fig. 5.11(b)) excites the sample all the bright X^0 that are formed decay within ~1 ns, leaving only dark X^0. The dark exciton can be stored due to its long spin-flip lifetime. At t=Δt the PPG changes the voltage applied to the sample from V_1 to V_4 (Fig. 5.11(c)). When the voltage experienced by the dot crosses the X^0–X^{1-} charging point (V=0.35 V) a second electron tunnels into the dot, forming X^{1-}. X^{1-} has no fine structure and is free to recombine radiatively with a characteristic lifetime of around 700 ps, which can be considered the "read" part of the process. An exponential fit to the peaks (Fig. 5.12, red line) give a value for the secondary lifetime (τ) of the neutral exciton at $V=V_1$.

Figures 5.10 and 5.12 contain data from the same V_1 value (=0.27 V). Fig. 5.10 measures τ to be 364±58 ns, and Fig. 5.12 is in good agreement with a τ value of 418±54 ns. The count rate observed in Fig. 5.12 is larger than that of Fig. 5.10,

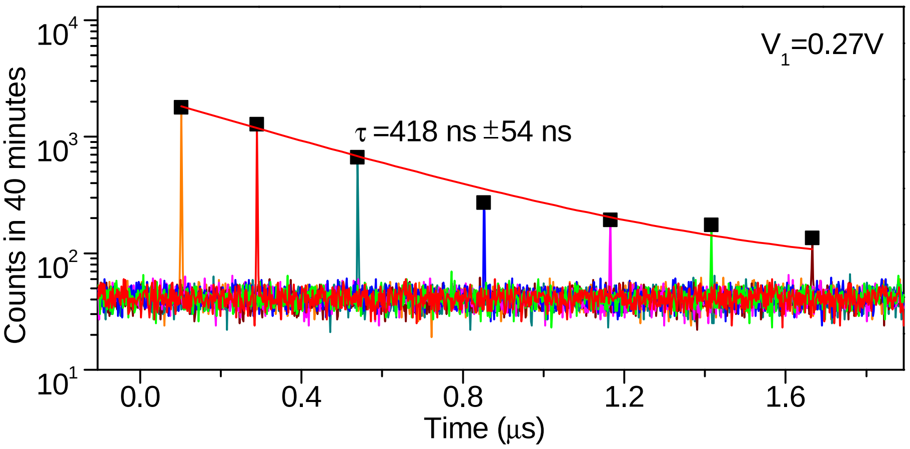

Figure 5.12: TRPL of X^{1-} recorded when the dot represented in Fig. 5.11(a) is excited with 100 ps pulses of 826 nm laser light with a repetition rate of 500 kHz at an average laser power of 9.6 nW μm^{-2} (as in Fig. 5.11(b)) and the PPG is used to apply a time-varying voltage (represented in Fig. 5.11(c)) between V_1 (=0.27 V) and V_4 (=0.54 V) across the device. Seven individual scans are included in the plot, for seven different values of Δt (=102 ns (orange), =287 ns (red), =539 ns (cyan), =852 ns (blue), =1166 ns (pink), =1416 ns (green), =1666 ns (brown)). The peak heights of the Δt peak in each scan have been fitted with an exponential decay (red line) in order to find the electron spin-flip time (τ) at V_1.

due to changes in alignment in the time between each set of scans. Unfortunately, this means that it is not possible to quantify the percentage of dark excitons which are able to cross the X^0–X^{1-} charging point. However, the result from Fig. 5.12 is still encouraging as it confirms that it is possible for a dark exciton to cross the co-tunneling region without emitting as a bright X^0.

5.7 Comparison of dark exciton lifetime measurements

Sections 5.5 and 5.6 give two methods for measuring the secondary lifetime of the neutral exciton. In both sections, varying $V=V_1$ allows a measurement of τ over the bias extent of X^0. Here, the results from both measurement methods are compared with the neutral exciton secondary lifetime as measured by standard TCSPC performed with a static voltage bias (as performed in Chapter 3, section 3.3).

As can be seen in Fig. 5.13(a), the τ values obtained from sections 5.5 (green and yellow triangles) and 5.6 (red triangles) closely follow the secondary lifetime of X^0 measured using TCSPC and a static voltage bias (black and blue circles). The dependence of τ on the gate bias can be understood by calculating the electron spin swap rate from the Anderson Hamiltonian [2] which is reduced to

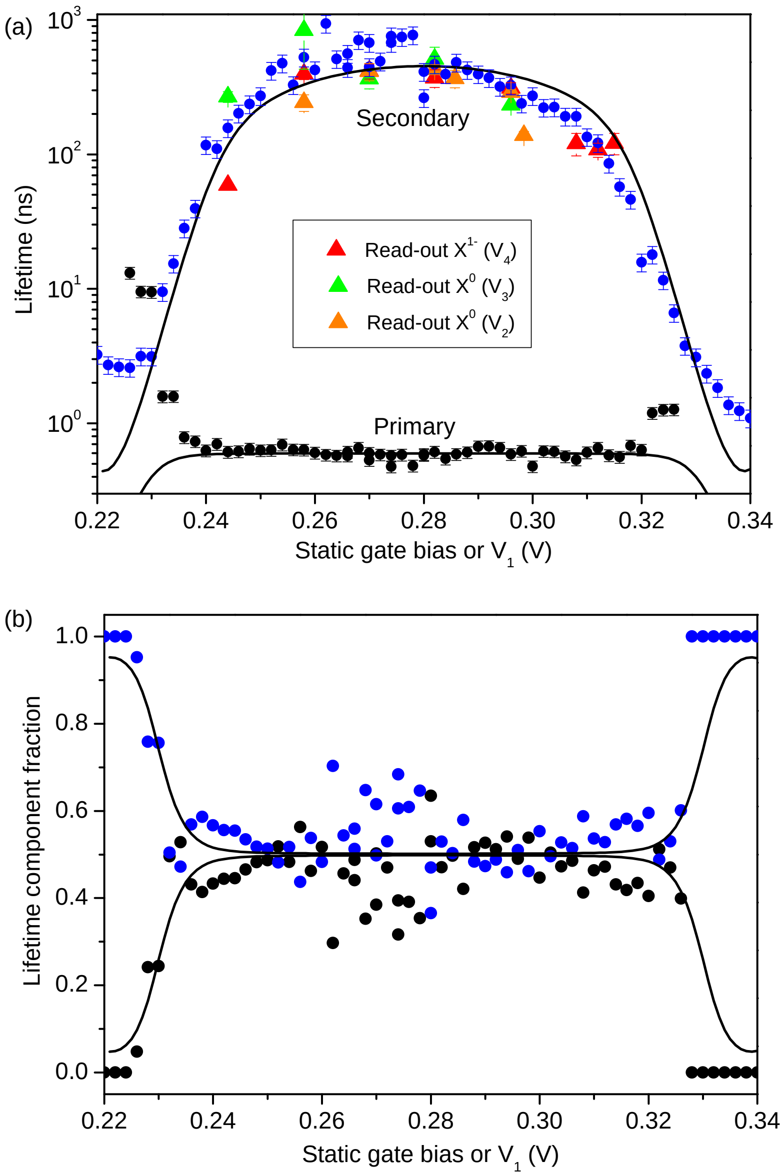

Figure 5.13: (a) Comparison of X^0 lifetimes taken from the same dot as sections 5.5 and 5.6 using the voltage pulsing technique (red, green and orange triangles) with that of standard TCSPC (black and blue circles). The effect of co-tunneling can be seen as a rapid decrease in secondary lifetime towards either edge of the X^0 plateau. (b) shows the fractional contribution of each lifetime component from (a) to the measured TRPL, using the same colour scheme. Included in both graphs is a fit (black line) based on exciton spin flip via co-tunneling [2] using τ_t=26 ps (Δ=40 μeV), δ_{BD}=0.263 meV, T=5 K, γ_r=1.67 ns^{-1} and γ_{nr}=0 ns^{-1}.

$$\gamma_{DB} = \frac{\Delta^2}{h} \int_{\varepsilon} \left(\frac{1}{\varepsilon + e(V_g - V_i)/\lambda} + \frac{1}{e(V_c - V_g)/\lambda - \varepsilon} \right)^2 f(\varepsilon) \left[1 - f(\varepsilon - \delta_{BD})\right] d\varepsilon, \tag{5.1}$$

where γ_{DB} is the dark to bright neutral exciton spin flip rate, and the bright to dark spin flip rate is given by $\gamma_{BD} = e^{\delta_{BD}/k_B T} \gamma_{DB}$. Δ is the tunnel energy, related to the electron tunneling time (τ_t) with $\Delta = \hbar/\tau_t$. τ_t is assumed to stay constant over the X^0 extent. ε is the energy of the Fermi sea continuum state. V_g is the d.c gate voltage bias. V_i is the voltage bias at the hole–X^0 charging point. V_c is the voltage bias at the X^0–X^{1-} charging point. λ is the lever arm ratio. $f(\varepsilon)$ is the Fermi-Dirac function, $f(\varepsilon) = 1/(e^{\varepsilon/k_B T} + 1)$.

The model (Fig. 5.13, black lines) is fitted using the electron tunneling time (τ_t=26 ps), the X^0 energy splitting between dark and bright states (δ_{BD}=0.263 meV), the temperature (T=5 K), and the radiative (γ_r=1.67 ns^{-1}) decay rate. A non-radiative decay rate is not required (γ_{nr}=0ns^{-1}) to fit the model to the data accurately. Fig. 5.13(b) shows the relative intensities of each lifetime component in the TRPL performed at a static voltage bias. There is a 50:50 relative intensity between the primary and secondary decay in the centre of the X^0 extent, both with the model and the TRPL taken with static gate bias. This is because there is a 50% probability of creating either dark or bright X^0 in the dot with each laser pulse, and this confirms that the X^0 secondary lifetime is limited by the electron spin-swap, even at the plateau centre. This is a property of Wafer B (050328B), it does not occur in Wafer A (10311A) due to hole tunneling from the dot to the capping layer [2, 3]. At two static voltage biases, V<0.24 and V>0.32, the primary lifetime of the TRPL taken at static voltage bias in Fig. 5.13(a) increases. This is contrary to the behaviour predicted by the model, because first order tunneling (where X^0 charges (ionises) to become X^{1-} (h)) is prominent at each edge of the X^0 plateau, increasing the lifetime.

The advantage of the GHz pulsed voltage technique over the static voltage TRPL is that all the signal at t> Δt in the static voltage measurement is bundled into one small time window. In this way, a larger signal to noise ratio is achieved at t=Δt, which potentially enhances the accuracy with which τ can be determined. If the tunneling barrier is larger, the electron spin-swap rate can be suppressed by many orders of magnitude [4, 5], and it will be difficult to measure the dark exciton spin relaxation using a TRPL decay curve. Instead, spin read-out using GHz pulsing is much more suitable.

5.8 Resonant pulsed excitation of a single hole and electrical readout

In sections 5.5 and 5.6, the dark X^0 is used as a memory bit with an upper storage time limited by the electron spin swap rate with the back contact, and a choice of readout methods. Section 5.4 shows that the maximum single hole storage times in Wafer B are larger than the storage times possible using dark exciton, and Chapter 3 sections 3.2 and 3.4 show that resonant excitation would be preferable in order to avoid hole storage and at the capping layer–superlattice interface and hole recapture from the dot wetting layer. Resonant excitation would also avoid the spin randomisation that occurs in the wetting layer [6], by directly injecting the hole into the quantum dot. This would open up the possibility of hole spin initialisation, which would give the basis for a qubit (Chapter 1 section 1.1.1). Here, pulsed resonant excitation is employed to "write" a single hole in a dot from Wafer B (050328B) embedded within a device (Device C) designed as in Chapter 4 Fig. 4.9. This is achieved by exciting the $| 0\rangle \rightarrow X^0$ transition at a voltage bias at which the neutral exciton will be immediately ionised, leaving a single hole. The hole is stored for 20 ns, and then GHz bandwidth voltage pulsing causes as many as four electrons to sequentially tunnel into the dot before recombination occurs.

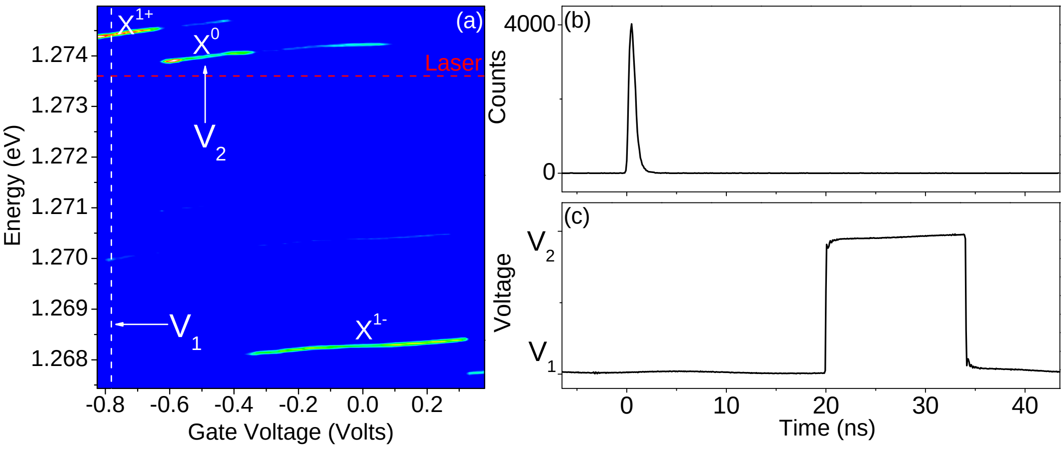

Figure 5.14: (a) Contour plot showing dot PL against static voltage bias for a single dot from Device C (Wafer B) when excited with a CW 830 nm laser at a power of 27.6 nW μm^{-2}. Background counts (<100 counts) are shown as dark blue and increasing counts are shown as light blue (~160 counts), green (~240 counts), yellow (~300 counts), red (330 counts) and white (>350 counts). V_1 is chosen at -180 mV from the h-X^0 charging point. V_2 was varied and forms the x-axis of Fig. 5.15. The laser energy at 1.2736 eV is shown as a dotted red line. (b) A time-resolved measurement of the laser pulse at 1.2736 eV used to excite the dot X^0 transition resonantly at $V=V_1$, with an average power of 46.8 nW μm^{-2}. (c) An oscilloscope measurement of the electronic pulse applied to the sample at a constant delay to (b).

A 90 ps pulse of laser light from a 1.2716 eV-centered broadband Picoquant laser head (controlled electronically by a PDL800-B head unit) and an average power of 46.8 nW μm^{-2} is filtered using the setup detailed in Chapter 2 section 2.3.1. A region at 1.2736 eV with 0.3 meV bandwidth is selected and used to excite the dot (represented in Fig.5.14(a)) with left-hand circularly polarised light at t=0 and V=V$_1$ (=-180 mV) (Fig. 5.14(b) and (c)). The polarisation optics in the microscope head collection arm were cross polarised in order to filter out any laser light that has reflected from the sample surface. After 20 ns, the PPG is used to change the gate bias to V$_2$ (Fig. 5.14(c)) and the PL is recorded with the spectrometer.

Fig. 5.15 shows the PL against V$_2$ value. At t=20 ns a photon is only emitted if V$_2$ is higher than -100 mV. Shown in Fig. 5.15, as V$_2$ is raised beyond -100 mV emission at X^0, X^{1-}, X^{2-} and X^{3-} was observed. The exciton plateau voltage extents are similar as when excited with non-resonant 830 nm laser light, however the absolute voltage biases are 500 mV higher than in Fig. 5.14(a). Reflected laser light at 1.2736 eV is recorded despite polarisation filtering.

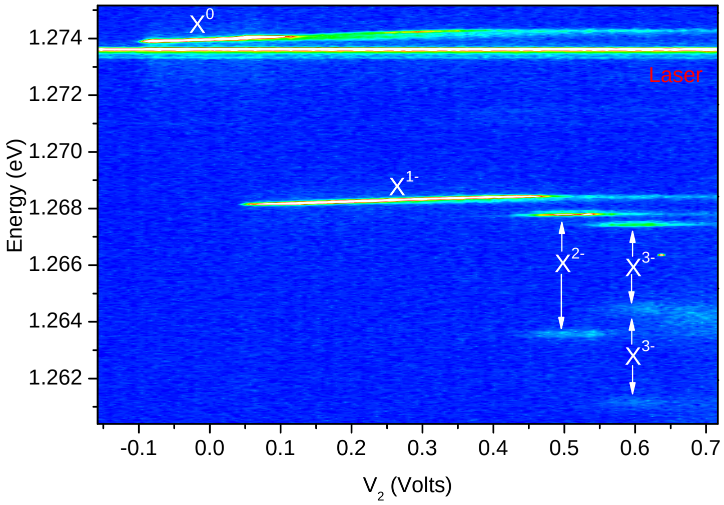

Figure 5.15: PL against V$_2$ value for a dot in Wafer B, Device C (represented by Fig. 5.14(a)), excited with 90 ps pulses of 1.2736 eV laser light with an average power of 46.8 nW μm^{-2} (Fig. 5.14(b)). Background counts (<90 counts) are shown as dark blue and increasing counts are shown as light blue (~100 counts), green (~110 counts), red (120 counts) and white (>140 counts). The dot is excited with a single hole at t=0 and V=V$_1$ (=-180 mV), and at t=20 ns the voltage is changed to V$_2$ (Fig. 5.14(c)).

The energy of the $\mid 0\rangle \rightarrow X^0$ transition at V=V$_1$ is 1.2736 eV (extrapolated from the Stark shift of the X^0 PL). Wafer B exhibits no hole tunneling effects (see Chapter 3 section 3.3.3), therefore only electron tunneling will contribute to the absorption linewidth of the neutral exciton, which is expected to be less than 10 μeV at V=V$_1$ (estimated from the data in Ref. [1]). At t=0 and V=V$_1$ the laser pulse excites the dot with a light at an energy of 1.2736 eV, which populates the dot with a neutral exciton. Due to the gate bias (V=V_1), the electron tunnels out within ~ps [2] and the hole is stored (discussed in section 5.4). At t=20 ns the time-varying voltage pulse from the PPG (Fig. 5.14(c)) changes the bias to V=V_2. If V_2 <-100 mV the hole will remain stored in the dot (and no PL is recorded), otherwise 1, 2, 3 or 4 electrons will tunnel into the dot and allow recombination as X^0, X^{1-}, X^{2-} or X^{3-} to occur. The relative exciton transition voltages in Fig. 5.15 are shifted when compared to Fig. 5.14(a). This is due to hole storage at the capping layer under non-resonant excitation (see Chapter 3 section 3.2). In Fig. 5.14(a) the dot is excited with 27.6 nW μm^{-2} of 830 nm CW laser light, which (when compared to Fig. 5.15 using Eqn. 3.14 from Chapter 3 page 61) suggests that ~3000 holes μm^{-2} are stored at the capping layer interface.

This result combines the knowledge acquired in many of the previous sections in order to demonstrate a highly versatile memory bit. This method has potential applications in quantum computing, since a hole could potentially be written into a dot with known spin, stored indefinitely, and then read out with several determinate wavelengths.

5.9 Resonant CW excitation of X^0 (Adiabatic passage)

In sections 5.5, 5.6 and 5.8, GHz bandwidth voltage pulsing was used to control the "read" step of several defined write–store–read processes. Optical excitation, although electrically triggered, was largely uncontrolled as a "write" step. Here, GHz bandwidth voltage pulsing is used to control the energy levels of the dot through the Stark shift, and hence to control the dot interaction with a narrowband laser which is resonant with the $\mid 0\rangle \rightarrow X^0$ energy transition. In this way, the dot energy levels are moved through the energy of the laser in order to populate the dot. Complete population inversion is possible if the energy levels of the dot are moved through the laser energy at a rate which is slow compared to the Rabi frequency but fast compared to the exciton radiative recombination rate, and this is termed rapid adiabatic passage [7, 8, 9, 10]. Here, the narrowband laser interacts with the dot for a fraction of the ~1 ns voltage response time of the device (~10 ps), which is much smaller than the exciton radiative lifetime (~1 ns). Resonant excitation can also be used to initialise the spin of a hole in the dot.

PL from a single dot (the same dot as in Chapter 3, Fig. 3.19) in Device D (Wafer B) was recorded against voltage bias when excited with 830 nm CW laser light at a power of 200 μW μm^{-2} (Fig. 5.16(a)). The excitons were identified using the same methods as in Chapter 3 section 3.1.2. The Stark shift of X^0 was measured to be 2 μeV mV^{-1}. Two voltage points were defined. V_1 (=0 mV) was placed at the high reverse bias edge of the X^0 plateau. V_2 (=440 mV) was placed in the X^{1-} plateau. The

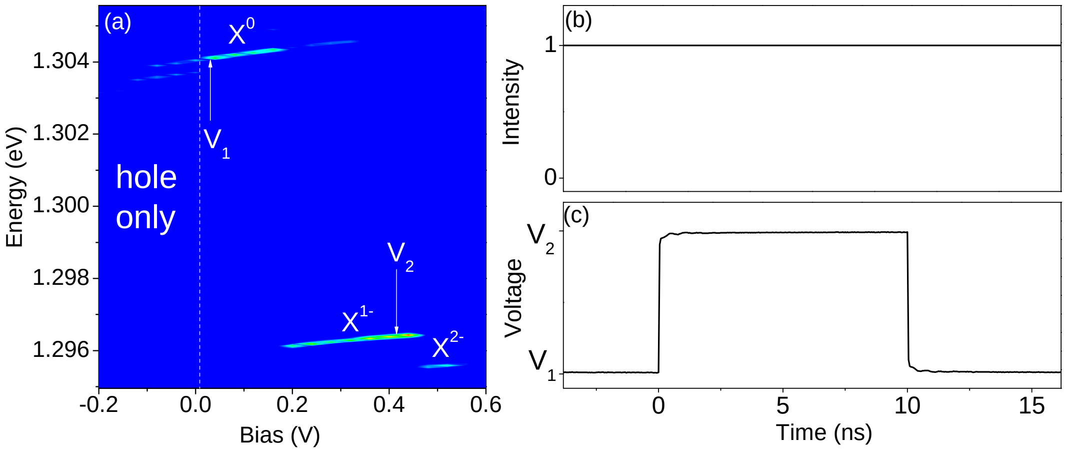

Figure 5.16: (a) Contour plot showing the PL against voltage bias for a single dot in Device D (Wafer B) excited with CW 830 nm non-resonant laser light at a power of 200 μW μm^{-2}. Background counts (<100 counts) are shown as dark blue and increasing counts are shown as green (∼1000 counts), yellow (∼2000 counts) and red (>2300 counts). (b) The narrowband tunable CW laser (a DL-100 grating stabilised diode laser from Toptica Photonics) used to excite the dot at a power of 92 μW μm^{-2}, resonant with the $\mid 0\rangle \rightarrow X^0$ energy transition of the dot. (c) The 50 MHz square wave voltage pulse between V_1 and V_2 applied across the device.

PPG was used to apply a 50 MHz square wave voltage across the device, between V_1 and V_2 (Fig. 5.16(c)). Two TRPL measurements of X^{1-} were recorded as the dot was excited with a CW narrowband tunable laser (a DL-100 grating stabilised diode laser from Toptica Photonics) at a power of 92 μW μm^{-2}. The excitation light from the laser was filtered with an angled bandpass filter (ANDV9415 from Andover Corporation) centered at the laser energy, before reaching the microscope head. The dot PL was filtered by another ANDV9415 bandpass filter, and then using the filter setup described in Chapter 2 section 2.3.1, before reaching the SPAD. This was done in order to prevent any laser light being recorded by the SPAD.

In the first TRPL measurement (Fig. 5.17(a)), the narrowband laser was tuned to 1.30404 eV (resonant with the low voltage edge of the X^0 voltage bias extent). In the second TRPL measurement (Fig. 5.17(b)), the narrowband laser was tuned to 1.30440 eV (resonant with the high voltage edge of the X^0 voltage bias extent). Two clear PL peaks can be seen. The first at t=0 corresponds to the voltage change from V_1 to V_2. The second at t=10 ns corresponds to the voltage change from V_2 to V_1. The peak at t=10 ns is noticeably larger for the higher energy optical excitation. In both Fig.5.17(a) and (b) the exponential decay for the peak at t=0 is ∼0.9 ns. The decay for the peak at t=10 ns in Fig. 5.17(b) is much faster at ∼0.3 ns, with a full width at half maximum of ∼0.35 ns.

In Fig. 5.17, the t=0 peak in (a) and (b) has a decay which is comparable to the radiative lifetime of X^{1-}. This indicates that an X^{1-} is created and allowed to decay radiatively. A reasonable explanation is that the dot is initially empty at

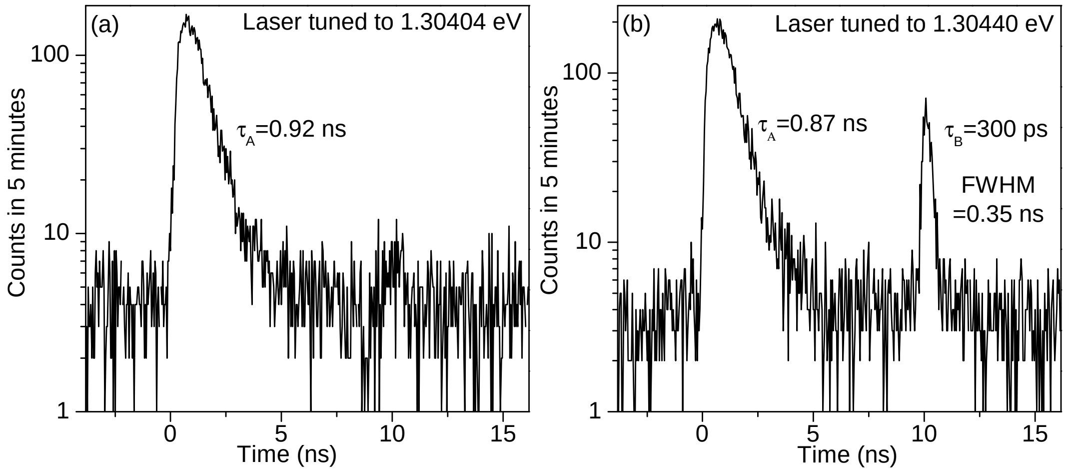

Figure 5.17: TRPL of X^{1-} for a single dot (represented in Fig. 5.16(a)) performed with 92 μW μm^{-2} of narrowband CW resonant illumination of X^0 (Fig. 5.16(b)) and a time-varying gate voltage bias (Fig. 5.16(c)). (a) shows the result when the laser is resonant with the low energy (low voltage bias) side of the X^0 plateau, at 1.30404 eV. (b) shows the result when the laser is resonant with the high energy (high voltage bias) side of the X^0 plateau, at 1.30440 eV.

$V=V_1$. At t=0 the voltage experienced by the dot starts to change from V_1 to V_2. As the $\mid 0\rangle \rightarrow X^0$ energy transition becomes resonant with the energy of the laser, the dot has a probability of being excited with X^0 (rapid adiabatic passage). Then, as the voltage experienced by the dot increases beyond the $X^0 \rightarrow X^{1-}$ charging point, a second electron tunnels from the back contact into the dot to form X^{1-}. Electron-hole recombination releases a photon which can be detected in a TRPL measurement of X^{1-}, leaving a single electron. Lastly, at t=10 ns the voltage experienced by the dot changes from V_2 to V_1, and the electron tunnels from the dot to the back contact, leaving the dot empty. This process would allow the detection of PL from X^{1-} **only** as the voltage changes from V_1 to V_2 at t=0.

The t=10 ns peak in Fig. 5.17(b) has a full width at half maximum and exponential decay which are comparable to the jitter of the SPAD. This suggests a secondary process is also occurring, in which the voltage experienced by the dot is passing through a finite region in which X^{1-} PL is emitted, and is able to pass through this region faster than the radiative recombination of X^{1-}. A reasonable explanation is based on the results from Chapter 3 section 3.5, in which X^0 can be resonantly excited within a small d.c. voltage region which allows electron tunneling to X^{1-}. In the second process, as the voltage experienced by the dot crosses the region in which the lowest one-hole state is X^{1-} and the lowest zero-hole state is $\mid 0\rangle$, resonant excitation of X^0 (within a ~0.14 meV bandwidth absorption region, see Chapter 3 Fig. 3.19) leads to emission of X^{1-} PL. This would allow the detection of PL from X^{1-} **both** as the voltage changes from V_1 to V_2 at t=0, and when the voltage changes

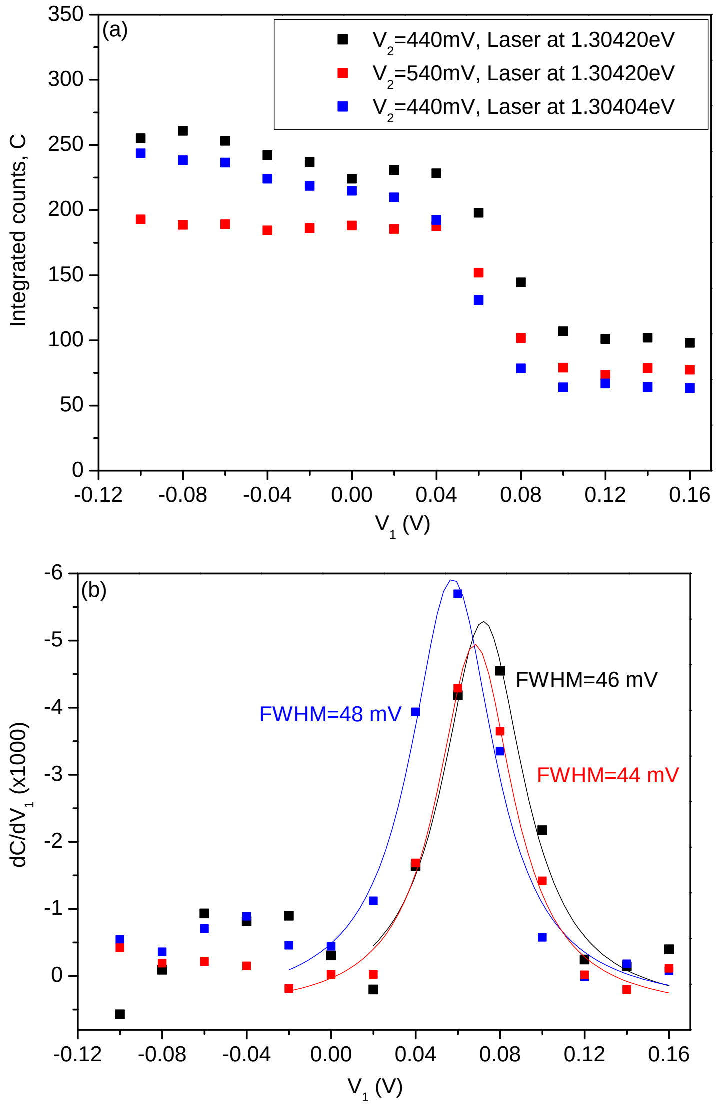

Figure 5.18: (a) Integrated counts for the t=0 peak from X^{1-} TRPL plots for a dot (represented in Fig. 5.16(a)) excited with a 92 μW μm^{-2} narrowband CW laser (Fig. 5.16(b)), and biased with a time varying voltage between V_1 and V_2 (as in Fig. 5.16(c)). V_1 is varied across the X^0 plateau. The black squares represent data taken with V_2=440 mV and a laser energy of 1.30420 eV. The red squares represent data taken with V_2=540 mV and a laser energy of 1.30420 eV. The blue squares represent data taken with V_2=440 mV and a laser energy of 1.30404 eV. (b) shows the the data in (a), differentiated by V_1 ($\frac{dC}{dV_1}$). The colour scheme in (b) is the same as in (a). Each data set in (b) is fitted with a Lorentzian lineshape with a FWHM of 46 mV (black), 44 mV (red), 48 mV(blue).

from V_2 to V_1 at t=10 ns. If this was the **only** active process, the peaks would be equally narrow in the time domain.

Further evidence for the two process explanation is given in Fig. 5.18(a), using the same dot. The narrowband cw laser was tuned to 1.30420 eV, the emission wavelength of X^0 PL at the centre of the X^0 d.c. voltage bias extent (Fig. 5.16), with an average power of 92 μW μm^{-2}. A 50 MHz square wave voltage pulse was applied across the device between V_1 and V_2 in the same manner as before. TRPL of X^{1-} was recorded for several values of V_1, with V_2=440 mV. The integrated PL counts of the t=0 peak are shown in Fig. 5.18(a) (black squares), against the value of V_1. As V_1 becomes larger than ∼60 mV the integrated counts half in value, suggesting that below V_1=40 mV the contribution to the count rate is from both processes, and above V_1=100 mV only the second process is able to contribute. The same measurements were taken at V_2=540 mV (Fig. 5.18(a), red squares) in order that electronic ringing may be discounted as an explanation. The results are differentiated ($\frac{dC}{dV_1}$, Fig. 5.18(b)) and fitted with a Lorentzian lineshape (FWHM=46 mV for V_2=440 mV, FWHM=44 mV for V_2=540 mV), giving a measurement of the voltage range over which the laser interacts with the dot. Since the Stark shift of X^0 is known (2 μeV mV^{-1}), the energy extent over which the laser interacts with the dot is found to be ∼90 μeV. Using the energy time uncertainty principle

$$\Delta E \Delta t \gtrapprox \frac{\hbar}{2} \tag{5.2}$$

where ΔE is energy region over which the laser interacts with the dot (=90 μeV). The time over which the interaction occurs (Δt) is calculated to be ∼4 ps, which is similar to the expected value of ∼10 ps calculated from the voltage response time of the dot.

There is however some data which does not necessarily agree with the identification of rapid adiabatic passage. If the laser energy is lowered the voltage at which the laser is resonant with the dot $\mid 0\rangle \rightarrow X^0$ transition should also become lower. The emission energy of the narrowband cw laser was lowered to 1.30404 eV, with an average power of 92 μW μm^{-2}. A 50 MHz square wave voltage pulse was applied across the device between V_1 and V_2 as before. TRPL of X^{1-} was recorded for several values of V_1, with V_2=440 mV. The integrated PL counts of the t=0 peak are shown in Fig. 5.18(a) (blue squares), against the value of V_1. The differentiated data ($\frac{dC}{dV_1}$) are presented in Fig. 5.18(b) (blue squares), fitted with a Lorentzian lineshape with a FWHM of 48 mV, centred at V_1=58 mV. This is ∼12 mV lower than the Lorentzian lineshapes from the data using a laser energy of 1.30420 eV. From the Stark shift, tuning the laser to 1.30404 eV is expected to lower the voltage at which the laser interacts with the dot $\mid 0\rangle \rightarrow X^0$ transition by ∼80meV. This difference between the expected and measured values casts doubt on the interpretation of rapid adiabatic passage.

Is this adiabatic passage?

In conclusion to the investigation of adiabatic passage in this experiment, the main points are reviewed. First, resonant excitation of X^0 occurs when the $\mid 0\rangle \rightarrow X^0$ transition in the dot is electronically altered (using the Stark shift) in order to cross through the laser energy. Second, from the measurements in this section and in Chapter 4, it is expected that the energies cross smoothly and at a rate which is far faster than the radiative lifetime of X^0. Third, electronic ringing and other optical processes have been disqualified as potential explanations for the results. Lastly however, when the laser energy is altered, the system did not respond to the magnitude that was expected, calculated from the Stark shift measured with non-resonant optical excitation. More experiments are required to resolve this issue.

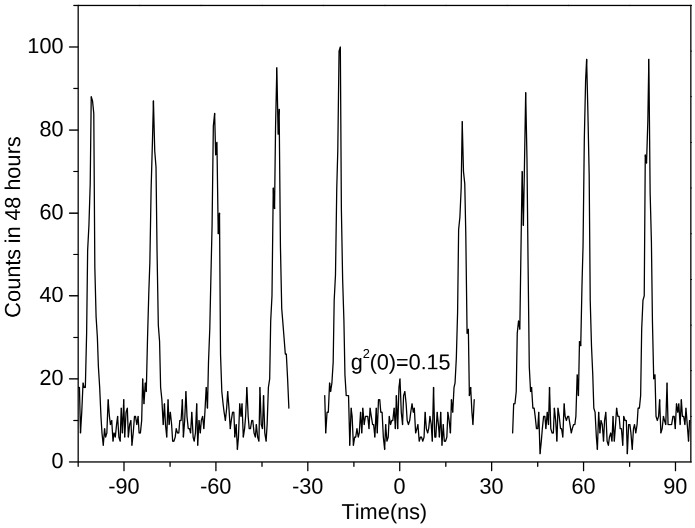

Figure 5.19: Autocorrelation of X^{1-} PL for a dot (represented by Fig. 5.16(a)) excited by a 92 μW μm^{-2} narrowband CW laser (Fig. 5.16(b)) which emits at 1.3042 eV, and biased with a time varying voltage between V_1 and V_2 (as in Fig. 5.16(c)). $g^{(2)}(0)=0.15$. The base level is raised due to the dark counts of the SPADs. The omitted data at t=±27 ns is due to broadband light emission from the SPADs (see Chapter 2 section 2.3 and Fig. 2.8).

Does this technique produce single photons?

Independent of the underlying mechanism for photon emission, it is still important to determine if the method yields electronically triggered single photons. An autocorrelation measurement was performed. The same dot was excited with 1.30420 eV of CW laser light at a power of 92 μW μm^{-2}, as before (Fig. 5.16(b)). V_1 and V_2 were chosen to be 0 mV and 440 mV, respectively. A 50 MHz square wave voltage pulse was applied across the device between V_1 and V_2 as in Fig. 5.16(c). Recorded in Fig. 5.19 is an autocorrelation of X^{1-} performed using the HBT interferometer (as described in Chapter 2). The $g^{(2)}(0)$ value (as defined in Chapter 1 section 1.4.4) is measured at 0.15 (the contribution due to the dark counts of the SPADs have been subtracted).

The auto-correlation shows that this is an effective method of creating single photons. The $g^{(2)}(0)$ value is not zero, possibly due the interaction of the laser with the region described in Chapter 3 section 3.5.

5.10 Conclusion

GHz bandwidth voltage pulses have been successfully applied to a charge-tunable quantum dot heterostructure. Both electron tunneling and optical excitation are fully controllable within the timescale of exciton recombination. Several write-store-read processes have been created, using either a single hole or a dark exciton as a memory bit. Also, two methods of creating electrically triggered deterministic single photons have been shown, using both pulsed resonant optical excitation and CW non-resonant optical excitation. Lastly, adiabatic passage was attempted, but not confirmed.

References

[1] S. Seidl, M. Kroner, P. A. Dalgarno, A. Hogele, J. M. Smith, M. Ediger, B. D. Gerardot, J. M. Garcia, P. M. Petroff, K. Karrai and R. J. Warburton, *Absorption and photoluminescence spectroscopy on a single self-assembled charge-tunable dot.* Physical Review B, **72**, 195339 (2005).

[2] J. M. Smith, P. A. Dalgarno, R. J. Warburton, A. O. Govorov, K. Karrai, B. D. Gerardot and P. M. Petroff, *Voltage control of the spin dynamics of an exciton in a semiconductor quantum dot.* Physical Review Letters, **94**, 197402 (2005).

[3] P. A. Dalgarno, Thesis title: *Time correlated single photon counting on charge tunable quantum dots.* (2005).

[4] M. Kroner, K. M. Weiss, B. Biedermann, S. Seidl, A. W. Holleitner, A. Badolato, P. Petroff, P. Öhberg, R. J. Warburton and K. Karrai, *Resonant two-color high-resolution spectroscopy of a negatively charged exciton in a self-assembled quantum dot.* Physical Review B, **78**, 075429 (2008).

[5] J. Dreiser, M. Atatüre, C. Galland, T. Müller, A. Badolato and A. Imamoglu, *Optical investigations of quantum dot spin dynamics as a function of external electric and magnetic fields.* Physical Review B, **77**, 075317 (2008).

[6] S. Trumm, M. Wesseli, H. J. Krenner, D. Schuh, M. Bichler, J. J. Finley and M. Betz, *Spin-preserving ultrafast carrier capture and relaxation in InGaAs quantum dots.* Applied Physics Letters, **87**, 153113 (2005).

[7] N. V. Vitanov, T. Halfmann, B. W. Shore and K. Bergmann, *Laser-induced population transfer by adiabatic passage.* Annual Review of Physical Chemistry, **52**, 763 (2001).

[8] S. Avrillier, J. M. Raimond, Ch. J. Bordé, D. Bassi and G. Scoles, *Supersonic beam spectroscopy of low J transitions of the* υ_3 *band of* SF_6*: rabi oscillations and adiabatic rapid passage with a cw laser.* Optics Communications, **39**, 311 (1981).

[9] V. Lorent, W. Claeys, A. Cornet and X. Urbain, *Rabi oscillations and adiabatic rapid passage measured in the 2s–3p transition of atomic hydrogen.* Optics Communications, **64**, 41 (1987).

[10] A. G. Adam, T. E. Gough, N. R. Isenor and G. Scoles, *Rabi oscillations and rapid-passage effects in the molecular beam* CO_2*–laser Stark spectroscopy of* CH_3F. Physical Review A, **32**, 1451 (1985).

Chapter 6

Potential improvements and further work

6.1 Improvements to the experimental setup

The confocal setup (see Chapter 2 section 2.1) was, on the whole, very successful at selecting and isolating single quantum dots. The microscope head was fully adjustable, allowing the maximum of the available PL to be collected for analysis. Also, the polarisation optics were extremely useful in filtering out the reflected laser light when appropriate (see Chapter 5 section 5.8), and will be useful for initialising the spin of the hole in future experiments. However, there are two main improvements that can be made to the design:

Adaptation of the experimental setup for laser spectroscopy

Adaptations to the experimental setup would allow for resonant absorption experiments to be performed on a single dot [1]. In this way, an accurate measurement of the exciton linewidths could be made, as well as the effect of power broadening on the exciton linewidth, and the fine structure splitting of the neutral exciton. These measurements would benefit those of Chapter 3 section 3.3.

Use of a GaAs S-SIL

The use of a glass (n=2.15) S-SIL was a huge improvement in the PL collection efficiency, compared to the glass hemispherical SIL (see Chapter 2 section 2.8). A further improvement could be made by using a GaAs (n=3.5) S-SIL, in order to eliminate any refraction effects as the dot PL crosses between the sample and the S-SIL. Using a GaAs S-SIL the collection efficiency should in theory approach 50% [2], although manufacturing tolerances are much smaller due to the high refractive index.

6.2 Improvements to the microscopic device

In Chapter 4 a microscopic device was successfully created which could respond to GHz bandwidth voltage pulsing. However, as shown in Chapter 4 Fig. 4.20, the 360 nm thick NiCr contact strip suffered from rippling and lift-off problems, which caused the deposited metal to flake away from the semiconductor material with repeated thermal cycling. Project student Jonathan Prechtel has recently solved this problem by using a contact strip consisting of NiCr, then Ti, then Au, deposited onto the device using e-beam evaporation with thicknesses of 5 nm, 3 nm, and 50 nm, respectively. The thick gold layer at the top of the contact strip has a much smaller resistivity than NiCr. The gold layer also allows gold wires to be bonded to the device using a K & S model 4123 wedge bonder, instead of using silver conductive paint as in this work (see Chapter 4 section 4.4).

In addition, by re-designing the device it should be feasible to etch a larger area around the Schottky gate, which would destroy the back contact in those regions. This would help to reduce stray capacitances in the system, and hopefully lead to a faster device.

6.3 Further GHz bandwidth voltage experiments

The experiments performed in Chapter 5 were very successful. The main goal of this project was to manipulate the charge held in a quantum dot, on the timescale of exciton recombination. Much more than this was achieved. There are several possible advances on this work.

Measuring the voltage pulse shape

An interesting new method of recording the voltage pulse shape experienced by the dot was recently developed by Jonathan Prechtel and Paul Dalgarno using a device designed and constructed by the author. This method makes use of the voltage region probed in Chapter 3 section 3.5, in which resonant excitation of X^0 results in PL detection at X^{1-}. The region is used as a small probe region to a large amplitude GHz voltage pulse. Shown in Fig. 6.1(a) is the PL recorded for a dot from Wafer B against d.c. voltage bias, as X^0 is excited by a CW laser emitting at 952.105 nm with power of 73.4 μW μm^{-2}. X^{1-} PL is clearly seen emitting over a small bias region. If a 10 MHz square wave time-varying voltage is applied over the sample with a fixed amplitude of 200 mV and an offset (defined as the mean value of the square wave) of 175 mV, TRPL of X^{1-} (presented in Fig. 6.1(b)) shows the interaction of the dot with the laser as the voltage changes at 30 ns (from 275 mV to 75 mV) and 80 ns (from 75 mV to 275 mV).

Several points on each PL peak are defined: **A** is at the maximum of each peak, **B** is at half of maximum on the rising edge of each peak, **C** is at the beginning of each peak, and **D** is at the end of each peak. The time of each point was recorded as the offset of the square wave was varied in Fig. 6.2.

PL is only recorded from X^{1-} at the point at which the $\mid 0\rangle \rightarrow X^0$ transition of the dot is resonant with the laser, therefore the position in time of the X^{1-} PL gives an indication of when the resonance occurs for a given offset of the square wave time varying voltage. In this way, it is possible to map the changing voltage as experienced by the dot, as shown in Fig. 6.2. Exponential fits give an indication of the $\frac{1}{e}$ response time for this device Fig. 6.2 (red lines) at ∼2–3 ns, which is similar to the values obtained for the devices in this work. This method should be included in future attempts to measure the voltage response time of a single dot.

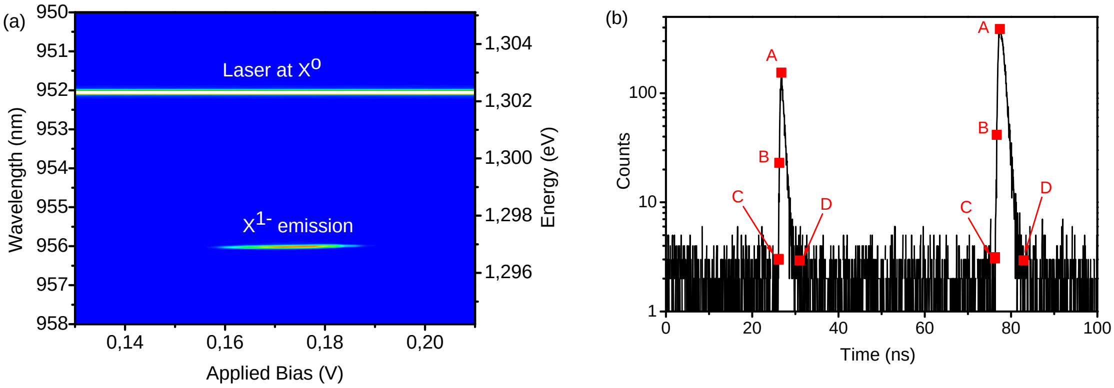

Figure 6.1: (a) The PL against d.c. voltage bias recorded as CW excitation laser at 952.105 nm excites the $|\,0\rangle \rightarrow X^0$ transition of a single dot in Wafer B with a power of 73.4 μW μm^{-2}. (b) TRPL of X^{1-} recorded for 10 minutes, as a 10 MHz repetition rate square wave time-varying voltage with an amplitude of 200 mV and an offset of 175 mV is applied across the dot in (a), with optical excitation also as in (a). Images by Jonathan Prechtel.

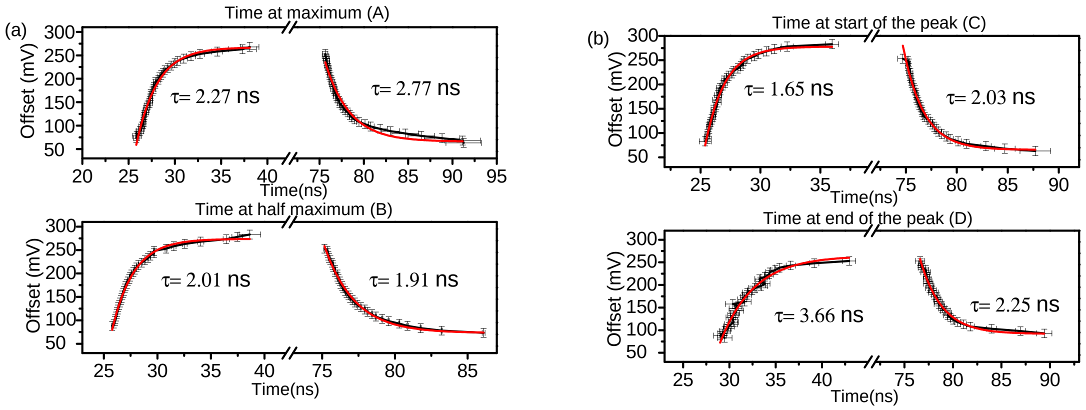

Figure 6.2: The offset of the square wave voltage pulse applied across the device, against the occurance time recorded for (a) the maximum peak height (**A**) and the half-maximum height (**B**), and (b) the start (**C**) and end (**D**) of the two peaks recorded in TRPL of X^{1-} as shown in Fig. 6.1(b). Images by Jonathan Prechtel.

Initialising the spin of a hole in dot

Read out of the hole spin was not achieved in this work, and as such it was not possible to prove that the hole was successfully initialised. It is thought that an interaction with the neutral exciton (due to the fine structure and/or the co-tunnelling regions) caused randomisation of the hole. The solution may be to use a faster device, so that the interaction time with the neutral exciton extent is minimised.

Measuring the T_2 time of the electron spin

GHz bandwidth voltage pulsing could also potentially be used to investigate the spin dephasing (T_2) time of the electron using vertically coupled quantum dots in a charge-tunable structure, using a method similar to that in Ref. [3]. In a similar structure to that of Wafer B (050328B), two vertically coupled quantum dots could be separated from a n-doped back contact by ∼25 nm of GaAs, acting as a tunneling barrier. At the first voltage (V_1), two electrons would be held within the dot closest to the back contact (Dot 1). Then at time t_1, the voltage would be altered so that one of the two electrons in Dot 1 would tunnel into the second dot (Dot 2). At time τ, the voltage would be changed back to V_1. Recreation of a two-electron state in Dot 1 would depend on the electrons maintaining their phase. Resonant absorption of the $| 0\rangle \rightarrow X^0$ transition in Dot 2 would allow a measurement of the number of electrons in Dot 2 at time τ. The hyperfine interaction from the surrounding nuclei would cause independent slowly evolving (>10 μs [3]) fields on each electron at time $t_1 < t < \tau$, causing a coherent population transfer (Rabi oscillations) between spin-up and spin-down electrons. This coherent spin manipulation would then be destroyed by the spin dephasing (T_2), and could be measured by adjusting τ and measuring the absorption. This method would be successful for T_2 times much smaller than the evolution of the hyperfine interaction.

Adiabatic passage

Further investigation into the experiment performed in Chapter 5 section 5.9 could reveal whether or not adiabatic passage was achieved in this work. With better optical filtering a much more strict set of experiements could be performed. For instance, the read-out step could potentially be performed using optical read-out of X^0, instead of using X^{1-} as in this work.

References

[1] A. Högele, S. Seidl, M. Kroner, K. Karrai, R. J. Warburton, B. D. Gerardot and P. Petroff, *Voltage-controlled optics of a quantum dot.* Physical Review Letters, **93**, 217401 (2004).

[2] K. A. Serrels, E. Ramsey, P. A. Dalgarno, B. D. Gerardot, J. A. O'Connor, R. H. Hadfield, R. J. Warburton and D. T. Reid, *Solid immersion lens applications for nanophotonic devices.* Journal of Nanophotonics, **2**, 021854 (2008).

[3] J. R. Petta, A. C. Johnson, J. M. Taylor, E. A. Laird, A. Yacoby, M. D. Lukin, C. M. Marcus, M. P. Hanson and A. C. Gossard, *Coherent manipulation of coupled electron spins in semiconductor quantum dots.* Science, **309**, 2180 (2005).